Efficient Superconducting-Nanowire Single-Photon Detectors and Their Applications in Quantum Optics

by

Xiaolong Hu

Submitted to the
Department of Electrical Engineering and Computer Science
in partial fulfillment of the requirements for the degree of

Doctor of Philosophy in Electrical Engineering and Computer Science

at the

MASSACHUSETTS INSTITUTE OF TECHNOLOGY

February 2011

Author .....
Department of Electrical Engineering and Computer Science
November 04, 2010

Certified by .....
Karl K. Berggren
Associate Professor of Electrical Engineering
Thesis Supervisor

Accepted by .....
Terry P. Orlando
Chairman, Department Committee on Graduate Students

Efficient Superconducting-Nanowire Single-Photon Detectors and Their Applications in Quantum Optics

by

Xiaolong Hu

Submitted to the Department of Electrical Engineering and Computer Science on November 04, 2010, in partial fulfillment of the requirements for the degree of Doctor of Philosophy in Electrical Engineering and Computer Science

Abstract

Superconducting-nanowire single-photon detectors (SNSPDs) are an emerging technology for infrared photon counting and detection. Their advantages include good device efficiency, fast operating speed, low dark-count rate, low timing jitter, free running mode, and no afterpulsing. The challenges to be addressed prior to real applications are cryogenic operations, small active areas, and efficiency-speed tradeoffs. This thesis presents the effort to address these challenges.

A fiber-coupled SNSPD system with a large-area detector in a closed-cycle cryocooler has been built, demonstrating 24% system detection efficiency with a dark-count rate of ~1000 counts/sec. As a result, the SNSPD system becomes a convenient tool with a single-mode fiber as the input channel and an SMA cable as the output channel. This system has enabled high-quality polarization-entanglement distribution at the wavelength of 1.3 μm. The 99.2% visibility in Hong-Ou-Mandel (HOM) interference measured in this experiment is the highest HOM visibility that has ever been reported for waveguide-based photon-pair sources. After entanglement is distributed, a pair rate of 5.8 pairs/sec at a pump power of 25 μW and two-photon quantum interference visibility of 97.7% have been measured.

On the other hand, increasing the active area of the detector does decrease its speed. To address the issue of efficiency-speed tradeoff, SNSPDs have been integrated with optical nano-antennae. A 9-μm-by-9-μm detector with 47% device efficiency and 5-ns reset time has been demonstrated. In terms of active area, device efficiency and speed, this SNSPD has the record performance among single-element SNSPDs. Finally, waveguide-integrated SNSPDs have been proposed and designed. The device structure permits efficient coupling of photons into a short nanowire, and thus, efficient and fast SNSPDs. This structure is compatible with on-chip photonic technologies, including inverse-taper couplers and ring resonators, that have been developed in recent years.

Thesis Supervisor: Karl K. Berggren
Title: Associate Professor of Electrical Engineering

Acknowledgments

I am greatly thankful to my advisor, Professor Karl Berggren, for his constant guidance, advice, and encouragement. He helped me choose the topic, taught me many experimental skills, and more importantly, created a nurturing environment in which I could continuously extend my ability to do scientific research.

I would also like to express my sincere acknowledgement to a multitude of people who have contributed to this project in different ways.

To Prof. Terry Orlando and Prof. Jeffery Shapiro for being on my thesis committee board and giving me advice on my thesis work;

To Prof. Cardinal Warde and Prof. Qing Hu for being on the committee board of my research qualification exam and giving me advice on my research;

To Dr. Franco Wong and Tian Zhong for fruitful collaboration;

To Dr. Charles Holzwarth and Jie Sun for fruitful collaboration;

To Dr. Eric Dauler and Dr. Richard Molnar at the MIT Lincoln Laboratory for fruitful collaboration;

To Dr. Francesco Marsili and Faraz Najafi for fruitful collaboration;

To Donald Winston for helping me with the Monte Carlo simulation;

To Prof. Rajeev Ram for his generosity in allowing me to use the probe station in his laboratory;

To Prof. Henry Smith for his expertise in nanofabrication;

To Prof. Mark Brongersma at Stanford Univerity, Prof. David Staelin at MIT, Dr. Bae-Ian Wu at MIT, and Prof. Eli Yablonovitch at the University of California, Berkeley for helpful discussions;

To Dr. Euclid Moon and John Lesieutre for proofreading my thesis;

To Mark Mondol and James Daley for their technical assistance;

To Nicolas Antoniou at Harvard University for his technical assistance;

To Tiffany Kuhn, Alicia Akins, and Sarah Gleason for their administrative assistance;

To my group mates, past and present, for their friendship and sharing knowledge;

To all the members of the Nanostructure Laboratory, past and present, for sharing lab skills and experiences;

To the Intelligence Advanced Research Projects Activity (IARPA), National Science Foundation, and the U.S. Department of Energy, Office of Science, Office of Basic Energy Sciences for the financial support;

Last, but not least, I would like to express my gratitude to my father, my mother, and all my family members in China for their continuous encouragement and support.

Contents

1 Introduction **17**

1.1 Applications of infrared single-photon detectors 19

1.2 Terminology for describing the performance of an SNSPD 20

1.3 Materials, existing device structures, and detection mechanism 24

1.4 Performance of state-of-the-art SNSPDs and comparison with other technologies 28

1.5 Outline of this thesis 29

2 Superconducting-nanowire single-photon detector system **31**

2.1 Device design and fabrication 32

2.2 Chip package 35

2.3 Circuit and optical illumination 38

2.4 Output pulse and reset time 38

2.5 Dark-count rate 39

2.6 Optical alignment 40

2.7 System detection efficiency 41

2.8 Discussion 42

3 Polarization-entanglement distribution using the superconducting-nanowire single-photon detector system **45**

3.1 Experimental setup 46

3.2 Hong-Ou-Mandel interference 51

3.3 Characterization of entanglement distribution 54

3.4 Summary 57

4 Superconducting-nanowire single-photon detector integrated with optical nano-antennae 59

4.1 Concept and device design 60

4.2 Device fabrication and imaging 66

4.3 Device characterization 69

4.3.1 Device efficiency 69

4.3.2 Kinetic inductance 72

4.3.3 Timing jitter 72

4.4 Comparison with previously reported devices 74

4.5 Integration of 30-nm wide nanowires with antennae 74

4.6 Summary 79

5 Waveguide-integrated superconducting-nanowire single-photon detector 81

5.1 Introduction 81

5.2 Design 82

5.3 Comparison with cavity-integrated SNSPDs 89

5.4 Development of fabrication process 91

5.5 Summary 95

6 Summary and future directions 97

6.1 Summary 97

6.2 Future directions 98

A Standard operation procedure and maintenance of the SNSPD system 103

A.1 Standard operation procedure 103

A.1.1 Before using the system 103

A.1.2 After using the system 104

A.2 Maintenance 105
A.2.1 Optical alignment 105
A.2.2 Procedure to measure dark count rate and system detection efficiency 106
A.2.3 Procedure to shut down the system 106
A.2.4 Procedure to start the system 107
A.2.5 Procedure to refill the compressor unit with ultra-pure helium gas 107

B Calculation of reset time **109**

C Fit of the optical constants of NbN using the Drude model **111**

D Linearly polarized mode with a Gaussian profile to approximate the mode in a single-mode optical fiber **119**

List of Figures

1-1 Schematic of a single-photon detector 20

1-2 Schematic presentation of dark counts 21

1-3 Schematic presentation of system detection efficiency 22

1-4 Schematic presentation of reset time 23

1-5 Schematic presentation of timing jitter 23

1-6 Detection mechanism and the circuit model of a superconducting-nanowire single-photon detector 27

1-7 Schematic of a SNSPD in a meander structure 28

1-8 Cross-section schematic of a NbN nanowire meander without (a) and with (b) integration of a quarter-wavelength cavity. 28

2-1 Micrograph of the fabricated superconducting-nanowire single-photon detector 33

2-2 Photograph of the chip of superconducting-nanowire single-photon detectors 34

2-3 Schematic of the chip package 36

2-4 Photograph of the chip of the chip package mounted on the cold head of the cryocooler. 36

2-5 Photographs of the chip plate. 37

2-6 Photograph of the SNSPD system after all parts were installed. . . . 37

2-7 Schematic of the circuit and the illumination. 38

2-8 Output voltage pulse of the system 39

2-9 Measured system detection efficiencies and dark-count rate as a function of bias current 40
2-10 Calculated noise-equivalent power 43

3-1 Schematic of the experimental setup for polarization-entanglement distribution. 47
3-2 Example output of the time-amplitude converter. 49
3-3 Zoom-in presentation of the peak in Figure 3-2. 49
3-4 Schematic of the usual way to measure coincidences by using two single-photon detectors. 50
3-5 Time-multiplexing scheme to measure coincidences. 50
3-6 Schematic of Hong-Ou-Mandel interference without distinguishability. 52
3-7 Schematic of Hong-Ou-Mandel interference with distinguishability. . . 52
3-8 Experimental setup of Hong-Ou-Mandel interference. 53
3-9 Measured Hong-Ou-Mandel interference. 54
3-10 Measured two-photon quantum-interference after entanglement distribution. 55
3-11 Measured visibilities as the function of the mean pair number. 56
3-12 Repeated measurement of two-photon interference visibility. 57

4-1 Explanation of the concept development of the superconducting-nanowire single-photon detector integrated with optical nano-antennae 61
4-2 Study of non-resonant nano-optical collection effect. 63
4-3 Simulated absorption enhancement as a function of cavity length. . . 64
4-4 Study of the frequency-selective-surface effect 65
4-5 Simulated intensity distribution and time-averaged Poynting vectors . 66
4-6 Scanning-electron micrograph of the fabricated superconducting-nanowire single-photon detector integrated with optical nano-antennae. 68
4-7 Cross-section schematic illustrating the appearance of voids and their effect on the absorption of the NbN nanowire. 69

4-8 Measured device efficiency as a function of bias current normalized to the critical current 70
4-9 Histogram of device efficiency of the detectors with maximum device effiecny larger than 10% on the chip. 71
4-10 Histogram of timing jitter of the superconducting nanowire single-photon detector integrated optical nano-antennae 73
4-11 Simulation of the cavity effect for a 30-nm wide nanowire integrated with nano-antennae for detecting single photons at the wavelength of 4 μm 76
4-12 Simulated peak absorption and optimum cavity length as a function of wavelength. 76
4-13 Monte Carlo simulation of electron forward scattering and secondary electron scattering at an acceleration voltage of 30 kV inside 500-nm thick HSQ. 78
4-14 Monte Carlo simulation of electron forward scattering and secondary electron scattering at an acceleration voltage of 100 kV inside 500-nm thick HSQ. 78
4-15 Experimentally realized 30-nm wide HSQ structure using thick HSQ. 79
4-16 Scanning-electron micrograph of a fallen-down HSQ structure. 79

5-1 Schematics of waveguide-integrated superconducting-nanowire single-photon detector 83
5-2 Simulated coupling loss between a single-mode fiber and the inverse-taper coupler 86
5-3 Evolution of the TE-like mode inside the inverse-taper coupler 88
5-4 Distribution of the x-component of the electric field in TE-like mode inside the inverse-taper coupler 89
5-5 Simulated imaginary part of the complex effective index as a function of the width of the waveguide 90
5-6 Simulated $A \times \eta_c$ efficiency as a function of the length of the nanowire. 90

5-7 Scanning-electron micrograph of the nanowire for waveguide integration 92
5-8 Optical micrograph of the waveguides aligned with the nanowires. . . 93
5-9 Top-view optical micrograph of the waveguides after being cleaved at the facet 94
5-10 Cross-section scanning-electron micrograph of the waveguide after being cleaved at the facet 94

C-1 Fit of the measured optical constants of NbN using the Drude model 112

D-1 Comparison between the simulated field distribution and the approximated distribution of E_x in a single-mode optical fiber 121

List of Tables

1.1 Performance of state-of-the-art SNSPDs and comparison with other technologies at the wavelength of 1550 nm. 29

5.1 Optical constants 86

C.1 Refractive indices of NbN thin film measured by elliposmetry. 113

Chapter 1

Introduction

Superconducting-nanowire single-photon detectors (SNSPDs), also referred to as superconducting single-photon detectors [1], are an emerging technology for infrared photon counting and detection. The advantages of this technology include good device efficiency at telecom wavelengths [2], broadband response [3, 4], fast operating speed [5], low timing jitter [6], low dark-count rate [7, 8], and negligibly low afterpulsing. The major disadvantages, or challenges, of this technology include cryogenic operation at an operating temperature of 4 K or below and small active area. The cryogenic operation is determined by the nature of the material used for the detectors. Because of this cryogenic operation, engineering work is required to package the detector in a cryogenic system in order to fully demonstrate the potential in efficiency for real applications. The small active area is determined by the nature of the structure used for the detectors, which is, of course, related to the working principle of the detector. The device has to be fabricated into a thin and narrow nanowire meander structure in order to detect single photons efficiently: the thickness is between 4 nm and 6 nm, and the width of the nanowire is below 100 nm. Current technology cannot fabricate long nanowires with such thickness and width without adding additional defects, generally called constrictions [9], onto the nanowires. In addition to these two challenges, there is an intrinsic tradeoff between the efficiency and the upper limit of the operating speed of the detector [5, 10]. The operating speed of the detector is limited by the kinetic inductance of the nanowire [5], which is proportional to the

length of the nanowire. Thus, as far as the operating speed is concerned, a shorter nanowire is preferable. On the other hand, in order to couple light efficiently into the nanowire, a longer nanowire is needed to cover a large enough active area. It is desirable to overcome, or at least to improve, this tradeoff to make the detector work efficiently and fast at the same time.

This thesis presents the work to address these challenges in the field of SNSPDs. The work includes (1) a fiber-coupled SNSPD system with a large active area in a closed-cycle cryocooler [7]; (2) application of this system in a quantum optics experiment - photonic polarization-entanglement distribution at the wavelength of 1.3 μm [11]; (3) antenna-integrated SNSPDs with a 9-μm-by-9-μm practical active area, 5-ns reset time, and 47% device efficiency [10]; and (4) design of a waveguide-integrated SNSPD for on-chip quantum information processing and fiber-coupled systems [10]. The motivation of part (1) is to address the challenge of its cryogenic operation and build a real detector system to demonstrate the potential of SNSPD technology. Part (2) is a demonstration of the impact of SNSPDs in the field of quantum optics. The motivation of parts (3) and (4) is to make SNSPDs work simultaneously fast and efficiently.

Before going into these topics, this chapter introduces the background, putting the research into context. Section 1.1 presents the applications that require fast and efficient infrared single-photon detectors, Section 1.2 defines terminology used throughout the thesis, Section 1.3 explains the operating principle of SNSPDs, Section 1.4 summarizes the performance of state-of-the-art SNSPDs and compares that with the performance of other infrared photon-counting technologies. Section 1.5 outlines the following chapters.

1.1 Applications of infrared single-photon detectors

Human eyes *cannot see* a single photon, whether visible or infrared, although the sensors in the retina *can respond* to a single photon [12]. Neural filters only allow an optical signal with at least a few photons arriving within less than 100 ms to trigger a conscious response. A single-photon detector (or a photon counter) is a device that can change optical signals to observable signals with single-photon sensitivity. A single-photon input is energetic enough to fire the detector to give a readable output. Single-photon counting is generally useful for all spectral ranges, and infrared photon counting ($\lambda > 800$ nm) is particularly interesting because of several important applications.

The first application is fiber-based quantum key distribution (QKD) [13, 14, 15]. The lowest loss window of optical fiber is at the wavelength of 1.55 μm, and the second lowest loss window is at the wavelength of 1.3 μm. To employ either of these windows to avoid large transmission loss, both the source and the detector need to work at these infrared wavelengths. In a QKD system, all the components other than detectors can be the same as the components used in a classical optical communication system; however, the detectors must have single-photon sensitivity. The efficiency and the speed of the single-photon detectors are among the determining factors for the capacity of the QKD system. Thus, efficient and fast single-photon detectors at near-infrared wavelengths are desirable.

The second application of SNSPDs is deep-space optical communications, for example, between the Earth and the moon. The wavelength for deep free-space optical communications is also chosen to be infrared [16]. Because of the long distance and the resulting large attenuation, sensitive, efficient, and fast photodetectors are needed. SNSPDs are good candidates.

The third application of SNSPDs is non-invasive diagnosis of the problems in very-large-scale-integration (VLSI) circuits [17]. Because of the high density of the components, it is difficult to diagnose the problems and identify the defects of modern

VLSI circuits. One way to perform the diagnosis without affecting the circuits is to test the circuits optically while the circuits are operating. The principle of this test is based on the fact that when a complementary-metal-oxide-semiconductor (CMOS) transistor switches, the transistor will emit weak light signals at infrared. This luminescence is time-correlated with the switching of the CMOS, and the strength of the luminescence is related to the quality of the transistor. For example, if there is a current leak in the oxide layer, there will be stronger luminescence than a normal transistor can emit. So, detecting the luminescence can help obtain the information about the quality of the transistors. SNSPDs are good detectors for detecting this weak luminescence.

In addition to the applications mentioned above, SNSPDs are generally useful for any application involving weak infrared optical signal sensing and detection, including photon counting optical coherence-domain reflectometer [18], singlet oxygen detection [19], infrared spectroscopy [20, 21], measurement of time-resolved photoluminescence [22], and study of photon statistics [23].

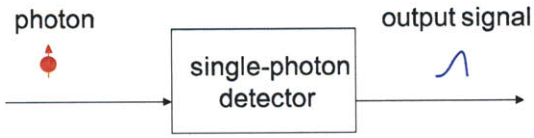

Figure 1-1: Schematic of a single-photon detector. The function of a single-photon detector is to change single-photons (can also be multiple photons) to observable output signals, typically voltage pulses.

1.2 Terminology for describing the performance of an SNSPD

This section defines the terminology used throughout the thesis to describe the performance of an SNSPD. An SNSPD requires a cryogenic system to maintain the working temperature at between 2 K and 4 K. The input of the system is single photons through an optical fiber, and the output of the system is voltage pulses through

a subminiature version A (SMA) cable. We can simply abstract the detector system as a black box as shown in Figure 1-1 in order to define the terminology.

- Dark-count rate

  Dark-count rate, D, is defined as the output counts per unit time that have no corresponding input photons. As illustrated in Figure 1-2, the output signal between 1 and 2 does not have a corresponding input, and therefore it is attributed to a dark count. The dark counts measured experimentally are mostly due to stray light and coupled blackbody radiation. The mechanism of *intrinsic* dark counts in SNSPDs has not been completely understood yet. The intrinsic dark counts could be due to the fluctuations inside the nanowire such as phase-slip centers [24].

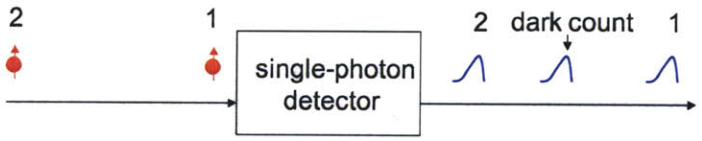

Figure 1-2: Schematic presentation of dark counts. Output signals (blue pulses) 1 and 2 correspond to input photons (red filled circles with arrows) 1 and 2. Between output signals 1 and 2, there is an output signal count without corresponding input. This output signal is called a dark count, viewed as a noise count.

- System detection efficiency

  System detection efficiency is defined as the ratio of the number of voltage pulses coming out from the system, with exclusion of dark counts, over the number of photons sent into the system. As illustrated in Figure 1-3, five photons are sent into the single-photon detector, but only 2 output pulses result, meaning that the system detection efficiency is not 100%. System detection efficiency, η, is a product of three numbers [2]: coupling efficiency, absorptance, and intrinsic quantum efficiency. Coupling efficiency, η_c, is the probability of incident photons that arrive at the active area of the detector; absorptance, A, is the probability that a photon is absorbed once it reaches the active area of the detector; intrinsic quantum efficiency, P_r, is the probability that the photon

generates a detectable voltage pulse once the photon is absorbed. Coupling efficiency is determined by the spatial overlap between the detector and the optical mode [25]. Absorptance is dependent on the photonic structure of the device, polarization, and wavelength of the incident photons. Intrinsic quantum efficiency is dependent on the quality of the film, i.e., defect probability, and the quality of the fabrication process, i.e., the uniformity of the width of the nanowire, the width of the nanowire, and the wavelength of incident photons. Coupling efficiency and absorptance can be modeled accurately; P_{r}, however, has not been fully understood yet. The product of A and P_{r} is called device efficiency.

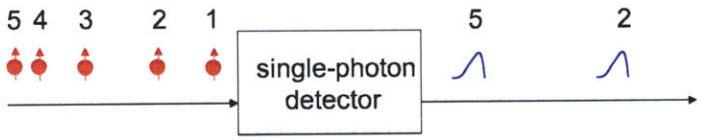

Figure 1-3: Schematic presentation of system detection efficiency. Five input photons (red filled circles with arrows), 1-5, are sent into the single-photon detector, but only two output signals (blue pulses), 2 and 5, result. The system detection efficiency is defined as the number of output signals due to the firing by the input signals (i.e., total number of output signals minus the number of dark counts; for simplicity, no dark counts are shown here) over the number of input photons.

- Reset time

  After being fired, an SNSPD cannot detect another incident photon immediately because the bias current cannot flow back to the nanowire and device efficiency (in fact, due to P_{r}) cannot recover immediately. As illustrated in Figure 1-4, photon 2 follows photon 1 so closely that the single-photon detector cannot respond to photon 2 after responding to photon 1 and yielding an output signal. The reset time, τ, is defined as the time needed for the device efficiency to recover to 90% of the device efficiency if there were no firing. Note here that the second photon can also be blocked by a dark count. Reset time is determined by the kinetic inductance of the nanowire [5], and is well understood.

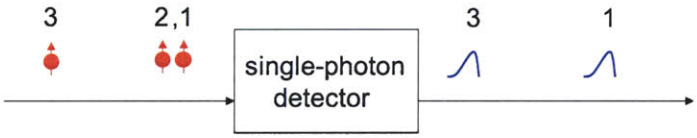

Figure 1-4: Schematic presentation of reset time. There are three input photons (red filled circles with arrows) labeled as 1, 2 and 3. Because photon 2 follows photon 1 so closely, and because the single-photon detector takes some time (called reset time) to detect another photon after being fired by photon 1, there is no output corresponding to photon 2.

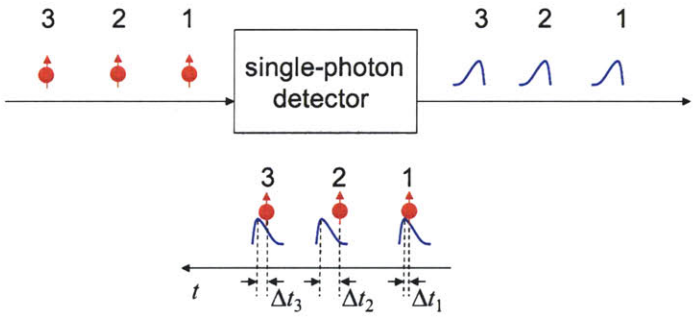

Figure 1-5: Schematic presentation of timing jitter. On the upper panel, output signals (blue pulses) 1, 2, and 3 correspond to input photons (red filled circles with arrows) 1, 2, and 3, respectively. For simplicity, we assume that there are no dark counts, no missing output counts due to the imperfect efficiency or the blocking effect due to the finite reset time. However, the single-photon detector is still not perfect. If we look carefully at the input photons and output signals in the time domain, we will find a varying time delay between the input photons and their corresponding output signals. This variation of the delay is called timing jitter.

- Timing jitter

  A time delay exists between an incident photon and its corresponding output signal; furthermore, this time delay varies. As illustrated in Figure 1-5, if we examine the input photons and output signals carefully in the time domain, we will find a varying time delay between the output signals and the corresponding input photons. The distribution of this time delay is approximately a Gaussian distribution. Timing jitter is defined as the full width at half maximum of this distribution [6]. The origin of the timing jitter of SNSPDs has not been fully understood. Timing jitter could be related to the formation of resistive regions

called hotspots [1, 26]. There is evidence that the timing jitter is dependent on the bias current and the width of the nanowire.

1.3 Materials, existing device structures, and detection mechanism

An SNSPD is made of niobium nitride (NbN) thin film on top of sapphire substrate [1, 2, 7]. The material can also be niobium (Nb) [27], niobium titanium nitride (NbTiN) [28, 29], and probably some other superconducting materials that people have not tried yet. The substrate can also be magnesium oxide (MgO) [28, 30], silicon dioxide (SiO_2) [29], silicon (Si) [31], gallium arsenide (GaAs) [32], and probably some other substrates. Superconducting films are deposited onto the substrate by DC magnetic sputtering. Different combinations of materials and substrates yield detectors with different performance. The material and substrate used throughout this thesis are NbN and R-plane sapphire, respectively. The thickness of the film is between 4 nm and 6 nm.

The device structure of the detector is determined by the detection mechanism, which is described by the so-called hotspot model [1, 26] and is explained by Figure 1-6. A NbN nanowire is biased with a bias current, I_b, close to its critical current, I_c [Figure 1-6 (a)]. If a photon is absorbed by the superconducting nanowire, the photon will first excite an electron, and this hot electron will collide with other electrons and break Cooper pairs, forming a hotspot inside the nanowire [Figure 1-6 (b)]. The current is therefore squeezed into the sidewall of the nanowire, and the current density exceeds the critical current density of the nanowire [Figure 1-6 (c)]. The whole cross-section of the nanowire becomes resistive, and current starts to be diverted into the low impedance line, which is in parallel with the nanowire [Figure 1-6 (d)]. The residual current inside the nanowire flowing through the resistive region generates Joule heat, which further makes the resistive region expand [Figure 1-6 (d)]. More and more current flows into the low impedance line, and eventually there is no current inside

the nanowire, and thus, no Joule heating anymore [Figure 1-6 (e)]. The nanowire is cooled and its superconductivity is restored [Figure 1-6 (f)]. The current flows back to the superconducting nanowire and the nanowire is ready to detect another photon [Figure 1-6 (a)].

The size of the hotspot determines that the width of the nanowire has to be $\leq$100 nm in order to detect incident photons efficiently. The process of hotspot formation has not been quantitatively understood yet; however, we know that the size of the hotspot is related to the wavelength of the radiation, or equivalently, the energy of the incident photon [26].

The heat dissipation time determines the lower limit of the reset time, and therefore, sets the lower limit of the length of the nanowire. The expansion of the resistive region due to the Joule heating, the diversion of the current, the cooling of the nanowire, and the current recovery are well explained by the electrical-thermal model [33, 34]. The thermal time constant for cooling, τ_{th}, needs to be smaller than the current recovery time constant, $\tau_{\mathrm{L/R}}$, i.e., $\tau_{\mathrm{th}} < \tau_{\mathrm{L/R}}$. Otherwise, if the current flows back to the nanowire too fast when the resistive region has not completely disappeared, the resistive region will be stabilized by the current so that the nanowire cannot go back to the superconducting state. Instead, the nanowire is in a state called the latched state [33], with nonzero resistance, that cannot be used for single-photon detection.

The requirement of absorbing the incident photon determines that the meander structure of the detector and additional integrated optical components are needed in order to capture the incident photons. Figure 1-7 shows the schematic of the meander structure. The purpose of the meander design is to cover a certain area to facilitate optical coupling. Figure 1-8 shows the cross-section schematic of the NbN nanowire meander without (a) and with (b) integration of a quarter-wavelength cavity. The purpose of the cavity is to enhance the absorption of the NbN nanowire. Absorption can be accurately modeled by electromagnetic simulation. Part of this thesis is devoted to the enhancement of the absorption of short NbN nanowires by integrating them with optical components.

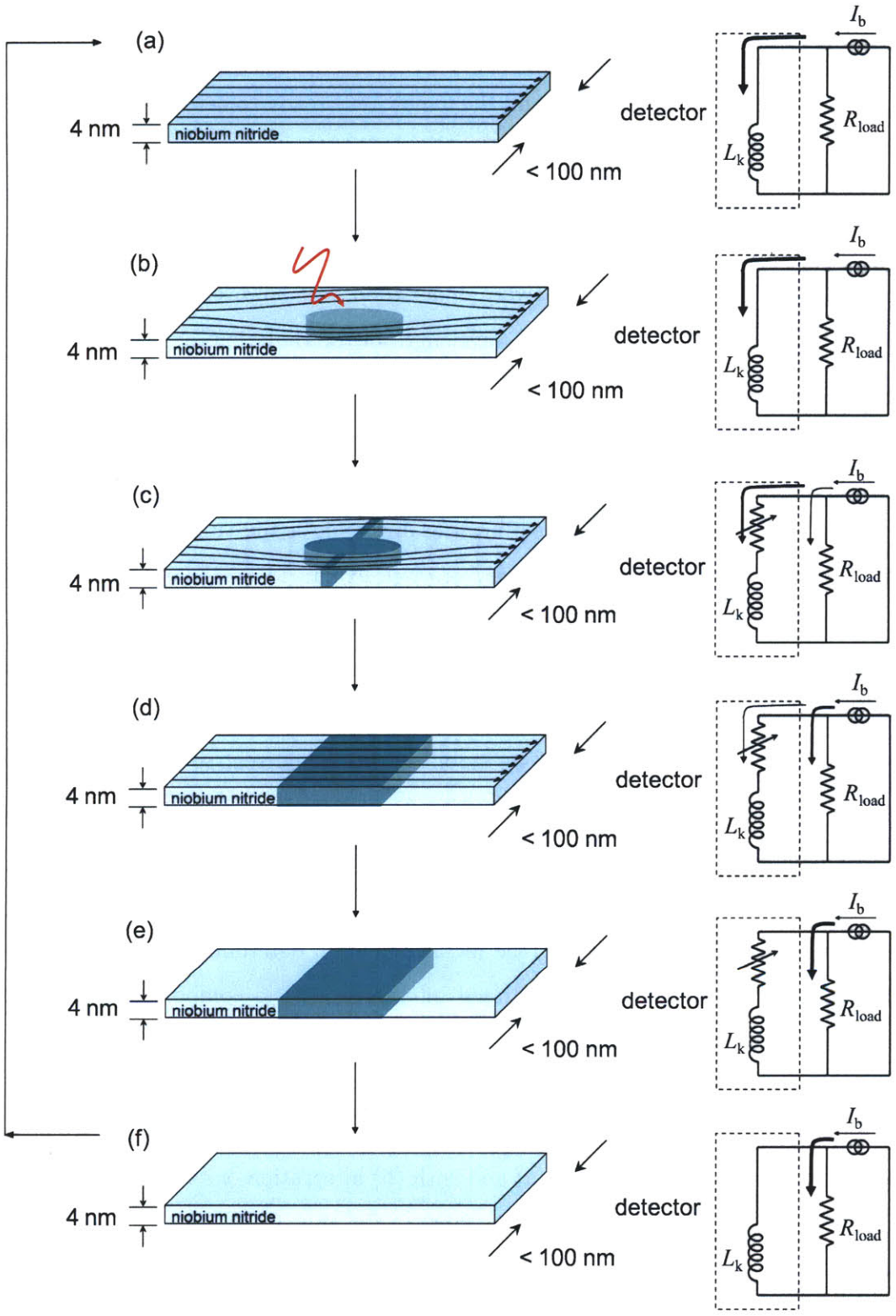
(a)
4 nm
niobium nitride
< 100 nm
detector
I_b
R_{load}
L_k
(b)
4 nm
niobium nitride
< 100 nm
detector
I_b
R_{load}
L_k
(c)
4 nm
niobium nitride
< 100 nm
detector
I_b
R_{load}
L_k
(d)
4 nm
niobium nitride
< 100 nm
detector
I_b
R_{load}
L_k
(e)
4 nm
niobium nitride
< 100 nm
detector
I_b
R_{load}
L_k
(f)
4 nm
niobium nitride
< 100 nm
detector
I_b
R_{load}
L_k

Figure 1-6: Detection mechanism and the circuit model of a superconducting-nanowire single-photon detector. (a) A niobium-nitride nanowire (width < 100 nm) is biased with a bias current close to the critical current of the nanowire. In the circuit model, the superconducting nanowire can be modeled as an inductor. The resistor in parallel with the inductor is the 50-Ω impedance of the transmission line. (b) Once a photon is absorbed, the photon generates a resistive region. The current is squeezed into the sidewall where the current density will exceed the critical current density of the nanowire. (c) The whole cross-section becomes resistive. Because current flows in this resistive region, the current generates Joule heat, which further makes the resistive region expand. In the circuit model, the resistive nanowire is modeled as an inductor with a serial resistor. The resistance of the resistor changes as the resistive region expands. Some of the current gets diverted into the low impedance line. (d) The Joule heating makes the resistive region further expand. More and more current is diverted into the low impedance line. (e) Eventually, all the current is in the low impedance line, and there is no Joule heating anymore. (f) Because of the cooling, the absorbed energy dissipates as thermal energy and the nanowire goes back to the superconducting state. The current flows back to the nanowire, and the system returns to its initial state (a). In this way, the superconducting nanowire can continuously detect single photons.

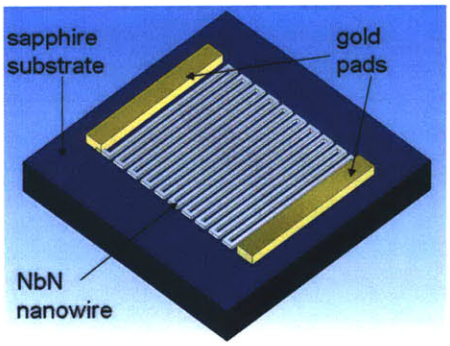

Figure 1-7: Schematic of a SNSPD in a meander structure. This figure is excerpted from [25].

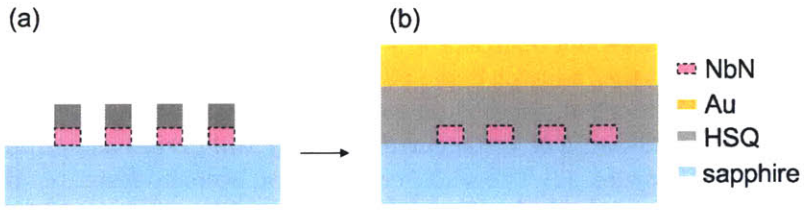

Figure 1-8: Cross-section schematic of a NbN nanowire meander without (a) and with (b) integration of a quarter-wavelength cavity.

1.4 Performance of state-of-the-art SNSPDs and comparison with other technologies

This section summarizes the status of the field of SNSPDs and make a comparison with other infrared photon counting technologies. This summary is primarily based on [35, 36] and the references therein.

In addition to SNSPDs, several technologies co-exist for infrared single-photon detection, including photomultiplier tubes (PMTs), InGaAs/InP avalanche photodiodes (APDs), transition edge sensors (TESs), and frequency up-conversion (UC) detectors. This is not a complete list. These technologies are based on different principles, which will not be elaborated here. Instead, the best performance of each type is listed in Table 1.1.

Table 1.1: Performance of state-of-the-art SNSPDs and comparison with other technologies at the wavelength of 1550 nm.

Characteristic	SNSPD	TES	APD	PMT	UC
efficiency	~20%[a], ~50%[b]	95%	~10%	2%	2%~10%
speed (MHz)	100	0.1	100	10	10
jitter (ps)	30	10^5	55	300	40
noise counts (/sec)	$10^2 \sim 10^3$	3	6% afterpulse	2×10^5	10^5
resolve photon numbers?	yes[c]	yes	yes	yes	no
working temperature (K)	2-4	0.1	243	200	300

[a]For single-element SNSPDs.
[b]For multi-element SNSPDs.
[c]Single-element SNSPDs cannot resolve photon numbers without using a time-multiplexing scheme; multi-element SNSPDs [37] and SNSPDs composed of parallel nanowires [38] can.

SNSPDs have good comprehensive performance. Compared with PMTs, APDs, and UC detectors, SNSPDs have better efficiency and lower dark-count rate. TESs have even higher efficiency and lower dark-count rate, but their speed and timing jitter are much worse than those of SNSPDs. Thus, compared with TESs, SNSPDs are more suitable for applications in which speed and precise timing are required, for example, in communication systems.

1.5 Outline of this thesis

This thesis is about SNSPDs and their applications in quantum optics.

Chapter 2 focuses on a fiber-coupled SNSPD system [7]. The SNSPD is a circular shaped detector with a 9-μm diameter integrated with a quarter-wavelength cavity on top. The input channel of the system is a single-mode fiber and the output channel of the system is an SMA cable. System detection efficiency of 24% with dark-count rate of ~1000 counts/sec (cps) has been demonstrated.

Chapter 3 focuses on experimental polarization-entanglement distribution using this SNSPD system [11]. One feature of the experiment is that we only used one detector and a time-multiplexing scheme to detect entangled-photon pairs. The photon pairs at the wavelength of 1.3 μm were generated by parametric down-conversion in-

side a periodically-poled potassium titanyl phosphate (PPKTP) waveguide, and then, were distributed to the detector. The detected pair rate using one single SNSPD in the measurement of Hong-Ou-Mandel interference was 150 times the detected pair rate using two InGaAs single-photon detectors [39]. We obtained a pair rate of 5.8 pairs/sec at a pump power of 25 μW and two-photon quantum interference visibility of 97.7% after distribution, neither with subtraction of accidentals.

Increasing the active area of the detector allowed us to couple light into the detector efficiently and enabled an efficient detector system. On the other hand, if we keep the original design of the meander, increasing the active area inevitably increases the length of the nanowire and therefore, the kinetic inductance of the nanowire. Thus, a large-area detector is slow. The rest of the thesis focuses on novel photonic structures that allow us to use a short nanowire to achieve an efficient detector.

Chapter 4 focuses on a design and realization of an SNSPD integrated with optical nano-antennae [10]. By adding additional gold structures, a sparse meander can absorb light efficiently. A detector with a 600-nm pitch covering an active area of 9 μm by 9 μm was demonstrated. The device efficiency of the detector was measured to be 47% for transverse-magnetic (TM) polarization and 4% for transverse-electric (TE) polarization. This type of SNSPD is the only one that dominantly responds to TM polarization so far. The reset time of this SNSPD was 5 ns. This detector is ideal for applications where efficiency and speed are simultaneously needed. This idea has been extended to absorption enhancement of an ultra-narrow nanowire for detecting single photons at mid-infrared wavelengths.

Chapter 5 focuses on the concept, design, and developement of the fabrication process of waveguide-integrated SNSPDs [10] for fiber-coupled systems and on-chip applications. Coupled with a single-mode fiber, the system detection efficiency can reach 75% with a 50-μm long NbN nanowire. The corresponding reset time is estimated to be 3.4 ns. The dominant loss is the coupling loss between fiber and the waveguide taper. For on-chip quantum optics, if the light source is also integrated with a waveguide, the system detection efficiency can be even higher.

Chapter 6 summarizes and concludes the thesis, and discusses future directions.

Chapter 2

Superconducting-nanowire single-photon detector system

This chapter presents the fiber-coupled SNSPD system in a closed-cycle crycooler to address the challenge of the cryogenic operation of the detector. Twenty-four percent system detection efficiency has been demonstrated with a dark-count rate of ~1000 cps once the detector is fully biased. To follow the procedure of building this system, the chapter presents the design and fabrication of a large-area detector, the design of the chip package, and the measurement of the dark-count rate and the system detection efficiency. Finally, a document attached in Appendix A explains how to operate and maintain the system. Most of the work presented in this chapter has already been documented in [7].

Building such a system includes at least two challenges. The first challenge is generally true for any engineering work in which the whole procedure is composed of cascaded steps. Each step looks simple, with a small probability of error; however, the whole procedure is not simple because there is a large probability that a fatal error may occur during the constructing and debugging processes. The second challenge is the optical alignment at low temperature in a completely enclosed chamber. To address this challenge, we used three cryogenic nanopositioners to perform *in-situ* optical alignment.

These challenges probably explain why the system detection efficiency has re-

mained low since SNSPD technology was invented in 2001 although there have been significant efforts in the field to push this efficiency higher. Before this project started at the Massachusetts Institute of Technology (MIT), National Institute of Standards and Technology in the US has reported $< 10\%$ system detection efficiency in a closed-cycle cryocooler system [35]; European teams have reported $\sim$20% system detection efficiency by immersing the detector in liquid helium in a dewar [40]; MIT Lincoln Laboratory has reported 25% system detection efficiency for a 4-element detector array [41]. While this work was being done at MIT, several other teams were also working on packaging SNSPDs in closed-cycle cryocoolers to further enhance the system detection efficiency and reduce the dark counts. For example, National Institute of Information and Communications in Japan reported their results [8] almost at the same time as we published our results [7].

2.1 Device design and fabrication

The device structure used for this system is a 200-nm-pitch, 50%-fill-factor meander integrated with a quarter-wavelength cavity [2]. The standard process with hydrogen silsesquioxane (HSQ) as the e-beam resist [42] was used. The active area of the detector was expanded from 3 μm by 3 μm to 9-μm in diameter.

The SNSPD was designed to be a circular shape with a 9-μm diameter for the system in order to efficiently couple light to it. The key to coupling light to an SNSPD, or to any detector, is to maximize the overlap between the spatial mode of the light and the active area of the detector. This overlap is determined by two factors: (1) the size of the active area of the detector relative to the size of the optical mode and (2) the relative alignment of the detector with the optical beam. Lateral, longitudinal, or angular misalignments [25] decrease this overlap, and therefore the coupling efficiency. For the optical mode, we used the fiber focuser in our system to shrink the beam's waist (full width at $1/e^2$ of the intensity profile) of the light from the single-mode fiber down to 5 μm. The advantage of the slightly larger active area over the beam's waist is that it ensured that more than 99% of the incident light could overlap the

detector if there were perfect alignment between the beam and the detector, and a lossless fiber focuser. This design also provides some, but not complete, tolerance to mechanical vibration of the optical system relative to the detector. The advantage of the circular design was to minimize the length of the nanowire needed to cover a given area while maximizing coupling to the optical mode. Reduction of the total length of the nanowire further offered two advantages: (1) a faster detector because the speed of the detector is approximately inversely proportional to its length [5], meaning that compared with a 9-μm-by-9-μm square design, the speed of this circular detector is expected to be 1.16 times faster because the length of its nanowire is 1.16 times shorter, and (2) a decreased probability of constrictions, which are among the limits of the device efficiency [9].

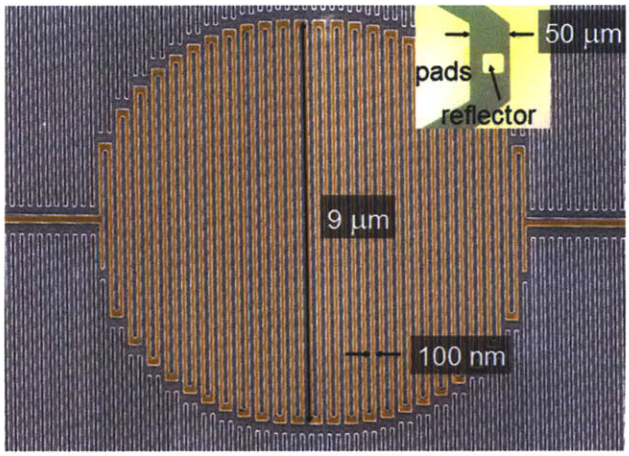

Figure 2-1: Micrograph of the fabricated superconducting-nanowire single-photon detector. The scanning-electron micrograph of the fabricated superconducting-nanowire single-photon detector was obtained before putting on the cavity. The diameter of the detector is 9 μm and the width of the nanowire is 100 nm. The detector itself is colored on the micrograph, and the surrounding linear structures are for proximity effect correction in scanning-electron-beam lithography. Inset: an optical micrograph of the detector after putting on the quarter-wavelength cavity.

Standard HSQ process [42, 2] was used to fabricate a circular SNSPD with a diameter of 9 μm, as shown in Figure 2-1. The width of the nanowire was ~100 nm, and the pitch of the meander was 200 nm. The total length of the nanowire was approximately 371 μm. Although the total length of this single nanowire was similar

to the overall length of four nanowires in the four-element detector used in [41], in the present case, a defect on the nanowire would constrict the entire device and thus limit the overall efficiency of this large-area detector. In the multi-element detector, a single constriction would affect only one element out of four. Therefore, fabricating a uniform defect-free nanowire is more critical to the performance of this single-element configuration.

A quarter-wavelength microcavity was integrated on top of the meander to enhance the optical absorption of the nanowire [2]. The cavity length that optimizes the absorptance of transverse-electric (TE) polarization was found by optical simulation to be 270 nm. In the process of adding the cavity to the meander, we spun on ~300-nm HSQ, exposed it by scanning-electron-beam lithography (SEBL, Raith 150 SEBL facility at the Massachusetts Institute of Technology), and then used reactive ion etching (RIE, Plasma Therm reactive-ion etcher) to etch it down to the appropriate thickness, which was measured by a profiler. Having optimal cavity length is important to achieving good device efficiency. Figure 2-2 presents the chip after the processing was completed.

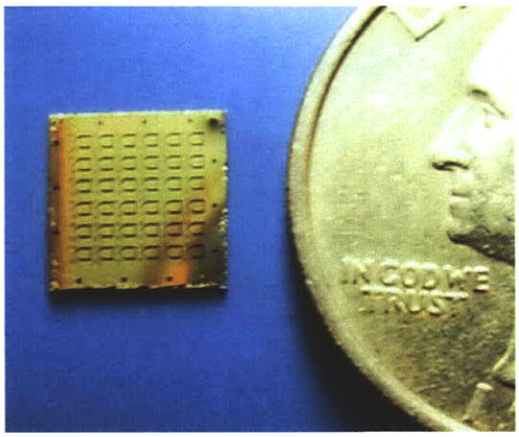

Figure 2-2: Photograph of the chip of superconducting-nanowire single-photon detectors (36 in total) after the processing was completed. One detector with the highest device efficiency was selected for the system among the 36 detectors on the chip. The size of the chip is 10 mm by 10 mm, smaller than a quarter.

The detector with the best device efficiency among 36 detectors on the chip was selected. The device efficiency of each detector was measured using a cryogenic probe

station at the baseplate temperature of 2.1 K and at the bias of 95% of each I_c. The device efficiency of this particular detector selected at the wavelength of 1550 nm was measured to be 30%. The small (0.6 K) temperature difference between the probe station and the cryocooler did not make an observable difference in critical current, and, therefore, it is reasonable to assume that the maximum device efficiency was also 30% in the cryocooler.

2.2 Chip package

Figure 2-3 shows a schematic of the chip package with all parts labeled. The function of each part is very much explained by its name. Figure 2-4 shows a photograph after we assembled the chip package but before putting on the semi-rigid radiation shield. Photographs of the core of the chip package, the chip plate, are shown in Figure 2-5. On the chip plate were mounted the SNSPD chip, a temperature sensor, three nanopositioners, the fiber focuser, and an SMA connector. The chip was sitting in the middle of the chip-plate, and glued to the plate by silver conducting paint, which provided thermal contact. The chip plate was mounted by screws to a hollow aluminum cylinder (the connector). The connector was then screwed onto the cold head. In this way, the detector sat in an enclosed metallic chamber facing the cold head except for a small hole under the chip to permit bottom illumination from the fiber focuser. This design of the enclosed metallic chamber for the detector was to reduce the dark counts. The detector was wire bonded directly to the SMA connector, which was connected by a semi-rigid coaxial cable that was heatsunk by being wrapped and taped around the connector and the second and first stages of the cryocooler. We used semi-rigid aluminum foil as the radiation shield for the chip package. This shield was clamped conformably to the first stage of the cryocooler by using a steel hose clamp. The resulting temperature of the radiation shield was $\sim$20 K; the resulting base temperature of the chip plate was 2.7 K.

A photograph of the SNSPD system after all parts were mounted is shown in Figure 2-6. The system can be viewed as a black box presented in Figure 1-1, with

the single-mode fiber as the input channel and the SMA cable as the output channel.

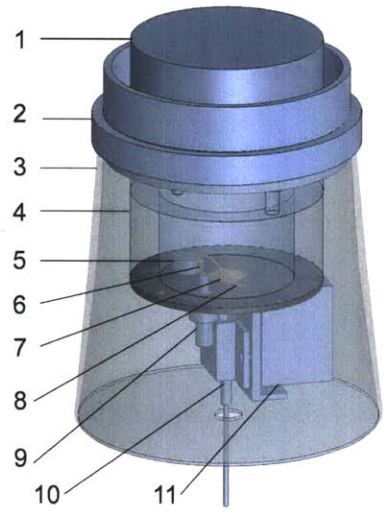

Figure 2-3: Schematic of the chip package with all parts labeled: 1. cold head; 2. clamp; 3. semi-rigid radiation shield; 4. connector; 5. temperature sensor; 6. signal wirebond; 7. chip; 8. ground wirebound; 9. RF readout; 10. fiber focuser; 11. positioners.

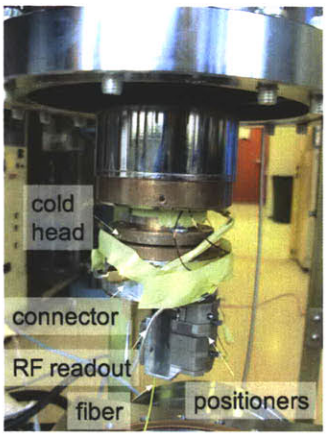

Figure 2-4: Photograph of the chip of the chip package mounted on the cold head of the cryocooler before the semi-rigid radiation shield was put on. Cf. the schematic in Figure 2-3.

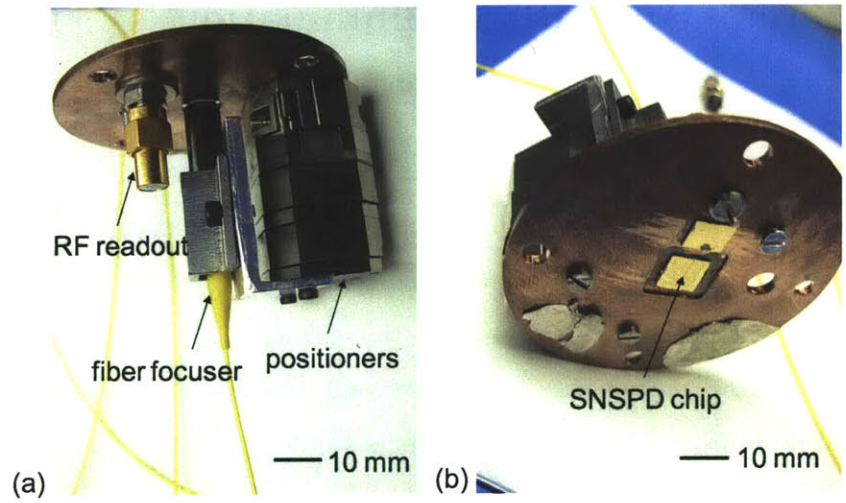

Figure 2-5: Photographs of the chip plate on which were mounted three nanopositioners, a temperature sensor, and the chip at the center. The fiber focuser is mounted on a nanopositioner and can be moved by the nanopositioners three dimensionally. (a) and (b) show two sides of the chip plate.

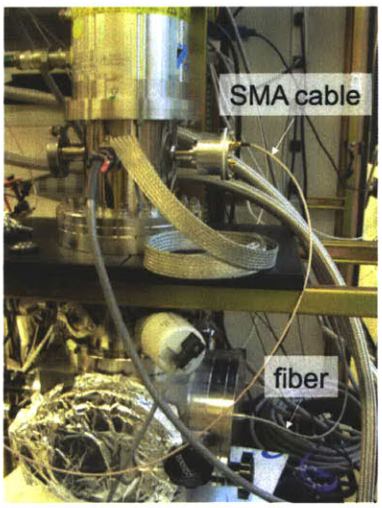

Figure 2-6: Photograph of the SNSPD system after all parts were installed. The system can be viewed as a black box with the single-mode fiber as the input channel and the SMA cable as the output channel. Cf. the schematic in Figure 1-1.

2.3 Circuit and optical illumination

The circuit and optical illumination in this system are similar to the setup documented in [25] for immersion testing of SNSPDs in liquid helium with a few modifications. The schematic of the setup is shown in Figure 2-7. A low noise current source was used to bias the detector, and an attenuated continuous wave (cw) laser was used as the light source to measure the system detection efficiency. The optical path consisted of a laser, a precision attenuator, a polarization controller, and the fiber focuser, all of which were connected by single-mode fibers.

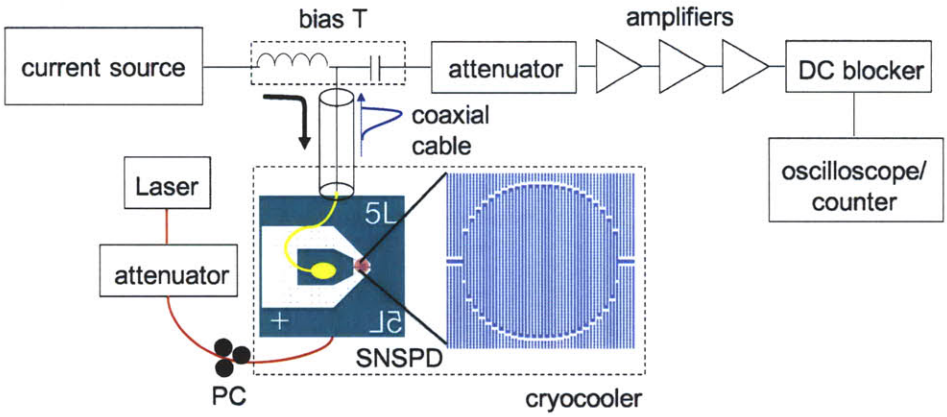

Figure 2-7: Schematic of the circuit and the illumination.

2.4 Output pulse and reset time

Figure 2-8 shows an output signal of the system, a voltage pulse. The full width at half maximum of the voltage pulse was ~5 ns. This pulse width is not the reset time of the detector because the filtering effect of the amplifiers made the voltage pulses appear shorter than the reset time. The reset time was expected to be 27 ns according to our calculation based on the kinetic inductance of the nanowire [5]. See Appendix B for details of the calculation.

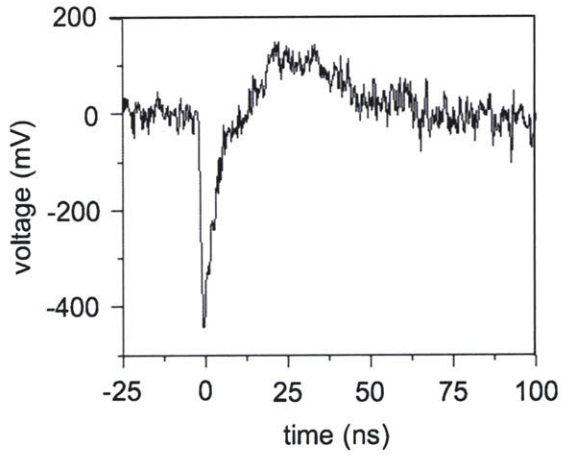

Figure 2-8: Output voltage pulse of the system. The full width at half maximum of the voltage pulse is ~5 ns.

2.5 Dark-count rate

The maximum dark-count rate measured when we increased the bias current up to 99% of the critical current was ~1000 cps, as shown in Figure 2-9. We took a number of steps to minimize the counts due to stray light coupled into the detector. As mentioned above, the chip package was designed so that the chip could only be illuminated from the back by the fiber focuser. The entire chip package including the nanopositioner stack and the fiber focuser was enclosed in the radiation shield. The fiber entered the radiation shield through a hole with a diameter of 8 mm and connected with the fiber outside the chamber through a vacuum feedthrough. After mounting the fiber focuser and the radiation shield, we covered this 8-mm-diameter hole with aluminum foil. The piece of fiber outside the cryocooler was in a metal jacket (see Figure 2-6), and when we measured the dark-count rate, we capped the FC/PC fiber connector at the end with a metal cap. We also used aluminum foil to cover the two quartz windows of the cryocooler to prevent the stray light from leaking into the fiber. With all of these strategies, the dark-count rate that we measured was ~150 cps and ~1000 cps when we biased the detector at 96% and 99%, respectively, of I_c, which was 14.6 μA. For comparison, without covering the quartz window or the

FC/PC fiber connector, the dark-count rate was above 2000 cps when we biased the detector at 99% of its I_c.

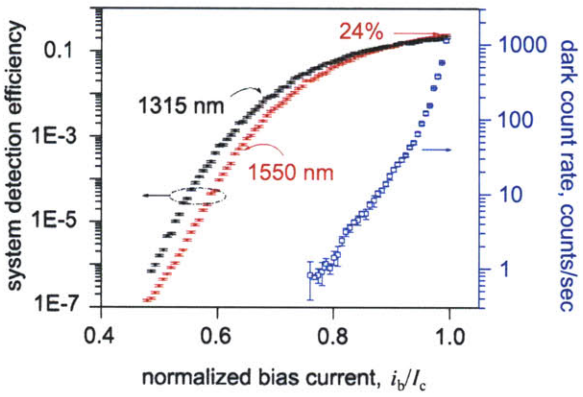

Figure 2-9: Measured system detection efficiencies and dark-count rate as a function of bias current. The system detection efficiencies for two wavelengths, 1550 nm and 1315 nm, were measured. At the bias of 99% I_c, the system detection efficiency reaches its maximum 24% at the wavelength of 1550 nm and, correspondingly, the dark-count rate is ~1000 counts/sec. The critical current, I_c, was 14.6 μA at the temperature of 2.7 K.

2.6 Optical alignment

Three cryogenic nanopositioners (two ANPx101 and one ANPz101, all from Attocube System) were used in our setup to precisely control *in-situ* the three-dimensional position of the beam waist of the incident beam. The fiber focuser was clamped into a V-groove, mounted on the nanopositioner stack, as shown in Figure 2-5 (a). When voltage pulses were applied, the nanopositioners performed stick-slip motion with a step size as small as ~10 nm at the temperature of 2.7 K. This much smaller step size compared with the wavelength of the light provided the requisite precision of position control. We scanned the beam three dimensionally until we found the maximum of the photon count signal. A practical guide of how to perform optical alignment for this system is in Appendix A.

2.7 System detection efficiency

We measured the system detection efficiency by using a greatly attenuated cw laser as the light source. Before adding attenuation, we used an optical power meter to measure the optical power P (in μW) coming out of the polarization controller. We controlled this power to be about 100 μW, and added attenuation A (in dB), which was typically 100 dB. Therefore, the incident power to the detector was on the order of 10^{-14} W, or equivalently, the flux of photons was about 10^5 photons/sec, which was much higher than the dark-count rate and much lower than the maximum counting rate, $\sim 1/\tau$, which was $\sim$37 MHz, of the detector.

Because the response of the detector was polarization dependent, we maximized the counts by adjusting the polarization of the incident photons using the polarization controller. The ratio of the maximum to minimum counting rate due to polarization variation was measured to be $\sim$2 at both 1550-nm and 1315-nm wavelengths. This ratio is primarily determined by the fill-factor of the meander, which was 50% in our device. This ratio is consistent with our optical simulation of the absorptance of the meander. The output voltage pulses of the detector after 50-dB amplification by three radio frequency (RF) amplifiers were counted by a photon counter. If the counting rate is denoted as N and the wavelength of the light is denoted as λ, the system detection efficiency, η, is simply calculated by

$$\eta = 10^{0.1A} hcN/(P\lambda), \tag{2.1}$$

where h is the Planck constant and c is the speed of light in vacuum. In this way, the system detection efficiencies at wavelengths of 1550 nm and 1315 nm were determined, as shown in Figure 2-9, as a function of bias current. At a bias at 99% of I_c, the system detection efficiency reached its maximum of 24% for 1550 nm and 22% for 1315 nm. We repeated the measurement of total counts and dark counts five times, and the efficiency and dark-count rate shown on the figure were obtained by averaging. The error for the efficiency measurement was calculated assuming $\pm$0.1 dB uncertainty in the precision attenuator, $\pm$5% uncertainty in the optical power meter, and one

standard deviation (SD) of the observed fluctuation in counting rate, which we believe was due to the intensity fluctuation of the laser, coupling efficiency fluctuation induced by the mechanical vibration of the piston, and intrinsic shot noise. These errors were summed in quadrature. At a bias of 99% of I_c, the resulting maximum system detection efficiencies were $24\% \pm 1\%$ and $22\% \pm 1\%$ at wavelengths of 1550 nm and 1315 nm, respectively. The error of the dark-count rate in Figure 2-9 was taken to be the SD of the measurements. The SD for dark counts was consistent with the expected fluctuation due to shot noise.

2.8 Discussion

Both system detection efficiency and dark-count rate increase with increasing bias current. Noise-equivalent power (NEP) is a commonly used number to measure the signal-to-noise ratio of a detector. NEP of a single-photon detector is defined as

$$\text{NEP} = hc\sqrt{2D}/\lambda\eta. \tag{2.2}$$

The NEP of our SNSPD system at wavelengths of 1550 nm and 1315 nm were calculated and plotted in Figure 2-10. If the bias current $< 95\%I_c$, the NEP of this SNSPD system $< 10^{-17}\text{WHz}^{-1/2}$. The sharp increase of NEP at large bias current ($> 95\%I_c$) is because the dark counts in this regime increase almost exponentially whereas the system detection efficiency increases slowly and saturates. Therefore, from the point of view of NEP, we bias the detector at 95% of its I_c in applications.

We can infer that the coupling efficiency was ~80% by comparing the device efficiency and the system detection efficiency. This incomplete coupling might be due to two reasons: (1) optical loss in the fiber focuser, which was measured to be 10% at room temperature, and (2) the dynamic misalignment between the beam and the detector resulting from the mechanical vibration induced by the piston inside the cryocooler. However, from the point of view of the system detection efficiency, the major limiting factor was still the device efficiency, meaning that the absorptance

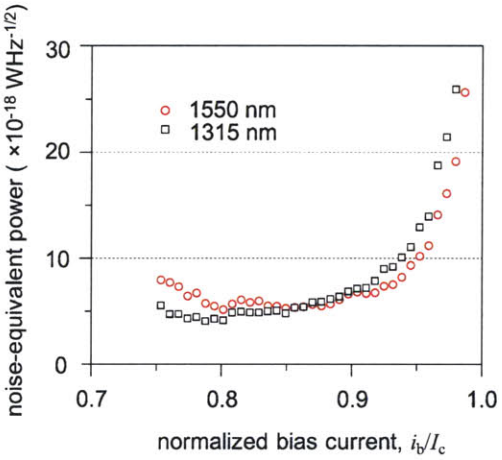

Figure 2-10: Calculated noise-equivalent power of the superconducting-nanowire single-photon detector system for two wavelengths, 1550 nm and 1315 nm. The calculation is based on the measured data in Figure 2-9.

of the NbN nanowire was not 100%, and small constrictions limited the intrinsic quantum efficiency, P_r. To further enhance the device efficiency while keeping a relatively large active area, it will be important to further improve the quality of the NbN film and increase the optical absorptance of the NbN nanowire, which will be discussed in Chapters 4 and 5. An application of this system in quantum optics, high-quality polarization-entanglement distribution, will be presented in Chapter 3.

Chapter 3

Polarization-entanglement distribution using the superconducting-nanowire single-photon detector system

Entanglement [43] is a unique phenomenon in quantum mechanics with no classical counterpart. It is the correlation beyond classical correlations between two particles or among multiple particles. Entanglement distribution is sending entangled particles to remote locations while the entanglement is preserved. This distribution is the basis of many applications such as quantum key distribution [44], quantum teleportation [45], and quantum repeaters [46]. Many experiments have already been reported upon the distribution of polarization-entangled photons at the spectral range where efficient Si APDs are available [47, 48, 44]. However, at telecom wavelengths, the reports [49, 50] of high-quality distribution of polarization-entangled photons are still rare because of the lack of high-quality polarization-entangled photon sources and because of the lack of high-performance single-photon detectors at these wavelengths. In particular, entanglement distribution at the wavelength of 1.3 μm is interesting because this wavelength is the second lowest loss window of telecom optical fibers and has minimal

interferences with the 1.55 μm infrastructure due to cross-talk and nonlinear spurious signals.

This chapter presents an experiment on photonic polarization-entanglement distribution using the SNSPD system described in Chapter 2. From the point of view of the entangled-photon source, this experiment confirmed the capability of a waveguide-based nonlinear crystal to generate high-quality entanglement. From the point of view of the detector, this experiment demonstrated the capability of the SNSPD system to make measurements in quantum optics orders-of-magnitude better than other detectors, due to its free-running mode, low dark-count rate, no observable afterpulsing, and high system detection efficiency. Most of the work presented in this chapter has already been documented in [11].

3.1 Experimental setup

Figure 3-1 presents the experimental setup for entanglement distribution. The setup is composed of two sub-systems: (1) the source for entanglement generation located at MIT in Building 36 and(2) the detector for coincidence detection in Building 38. They are connected by two pieces of standard telecom fibers, each of which is ~200-m long.

The polarization-entangled photon source was developed by my collaborators, Tian Zhong and Dr. Franco N. C. Wong. Photon pairs, horizontally (H) polarized signal and vertically (V) polarized idler, were generated in a 1.6-cm long, type II phase matched PPKTP waveguide pumped by a 658-nm cw laser diode. The photon pairs were at the wavelength of 1316.2 nm for a waveguide temperature of 26.5 °C. One important feature of this nonlinear crystal waveguide is that it is directly attached to and coupled with an input polarization-maintaining (PM) fiber for pump and an output PM fiber with a fiber-to-waveguide coupling efficiency of 45%. The functionalities of several optical components in source are as follows. A free-space, pump-blocking reflection Bragg grating (RBG) filter with a full width at half maximum bandwidth of 0.7 nm that was slightly smaller than the phase-matching bandwidth was used to

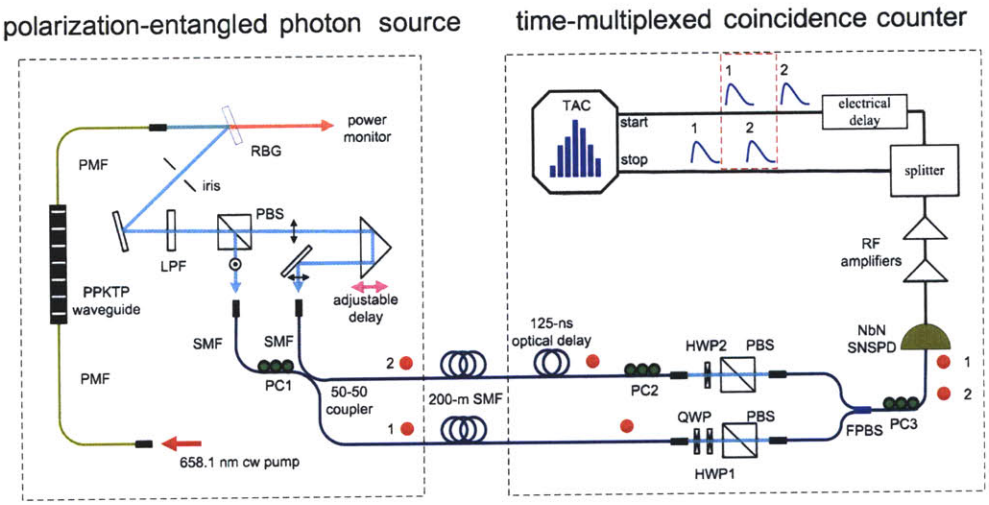

Figure 3-1: Schematic of the experimental setup for polarization-entanglement distribution. The whole setup is composed of two major parts: (1) source for polarization-entangled photons; (2) time-multiplexed coincidence counting. These two parts are located at two different buildings (source in Building 36 and detector in Building 38) at the MIT campus and are connected by two pieces of ~200 m fiber. PMF: polarization-maintaining fiber; PPKTP: periodically poled potassium titanyl phosphate; RBG: reflection Bragg grating; PBSL: polarization beam splitter; SMF: single-mode fiber; PC: polarization controller; HWP: half-wave plate; FPBS: fiber polarization beam splitter; NbN SNSPD: niobium-nitride superconducting-nanowire single-photon detector; TAC: time-amplitude converter.

ensure the spectral indistinguishability between signals and idlers. The effective efficiency of the RBG was 75%, taking into account the filter spectral shape and the 90% peak spectral transmission (98% if antireflection coating were applied). A long-pass filter (LPF) of 98% transmission at 1315 nm was placed after the RBG to further suppress any residual pump power. A polarizing beam splitter (PBS) was used to separate signals and idlers, which were then coupled into their respective SMF-28 fibers, and recombined at a 50-50 fiber non-polarizing beam splitter (NPBS). The signal and idler remained orthogonally polarized at the NPBS inputs by use of a polarization controller (PC1) in the idler arm. By considering only those events with one photon in each of the two output channels (labeled 1 and 2), we were able to postselectively generate the polarization-entangled triplet state $|\Psi\rangle = |\mathrm{H}\rangle_1|\mathrm{V}\rangle_2 + |\mathrm{V}\rangle_1|\mathrm{H}\rangle_2$ in the horizontal-vertical (H-V) basis [51] or equivalently $|\Psi\rangle = |\mathrm{A}\rangle_1|\mathrm{A}\rangle_2 - |\mathrm{D}\rangle_1|\mathrm{D}\rangle_2$ in the

antidiagonal-diagonal (A-D) basis. [1] An adjustable signal delay line, behind the PBS, provided the necessary timing compensation to erase the temporal distinguishability caused by dispersion in the type-II phase-matched waveguide.

The detector system used in this experiment is the one described in Chapter 2. We biased the detector at 95% of its I_c and obtained 19% system detection efficiency at the wavelength of 1316 nm with a dark-count rate of 150 counts/sec. An unattended fiber network linked the polarization-entanglement photon source and the SNSPD coincidence detection system physically located in two separate buildings. Figure 3-1 shows that the entangled photons in channels 1 and 2 were sent to the SNSPD system in two separate 200-m-long SMF-28 fibers. We were able to compensate for depolarization induced by the fiber transmission and maintain linear polarization at the detector location by using a quarter wave plate in channel 1 and a polarization controller (PC2) in channel 2. The polarization state of the entangled photons was analyzed with a combination of a half-wave plate (HWP) and a PBS in each channel.

The functionality of the time-amplitude converter (TAC) is as follows. The TAC has two input channels, "start" and "stop." The output counting of the TAC is time-correlated. If there is an input in the "start" channel followed by an input in the "stop" channel with a time delay, τ_d, the TAC counts 1 at the time τ_d. An example output of the TAC in our experiment is shown in Figure 3-2. The giant peak represents the counts of coincidences. A zoom-in presentation of the peak is shown in Figure 3-3. The TAC used in our experiment was Picoquant TimeHarp200 with a 38-ps timing resolution and a coincidence window of 1 ns, which was chosen to be $\pm$0.5ns around the peak. The coincidences are calculated by integrating the total counts inside the coincidence window.

The time multiplexed scheme of detection allowed us to use a single SNSPD for two-photon coincidence measurements. A usual way to measure coincidences is to use two single-photon detectors, as shown in Figure 3-4. If two photons fire two single-photon detectors at the same time, and if these two single-photon detectors

[1] Any polarization state can be written as a linear combination of a horizontal (0°) component and a vertical (90°) component in the H-V basis, or can be written as a linear combination of a antidiagonal (135°) component and a diagonal (45°) component in the A-D basis.

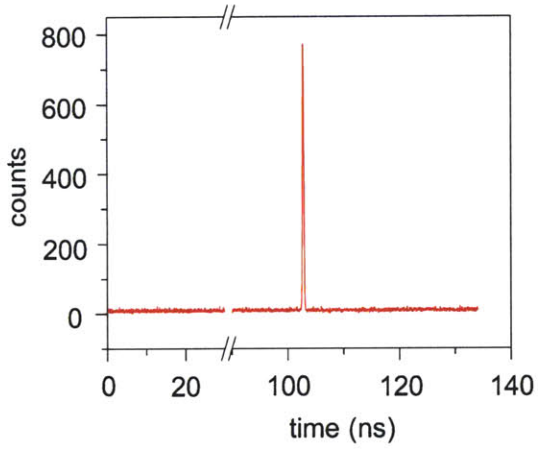

Figure 3-2: Example output of the time-amplitude converter.

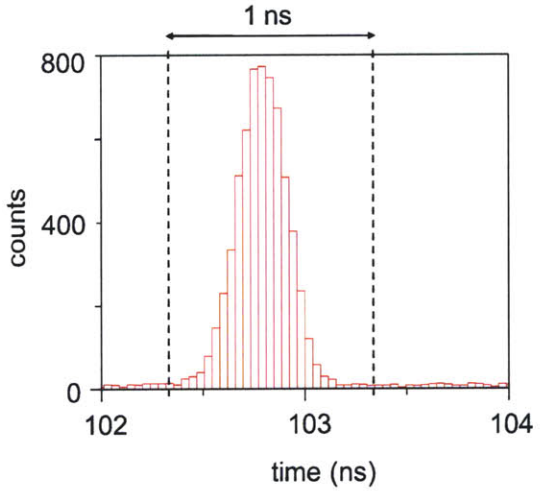

Figure 3-3: Zoom-in presentation of the peak in Figure 3-2. A coincidence window of 1 ns was chosen to be ± 0.5 ns around the peak.

yield outputs at the same time, then we get one coincidence. However, if a single-photon detector can run in free-running mode with low noise counts, we can use the time multiplexed scheme and only use one single-photon detector to measure coincidences. As shown in Figure 3-5 schematically, we artificially delay photon 2 by time τ_1, combine photon 1 and photon 2, and send them to the single-photon detector, one by one. Assume that two output signals are obtained. If the timing

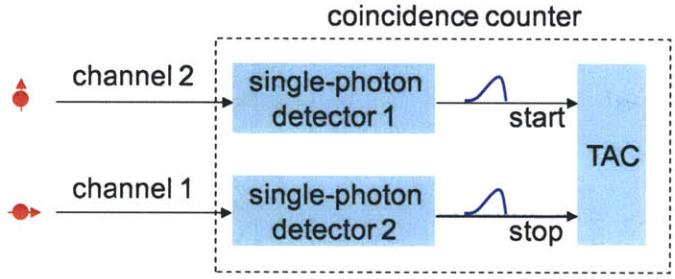

Figure 3-4: Schematic of usual way to measure coincidences by using two single-photon detectors.

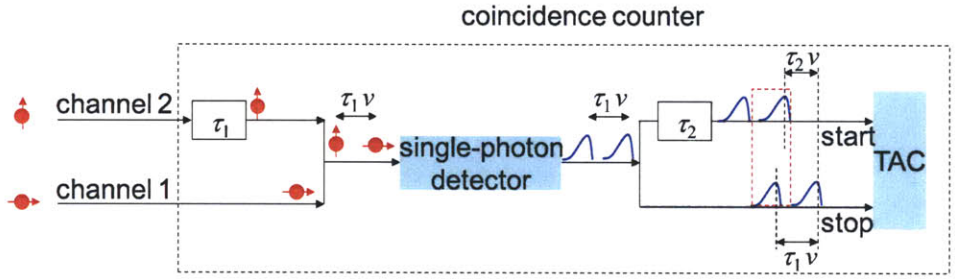

Figure 3-5: Time-multiplexing scheme to measure coincidences. Photon 2 is delayed by time τ_1, and is combined with photon 1. Photon 1 and photon 2 are sent into the single-photon detector, one by one. Assume that two output signals are obtained. If we neglect the timing jitter, the time difference between these two output signals is also τ_1. These two signals are then split into two channels. The signals in the "start" channel are delayed relative to the "stop" channel by time τ_2. Signals in these two channels are sent into a time-amplitude converter. If the time difference between two input signals of the time-amplitude converter is $\tau_1 - \tau_2$, this event is regarded as a coincidence. We use v to represent the speed of light in optical fibers or the speed of the RF signals in coaxial cables.

jitter of the single-photon detector is negligibly small compared with the coincidence window of the TAC, which is true in our case, the time difference between two output signals is also τ_1. Then we split the output signals, and delay the "start" channel relative to the "stop" channel by a time delay τ_2 ($\tau_2 < \tau_1$). If we find two pulses with a time difference between the "start" channel and the "stop" channel to be $\tau_1 - \tau_2$, we regard this event as one coincidence. In the experiment, we imposed a time delay of 125 ns for photon 2, relative to photon 1, before they were combined at a fiber polarizing beam combiner and subsequently sent to the fiber-coupled SNSPD. The

voltage-pulse outputs of the SNSPD were amplified by RF amplifiers, split into the "stop" channel and the "start" channel with $\tau_2 = 12$ ns, and sent to the TAC. The exact amount of τ_2 is not important because it would only shift the position of the peak (in Figure 3-2) if we changed τ_2, as long as $0 < \tau_2 < \tau_1$.

The transmission efficiency of the fiber-optic network for each channel, including connector losses, was 68%, and each of the two free-space-to-fiber coupling stages was 65% efficient. Including the efficiencies of the waveguide-to-fiber coupling, the RBG filter, other bulk optical components, SNSPD, and the time-multiplexed detection scheme, we estimate an overall system detection efficiency of $\sim$1.6%.

3.2 Hong-Ou-Mandel interference

As shown in Figure 3-6 schematically, if two identical photons with the same polarization and same frequency reach a 50-50 beam splitter at the same time from two input ports (1 and 2), they always come out together from either output port (3 or 4) because of their interference. There is no coincidence in this situation. If there is distinguishability between these two photons, there will be coincidence. For example, as shown in Figure 3-7, if we delay the photon from port 1 by time τ_3, there is a probability that the two photons will come out from port 3 and port 4 separately. Furthermore, the number of coincidence is dependent on the amount of distinguishability. This phenomenon is called Hong-Ou-Mandel (HOM) interference [52], which is a useful tool in experimental quantum optics to check and ensure the indistinguishability between photons.

We, therefore, first measured the HOM interference to find the appropriate path delay (or equivalently, the appropriate time delay) to ensure the temporal indistinguishability. The exact setup for this measurement is shown in Figure 3-8, which is slightly different from the setup presented in Figure 3-1. By adjusting PC1 in Figure 3-8 such that the signal and idler polarizations are equal at the inputs to the fiber NPBS, we measured the HOM interference at a pump power of 25 μW with negligible multi-pair generation probability within the coincidence window [51]. Figure 3-9

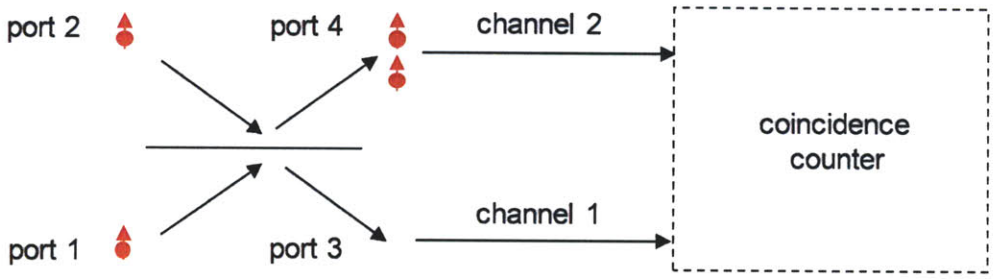

Figure 3-6: Schematic of Hong-Ou-Mandel interference without distinguishability. If two photons are sent into the two input ports of a 50-50 beam splitter and if these two photons are truly indistinguishable, they always come out from the same output port, either 3 or 4, but not simultaneously from both. Thus, there is no coincidence. This situation corresponds to the dip in Figure 3-9.

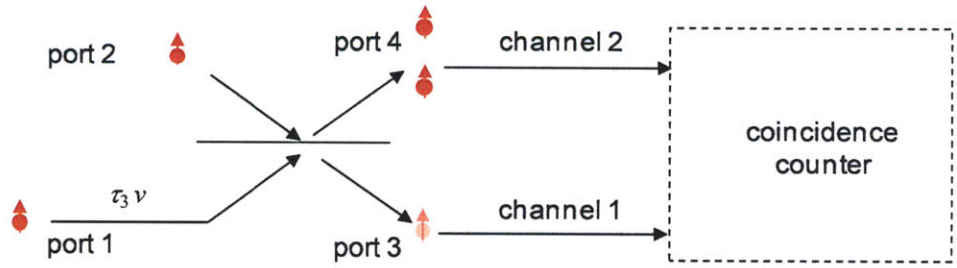

Figure 3-7: Schematic of Hong-Ou-Mandel interference with distinguishability. If there is some distinguishability between two photons (here as a time difference, τ_3), there will be coincidence. The speed of light is denoted as v.

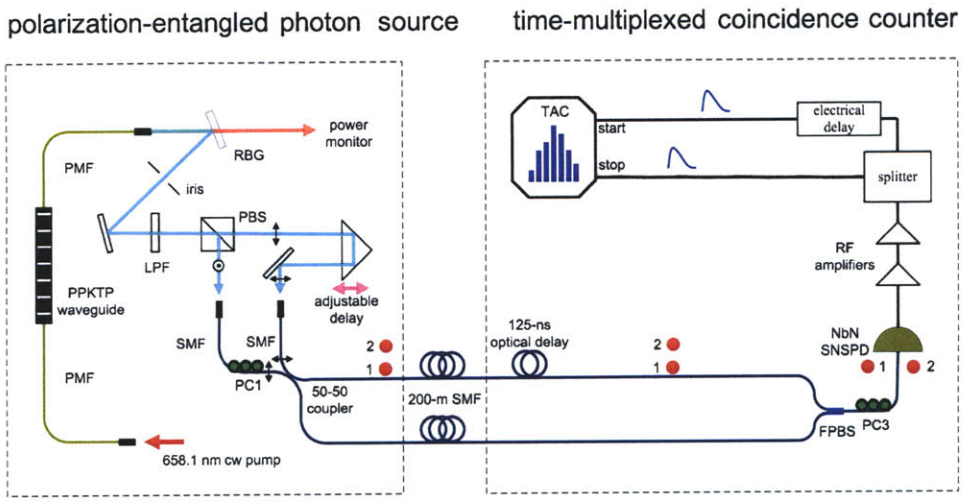

Figure 3-8: Experimental setup of Hong-Ou-Mandel interference. This figure should be read in comparison with Figure 3-1. The major differences include: (1) the polarization of the two photons are adjusted to be the same before the combination and interference at the 50-50 beam splitter; (2) On the detector side, there is no polarization analyzing module (i.e., HWP, PBS in Figure 3-1). PC3 was used in front of the NbN SNSPD to adjust the polarization of the photons to maximize the counts. The adjustable delay was used to compensate the time difference between two photons to ensure temporal indistinguishability.

shows the measurement results, taken without subtraction of accidental coincidences. The results yield an HOM visibility $V = (C_{\max} - C_{\min})/(C_{\max} + C_{\min}) = 99.2\% \pm 0.1\%$, where $C_{\max}$ ($C_{\min}$) is the maximum (minimum) coincidence count. To the best of our knowledge, this result is the highest HOM visibility reported for waveguide-based photon-pair sources. Compared with the previous measurements using gated InGaAs detectors [39], the coincidence rate per unit power has been improved by a factor of 150 due mostly to the use of the high-efficiency SNSPD in free-running mode. More importantly, the combination of low fluorescence from the waveguide source and low dark counts of the SNSPD significantly reduced accidental coincidences to 0.3% of $C_{\max}$, thus enabling more accurate measurements of the two-photon coherence properties without accidentals subtraction.

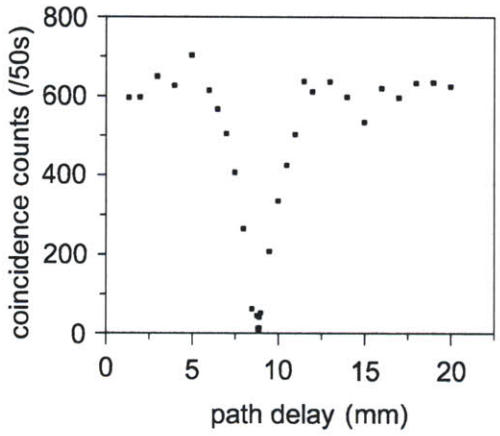

Figure 3-9: Measured Hong-Ou-Mandel interference. The x-axis is the adjustable path delay, and the y-axis shows the coincidence counts in 50 seconds for each data point. The data shown here are raw data without any accidentals subtracted.

3.3 Characterization of entanglement distribution

For polarization-entanglement generation, the time delay of the signal arm (the adjustable delay in Figure 3-1) was set at the minimum of the HOM dip to ensure that there was no timing distinguishability between the signals and the idlers. We characterized the quality of polarization-entanglement distribution by measuring the two-photon quantum interference remotely at the detector location. The measured interference is shown in Figure 3-10 for a pump power of 25 μW in the waveguide. The measured entangled-photon coincidence flux was 5.8 pairs/s. Without accidentals subtracted, we obtained a two-photon quantum-interference visibility of $98.2\% \pm 0.3\%$ in the H-V basis (HWP1 was set to be $0\,^\circ$) and $97.2\% \pm 0.1\%$ in the antidiagonal-diagonal (A-D) basis (HWP1 was set to be $22.5\,^\circ$). We also performed the polarization analysis at the source location before fiber distribution, and obtained a two-photon interference visibility of $98.3\% \pm 0.0\%$ in the H-V basis and $97.2\% \pm 0.3\%$ in the A-D basis, suggesting that entanglement distribution over a short length of 200-m fiber showed no degradation.

The visibility, V, is a function of the pair rate generated, which is further de-

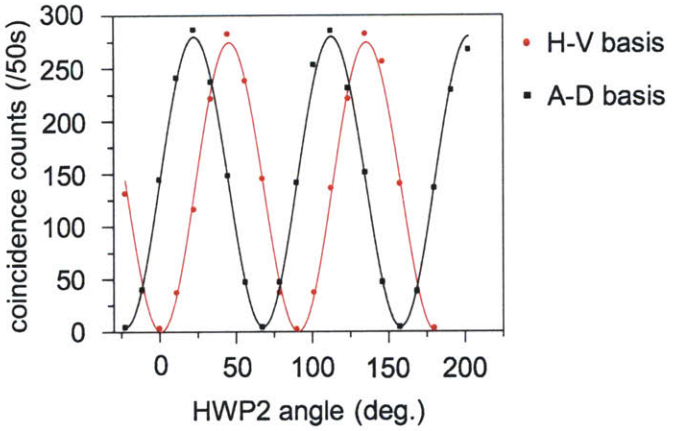

Figure 3-10: Measured two-photon quantum-interference after entanglement distribution. Half wave plate (HWP) 2 was rotated and coincidences in 50 seconds for H-V basis (HWP1 was set to be 0°) and A-D basis (HWP1 was set to be 22.5°) was measured. The dots are measured data without subtraction of accidentals and the curves are least-square fitting using sinusoidal functions.

pendent on the pump power inside the nonlinear crystal waveguide. Increasing the pump power increases the pair rate, but decreases the visibility. We define a dimensionless mean pair rate, α, as brightness $\times$ (coincidence window) $\times$ (pump power inside the waveguide), in which the brightness of the entangled-photon source used in this experiment was 2×10^7/s/mW [39], and the coincidence window used was 1 ns.[2] The dependence of V on α follows the following relation [11]: $V = 1 - 2\alpha$, assuming small pump power and ideal visibility at very small pump power (i.e, when the pump power approaches 0). The decrease of the visibility with the increase of α is due to multipair events. We measured the visibility with accidentals subtracted at different α for both H-V and A-D bases, and plotted the measured data in Figure 3-11. Each data point is the average of three measurements, and the error bar on each data point represents the standard deviation. The data sets for both H-V and A-D bases were fitted by $V = V_0 - 2\alpha$ with V_0 as a fitting parameter.

Given the use of single-mode fibers and a narrowband spectral filter, we would

[2]For example, in the case with 25-μW pump power, the pump power inside the waveguide was 12.5 μW. α in this case is calculated to be 0.025%.

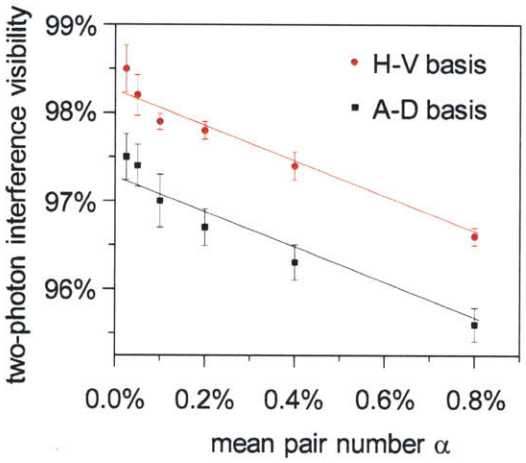

Figure 3-11: Measured visibilities as the function of the mean pair number, α. The linear decrease of the visibility with the increase of α is due to multipair events.

expect a visibility much closer to unity at very small α. We identified two main sources of degradation: (1) the 0.3% residual accidental coincidences that decreased the visibility by 0.6% and (2) a 1% visibility degradation due to observed signal and idler channel cross-talk that was caused by insufficient polarization extinction (25 dB) in the PM fiber and by alignment tolerance of the PM fiber axis relative to that of the PPKTP crystal.

Polarization entanglement may decohere over time in propagating through the fiber network caused by depolarization mechanisms such as temperature fluctuations and mechanical vibration. To investigate the stability of the distributed entanglement quality, we repeatedly measured the two-photon quantum-interference visibility in both H-V and A-D bases over a duration of 150 minutes. The results are shown in Figure 3-12, in which the time origin refers to the point when any depolarization over the network was corrected and the system was left unattended thereafter. We found that a visibility greater than 97% could be maintained for ~30 minutes without active polarization control, suggesting that short-distance distribution of polarization entanglement over an unattended fiber network is feasible.

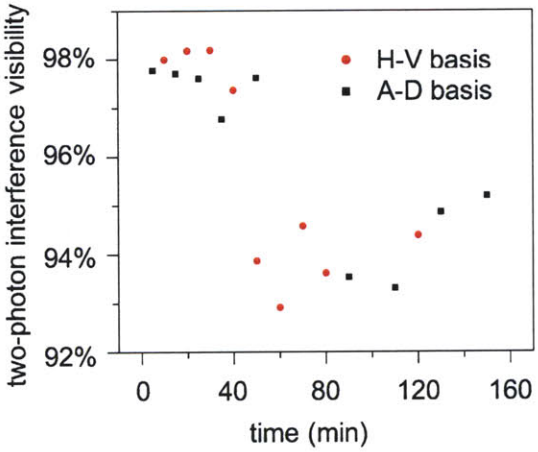

Figure 3-12: Repeated measurement of two photon interference visibility over 150 minutes.

3.4 Summary

This chapter presented a demonstration of polarization-entanglement distribution over a short-length standard telecom fiber-optic network. Polarization entanglement was generated by a fiber-coupled, low-noise PPKTP waveguide source and detected by a single high-efficiency, low-dark-count-rate SNSPD using time-multiplexed coincidence detection. This single SNSPD improved the pair rate in HOM interference by a factor of 150. At the pump power of 25 μW in the waveguide, we obtained a two-photon quantum-interference visibility of over 97% without subtraction of accidental coincidences after distribution. The visibility was found to be stable for ~30 minutes. This experiment is a demonstration of the impact, in the field of quantum optics, of the SNSPD system presented in Chapter 2.

The system of polarization-entanglement distribution may find applications in short-distance, short-time-scale fiber-optic distribution of high-quality polarization entanglement, for instance, in networking between a photonic and an atomic entanglement quantum system. Moreover, our work also suggests that fiber-optic distribution of polarization-entangled photons over longer distances should be possible with active polarization controls.

Chapter 4

Superconducting-nanowire single-photon detector integrated with optical nano-antennae

Chapters 2 and 3 have presented an SNSPD system with a large-area detector and the application of this system in polarization-entanglement distribution. The large active area allows photons to be efficiently coupled into the detector; however, increasing the active area of the detector decreased its speed. The speed of an SNSPD is considered to be one of the major advantages over other types of infrared single-photon detectors. It is desirable to realize an SNSPD that simultaneously has a practical active area, fast operating speed, and high device efficiency. Realizing such a device relies upon photonic design of the device structure. The idea is to use photonic structures to enhance the absorption of a short nanowire that has a small kinetic inductance. This chapter presents the design, fabrication, and characterization of SNSPDs integrated with optical nano-antennae that have achieved this goal.

In recent years, there has been tremendous interest in using nano-metallic structures to enhance the performance of active optoelectronic components. For example, a bow-tie antenna has been integrated on the facet of a laser diode to intensify the light at the nanoscale [53]. In addition, a dipole antenna has been integrated with a germanium photodiode to enhance the photocurrent [54]. In quantum optics, silver

nanowire has been used to enhance the non-classical light emission from a single quantum dot [55]. SNSPDs have been used to detect surface-plasmon polaritons in the near field [56]. Here, we integrate an SNSPD with optical nano-antennae to enhance its performance at detecting single photons from the far field.

Nano-metallic structures have different emphases on applications at infrared and visible wavelengths. The infrared spectral range, compared with the visible, is further away from the plasma resonance frequency of metals so that a surface-plasmon polariton in the infrared spectral regime is more like a photon than a plasmon. The capability of metal to decrease the wavelength of the surface wave at infrared wavelengths is weak; however, the metal is much less lossy in the infrared. Thus, metal nanostructures are suitable for applications in the infrared where efficiency is the most important concern, for example, photodetectors [54], and applications in the visible where a small spatial mode is the most important concern, for example, nanolithography [57].

This chapter is structured as follows. In Section 4.1, I present the concept and design of SNSPDs integrated with optical nano-antennae. In Section 4.2, I explain the fabrication and imaging of the device. In Section 4.3, I show the device characterization, including the measurement of the device efficiency, the kinetic inductance, and the timing jitter. In Section 4.4, I compare the performance of the antenna-integrated SNSPD with the performance of previously reported devices. In Section 4.5, I discuss the possibility to apply this device structure to narrower nanowires (width $\leq$ 30 nm) to detect single photons at the wavelength of 3 μm - 5 μm. In Section 4.6, I summarize this chapter. Most of the work presented in this chapter has already been documented in [10, 58, 59, 60].

4.1 Concept and device design

In order to make the detector simultaneously fast and efficient, one needs to use a short nanowire that can absorb incident photons effectively, probably assisted by additional photonic structures. Suppose we want to cover a practical active area, for

instance, 9 μm by 9 μm, with a NbN nanowire meander. We can either use a dense meander as shown in Figure 4-1 (a) or use a sparse meander as shown in Figure 4-1 (b). The length of the nanowire in the dense meander with a small pitch is long, and therefore, the detector is slow because of the large kinetic inductance. In contrast, the length of the nanowire in the sparse meander with a large pitch is short, and therefore, the detector is fast because of the small kinetic inductance. However, the nanowire in a large pitch meander cannot absorb incident photons efficiently because most of the incident photons simply pass through the gaps.

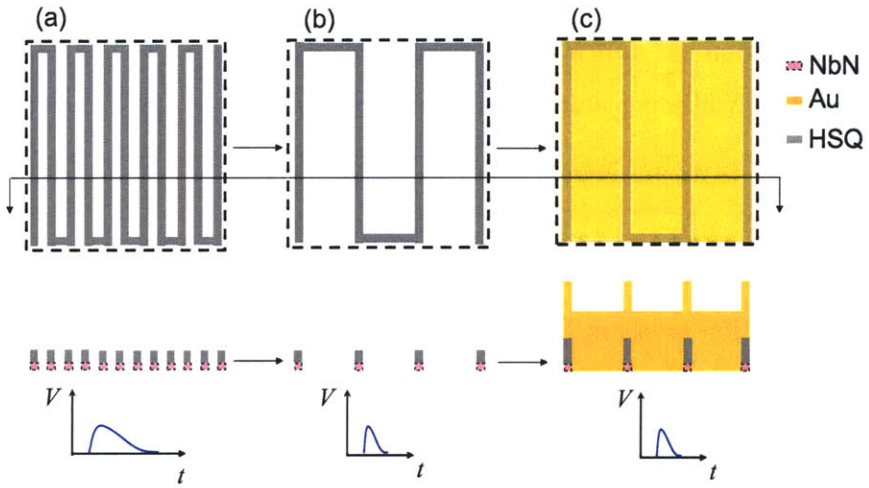

Figure 4-1: Explanation of the concept development of the superconducting-nanowire single-photon detector integrated with optical nano-antennae. The upper panel shows the schematic of the device structure from a top view. The middle panel shows the cross section. The lower panel shows the schematics of the output. In order to cover an area with NbN nanowire meander, dense meander in (a) or sparse meander in (b) can be used. The nanowire in (a) is long, so that the detector is slow; the nanowire in (b) is short, so that the detector is fast. However, the large gaps between adjacent nanowires in (b) allow incident photons to pass through the gaps, so that the absorption is weak. As shown in (c), the idea is to put gold between the adjacent HSQ structures and on top of the HSQ to block the path of the transmission and reduce the reflection.

A schematic of the device structure with integration of optical nano-antennae is shown in Figure 4-1 (c). Our idea is to add metal, for example, gold or silver, between adjacent NbN and HSQ, and on top of HSQ. The physical intuitive picture was to block the path for transmission and reduce the reflection by interference for

TM-polarized light. Our optical simulation confirmed this intuition. We found that this device structure is better than the existing device structures as far as efficiency and speed are concerned. Here, three effects play roles in absorption enhancement of such a narrow nanowire. They are (1) non-resonant collection effect by a nano-slit, (2) resonant cavity effect, and (3) frequency-selective-surface effect. These three effects are not completely separable, and a complete explanation requires solving Maxwell's Equations numerically. The following explanations are thus somewhat phenomenological.

To quantify the enhancement of absorption, we define absorption enhancement as the ratio of absorption per unit width in the nanowire normalized to the absorption of an unpatterned NbN film per unit width. Intuitively speaking, this defined parameter describes the capability of added photonic structures to enhance the absorbed energy density inside NbN.

The first effect, the non-resonant nano-optical collection, is based on the fact that the effective collection area for TM-polarized light is larger than the geometric area of the slit. In other words, the subwavelength slit can collect and focus the light into the nano-slit [61, 62, 63], acting like a feed gap. Here, we use this effect to collect the light and focus onto NbN, and enhance the absorption of NbN. We simulated a similar one-dimensional gold structure with NbN at its aperture as shown in the inset of Figure 4-2 and found that the gold structure enhances the absorption of the NbN nanowire. Figure 4-2 presents this absorption enhancement. The absorption enhancement of an 80-nm-wide (the value of the nanowire width in our experiment) NbN nanowire is approximately 2, and approaches 1 for an infinitely wide slit. The absorption enhancement decreases almost monotonically with increasing slot width. This almost monotonic decrease, together with the strongly enhanced electric field observed in the simulation at the gold edge adjacent to the NbN, suggests the existence of non-resonant edge-scattering effects in this system.

In the second effect, the resonant enhancement of absorption by an optical nano-cavity backing the slit, the effective interaction time between the photon and the nanowire is increased due to cavity resonance. As shown in the inset of Figure 4-

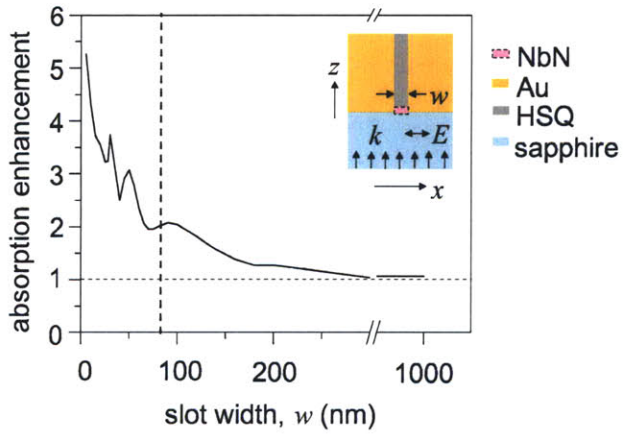

Figure 4-2: Study of non-resonant nano-optical collection effect. The figure shows the absorption enhancement as a function of slot width, w. The cross section of the model studied is shown in the inset. The model consists of a gold-HSQ-gold slot waveguide on top of a sapphire substrate and NbN nanowire is at the aperture of the waveguide. The experimental value of the slot width is 80 nm. The monotonic decrease, except for a few fine features, of the absorption enhancement with the increase of the slot width suggests that this effect is an edge effect.

3, each metal-insulator-metal slot behaves as a resonant optical waveguide, while a reflector behind the waveguide forms a quarter-wavelength cavity, eliminating optical transmission and reducing reflection. The photons are thus strongly absorbed by the nanowire placed at the waveguide aperture, where the electric field is maximal, i.e., at the field anti-node created by the quarter-wave resonator. By performing optical simulation on a single cavity, we optimized the cavity length, l, defined as the vertical distance from the top of the HSQ to the sapphire-NbN interface. Figure 4-3 presents the absorption enhancement of the NbN nanowire as a function of l. The width of the nanowire was fixed at 80 nm. The absorptance peaks at 150-nm cavity length and decreases at either shorter or longer cavity lengths around 150 nm. At this optimum cavity length, the absorption enhancement is increased by the cavity from $\sim$2 to $\sim$6. The slow decrease in absorptance for cavity length either shorter or longer than the optimum permits a wide tolerance of cavity length inaccuracy in fabrication.

The third effect, the frequency selective surface, is the result of interference among

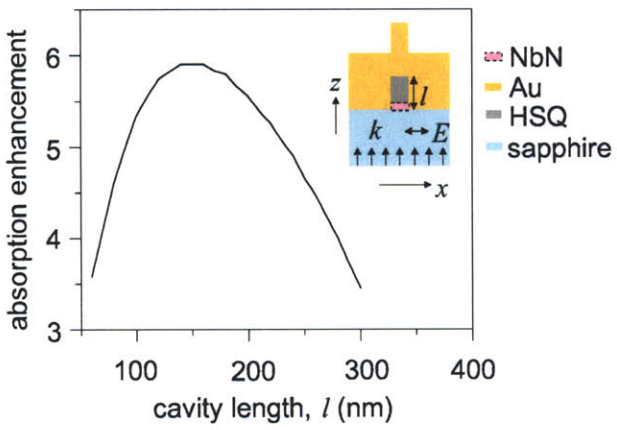

Figure 4-3: Simulated absorption enhancement as a function of cavity length, l. The model studied is shown in the inset. The absorption enhancement peaks at l~150 nm, and, correspondingly, the absorption enhancement, including the non-resonant collection effect, reaches 6.

the unit cells due to the periodic-like structure of the device, as shown in Figure 4-4 (a). Figure 4-4 (b) presents the simulated absorption enhancement and absolute absorptance, defined as the absorbed optical power normalized to incident optical power, as a function of pitch, p, fixing the w and l to be the experimental values 80 nm and 180 nm, respectively. This simulation includes the first and second effects mentioned above as well. At small pitches, the absorption enhancement is suppressed because the antenna aperture of each unit cell overlaps that of adjacent cells. By increasing the pitch, more light is concentrated into each slot and absorbed by the NbN nanowire. The absorption enhancement would saturate at large pitch if each individual antenna did not interfere with the others. However, when the pitch of the NbN nanowire is equal to integer numbers of λ/n, where n is the optical index of sapphire, most of the incident light is reflected by the gold instead of being coupled to the optical nano-cavities and NbN nanowire; therefore, the absorption of the NbN is minimized. The interface between sapphire and nano-structured gold thus behaves as a frequency selective surface [64]. The initial increase of absorption enhancement with pitch and the minimum at $p = 886$ nm result in a peak of absorption

enhancement at the pitch of ~600 nm, which was therefore chosen for our experiment. Correspondingly, the maximum absorption enhancement is 8, ~25% of which is due to this frequency-selective-surface effect. In addition, Figure 4-4 (b) presents the absolute absorptance as a function of p. For 600-nm pitch, the absolute absorptance is calculated to be 47% for TM-polarized light.

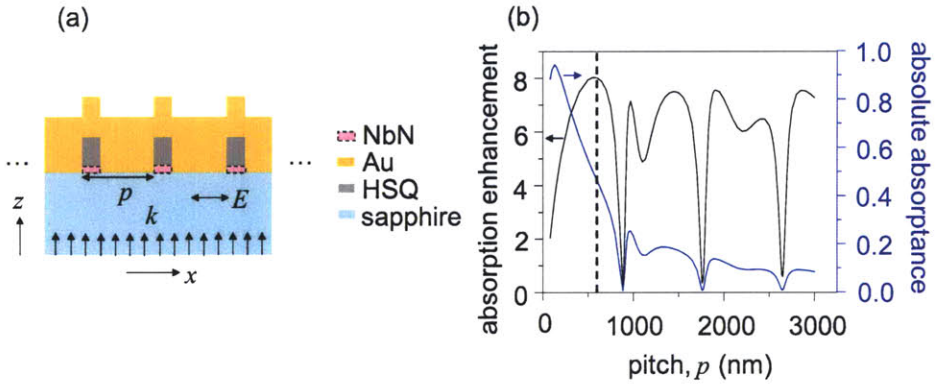

Figure 4-4: Study of the frequency-selective-surface effect. (a) shows the model used in this study. It is an infinite periodic structure with the unit cell shown in the inset of Figure 4-3. The pitch of the structure is denoted as p. (b) shows absorption enhancement and absolute absorption as a function of pitch p. The inference pattern is due to the nanostructured interface between gold and sapphire, which forms the frequency-selective surface. The interference makes the total absorption enhancement including three effects peak at the pitch 600 nm. The maximum absorption enhancement is ~8 and the corresponding absolute absorption is ~50%.

The optical simulations in this section were done by using the commercial Comsol Multiphysics software and were based on the finite-element method. The optical indices for NbN [10], $NbNO_x$ [10], gold [65], HSQ [10], and sapphire [10] that we used in simulations were $5.23+5.82i$, 2.28, $0.55+11.5i$, 1.39, and 1.75, respectively, where $i=\sqrt{-1}$. The thickness of the NbN is 4.5 nm. The exterior boundary conditions for the horizontal boundaries that we used were always scattering boundary conditions. For the vertical boundaries, we used scattering boundary conditions when simulating a single slot and periodic boundary conditions when simulating the meander. When simulating a single slot, the width of the sapphire used in the simulation was 20 μm.

Figure 4-5 presents the intensity distribution and the time-averaged Poynting vector assuming $d = 180$ nm, $w = 80$ nm, and $p = 600$ nm. The collection effect of

the optical nano-antennae is clearly seen, and the NbN is positioned near the field maximum.

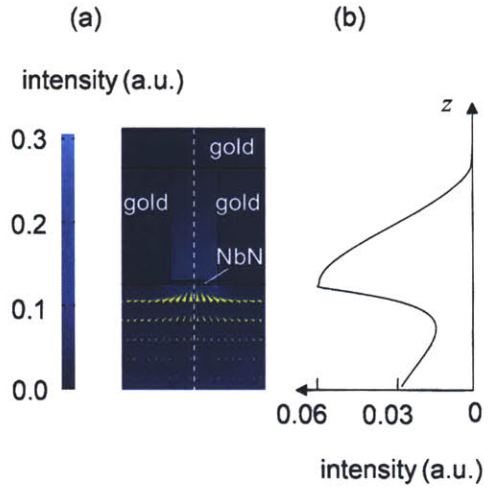

Figure 4-5: Simulated intensity distribution and time-averaged Poynting vectors. In (a), the surface color represents the field intensity and the arrows show the time-average Poynting vectors. The capability of collecting and focusing the incident light by the optical nano-antennae can be seen. In (b), the line shows the intensity distribution along the white dashed line in (a), illustrating that the NbN nanowire is positioned near the field maximum.

4.2 Device fabrication and imaging

We successfully fabricated the SNSPDs integrated with optical nano-antennae. Compared with the process used for fabricating SNSPDs with a quarter-wavelength cavity, the process used here has two major differences: (1) we used direct e-beam writing on 300-nm thick HSQ to define the nanowire; (2) we did e-beam writing only once in the whole process to fabricate a chip. The process is described in details as follows.

Starting from a 4.5-nm thick NbN film on sapphire substrate, we first fabricated gold contact pads. To do this, we spun on ~1-μm of Shipley Microposit S1813, a positive-tone photoresist, baked the chip in ambient conditions at 90 °C for 3 min, performed contact optical lithography to define the pads, and developed the resist. After evaporating 10-nm titanium (Ti) and 50-nm gold (Au), we performed liftoff in

90 °C NMP solvent (1-methyl-2-pyrrolidinone). The Ti layer was used to enhance the adhesion between Au and NbN. We then spun on ~300-nm HSQ formulated as Fox-14 from Dow Corning, and performed scanning-electron-beam lithography at 30 kV to define the nanowire meander structure, followed by developing the HSQ in 25% tetramethylammonium hydroxide (TMAH) for 4 min at ~20 °C. We used RIE to transfer the pattern into NbN from HSQ with CF_4 as the reactive gas and RF power of 98 W (power density: ~1.5 Wcm^{-2}) for 100 sec. The resulting thicknesses of HSQ measured by both atomic force microscopy and scanning-electron-beam cross-section imaging were 180 ± 10 nm. To integrate the nanowire detector with the optical nano-antennae, we then spun on ~1-μm S1813 a second time, performed contact optical lithography aligned with the detector to open a window of 25 μm by 25 μm for the gold antenna structure. After evaporating ~6-nm SiO_2 for electrically insulating the nanowire from the Ti and Au, followed by ~3-nm Ti, and ~300-nm Au, we did liftoff in 90 °C N-methyl-2-pyrrolidone. The resulting optical nano-antenna-ntegrated SNSPD is shown in Figure 4-6.

A sample detector was cut by focused ion beam and imaged by electron beam using a Zeiss NVision 40 dual beam system. We first deposited ~2-μm thick platinum (Pt) *in-situ* in a 2 μm × 10 μm area, within which the cross-section would be, to protect the device structure from being damaged by the focused gallium ions. The cut was done sequentially by a coarse mill (30 kV, 700 pA), a medium mill (30 kV, 300 pA), and a final fine polish (30 kV, 40 pA). The cross-section was then imaged by electron beam at 2 kV using the secondary-electron detector. Although the chip was tilted so that the angle between the normal to the chip and the incident electron beam was 54 °, the image in Figure 4-6 is shown after digital angle-correction.

If we compare the fabricated structure in Figure 4-6 (b) with the schematic in Figure 4-4, we find that they are slightly different. Voids not filled with gold near HSQ appear on the micrograph of the fabricated devices. These voids appear because of the shadowing effect in gold evaporation. As shown in Figure 4-7 (a), the gold on top of HSQ migrated during the evaporation process and the migrated gold shadowed the subsequent evaporation, yielding the voids.

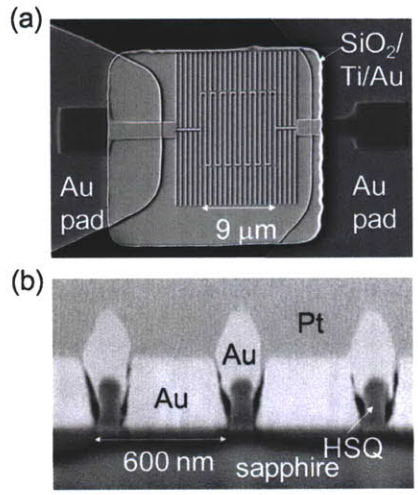

Figure 4-6: Scanning-electron micrograph of the fabricated superconducting-nanowire single-photon detector integrated with optical nano-antennae. (a) Top view. The active area of the detector is 9 μm by 9 μm. The surrounding linear structures are for proximity-effect correction in scanning-electron-beam lithography. (b) Cross-section view. This micrograph was obtained by an electron-ion dual-beam system. The sample was cut by focused ion beam and was then tilted and imaged by scanning electrons. The tilt was compensated digitally. The platinum was deposited *in situ* to protect the imaging area of interest from being damaged by the focused ion beam. The pitch of the meander is 600 nm. The NbN nanowire under HSQ is not visible on this micrograph because it is only ~4.5-nm thick.

We evaluated the effect of the voids on the absorptance of the nanowire by simulating the structure obtained in Figure 4-6 (b). We drew in Figure 4-7 (b) the geometry of a unit cell used in finite-element optical simulation. We found that the voids decreased the simulated absorptance from 47% to 44%.

To eliminate the voids, one could use a two-angle evaporation process or sputtering to coat the sidewalls of HSQ with gold. If the evaporation angles are sufficiently small and a slightly re-entrant resist profile is used around the edge of the metal-deposited region to avoid sidewall coating of metal on the resist, two-angle evaporation may be compatible with the subsequent lift-off required.

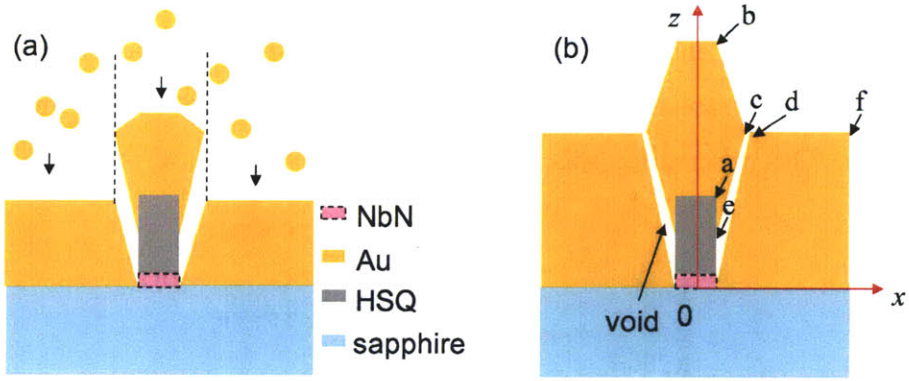

Figure 4-7: Cross-section schematic illustrating the appearance of voids and their effect on the absorption of the NbN nanowire. (a) These voids were attributed to migration of the gold on top of the HSQ during the evaporation process, which gradually shadowed the subsequent evaporation. (b) A geometry of a unit cell was used in finite-element optical simulation. A coordinate system was established to define the geometry. The x and z coordinates in nm for the points a, b, c, d, e, and f were (40, 186.5), (40, 486.5), (110, 300), (120, 300), (40, 90), and (300, 300), respectively.

4.3 Device characterization

We characterized the fabricated superconducting-nanowire single-photon detectors by measuring device efficiency, kinetic inductance, and timing jitter. From the measured kinetic inductance, we calculated the reset time.

4.3.1 Device efficiency

Device efficiency was measured at a baseplate temperature of 2.1 K using the setup similar to that in Figure 2-7, but in a cryogenic probe station instead of a cryocooler. In our experiment, the detector was illuminated by a pulsed laser at the wavelength of 1550 nm with a pulse repetition rate of 10 MHz. We used the polarization controller in the optical illumination path to control the polarization of the incident photons. We mounted a reference chip without antenna integration adjacent to this chip with antenna integration, and ensured that the orientations of the nanowires on both chips were same. Based on the fact that an SNSPD without antenna integration has maximum counting rate for TE polarization and minimum counting rate for TM

polarization, we identified TE and TM polarizations using an SNSPD on the reference chip. We then found that the SNSPDs integrated with optical nano-antennae had maximum counting rate for TM polarization and minimum counting rate for TE polarization. This observation was consistent with our theoretical prediction.

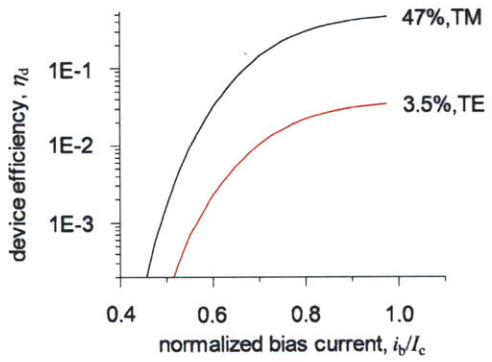

Figure 4-8: Measured device efficiency as a function of bias current normalized to the critical current, I_c (11.6 μA at 2.1 K). At the bias of 97.5% of the I_c, the device efficiency for TM polarization reaches 47% and for TE polarization reaches 3.5%. The dominant response to photons in TM mode is the key feature of the antenna effect.

Device efficiency for both polarizations as a function of bias current is presented in Figure 4-8. Once the detector was biased at 97.5% of I_c, which was 11.7 μA at the temperature of 2.1 K, device efficiency reached 47% ± 5% for TM polarization and 3.5% ± 0.4% for TE polarization. The fractional error in the detection efficiency measurement was estimated to be ~10%, primarily due to the calibration of the optical-spot diameter. For this device, we did not coat the back of the sapphire substrate with an anti-reflection coating (ARC) as done in prior work [2]; if we take the calculated 7.4% reflectance at the air-sapphire interface into account, the corrected device efficiencies for TM- and TE polarizations were 50% ± 5% and 3.8% ± 0.4%, respectively. The response of the detector to TE-polarized incident light is suppressed because the optical nano-cavities do not support TE-modes so that most of the incident TE-polarized light was reflected.

The 47% device efficiency for TM-polarized light would be surprising if one did not consider the effects described above, given that the fill-factor of NbN nanowire was

only ~13%. Furthermore given that the intrinsic quantum efficiency, P_r, is estimated to be ~70-90% [66], the majority of incident light was coupled into the NbN nanowire, i.e., the absorptance of the NbN nanowire must be > 50% for TM polarization. As a comparison, the absorptance of the 80-nm wide NbN nanowire in the 600-nm pitch meander on the sapphire substrate without any optical nano-antenna integration was simulated to be 4% and 8% for TM and TE polarizations, respectively. This difference in absorptance between the SNSPDs with and without antenna-integration demonstrates the effect of the optical nano-antennae.

To further support the thesis that the optical nano-antennae play an important role in device performance, we calculated polarization ratios, defined as device efficiency of TM polarization relative to TE polarization at the same bias current, 97.5% of I_c. The calculated ratio from the measured device efficiencies was ~13 for this antenna-integrated device, as opposed to ~0.5 for a 600-nm pitch detector without antenna-integration.

The presented results focused on a single device out of 45 devices that were fabricated. Figure 4-9 presents maximum efficiency (TM polarization) and minimum efficiency (TE polarization) for the 4 of these 45 devices that showed maximum efficiency exceeding 10%. The ratio of device efficiency for TM- and TE polarizations is a key signature of the antenna effect, and this effect was observed in all four of the devices.

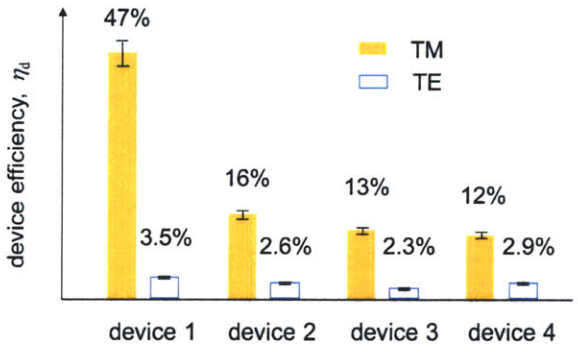

Figure 4-9: Histogram of device efficiency of the detectors with maximum device effiecny larger than 10% on the chip. The dominant response to photons in the TM mode is the key feature of the antenna effect.

Two challenges in the fabrication process limited the yield; understanding these challenges should permit further improvement in device yield and performance. The first challenge was direct electron-beam writing on thick HSQ resist. The resist used in this experiment was 300-nm thick, as opposed to the 70-nm thickness typically used [2]. Thicker resists scatter electrons over a greater area, and, therefore, the dose control required to yield uniform nanowires was more difficult for these devices. To reduce the scattering of electrons in thick HSQ in future work, one could, for example, increase the acceleration voltage from 30 kV to 100 kV. The second fabrication challenge was gold evaporation. During the cryogenic testing, we observed that some devices with similar critical currents differed significantly in device efficiency, suggesting that the absorptance was different among devices. This difference might be due to variation in the migration of gold during the evaporation process, which caused voids of varying shapes.

4.3.2 Kinetic inductance

To evaluate the speed of the detector, we measured the kinetic inductance, L_{k}, of the detector to be $\sim$100 nH using a network analyzer. The recovery of the bias current, and therefore the detection efficiency, is known to be limited by this kinetic inductance [5]. From the measured curve of device efficiency vs. bias current in Figure 4-8, we calculated the bias current corresponding to 90% of the device efficiency when the detector was biased at 97.5% of its I_{c}. From this identified bias current and the expected exponential recovery with time constant $L_{\mathrm{k}}/(50\ \Omega)$ of the bias current after returning to the superconducting state, we calculated the reset time to be $\sim$5 ns. Details of the calculation appear in Appendix B.

4.3.3 Timing jitter

Because the origin of timing jitter of the SNSPDs is not well-understood, and because low timing jitter is one of the advantages of this technology, one concern we had was whether adding the optical nano-antenna structure to the superconducting nanowire

would significantly affect the timing jitter of the detector. To address this concern, we measured timing jitter for TM and TE polarizations to be 39 ± 3 ps and 45 ± 3 ps, respectively, biasing the detector at 97.5% of its I_c.

We measured the timing jitter of the SNSPD integrated with optical nano-antennae using the same method and experimental setup used in [6]. The output pulses from a passively mode-locked fiber laser with a pulse repetition rate of 10 MHz and a pulse width of less than 1 ps were split into two channels by an optical splitter, and were sent to the SNSPD and a reference photodiode with 40 GHz bandwidth. Their outputs were sent to two channels of a 6 GHz real-time oscilloscope. The front edge of the output of the SNSPD was used as the trigger, and the timing of the output of the photodiode was measured.

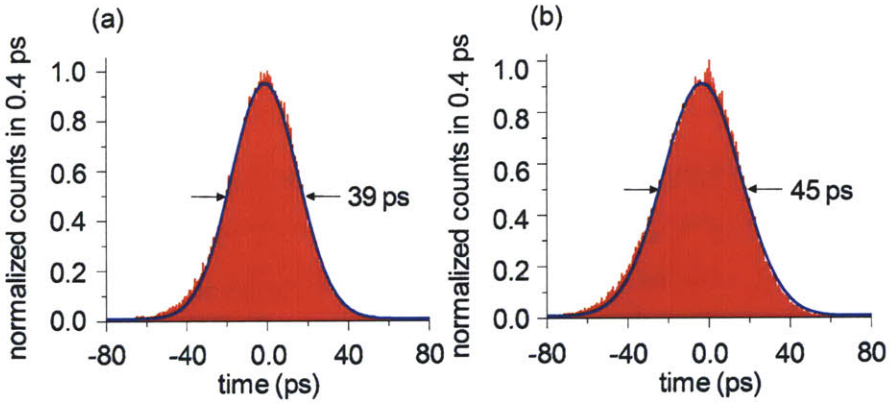

Figure 4-10: Histogram of timing jitter of the superconducting nanowire single-photon detector integrated optical nano-antennae for (a) TM polarization and (b) TE polarization at the bias of 97.5% of the critical current of the nanowire. The lines are Gaussian fits, with full widths at half maxima of 39 ps and 45 ps for (a) TM and (b) TE polarizations, respectively.

The measured timing-jitter histograms and Gaussian fits are presented in Figure 4-10 (a) for TM polarization and (b) for TE polarization. The Gaussian function used for fitting is expressed as

$$g(t) = g_0 + \frac{a}{\sigma\sqrt{\pi/2}}\exp[-\frac{2(t-t_0)^2}{\sigma^2}], \tag{4.1}$$

where g_0, a, and σ are fitting parameters. The full width at half maximum equals 1.18σ; it is 39 ps for (a) TM polarization and 45 ps for (b) TE polarization. There was $\pm$ 3 ps uncertainty on each measured value because of the $\pm$ 2 ps uncertainty of trigger and interpolator jitter specified by the oscilloscope. The difference between the measured values of the timing jitters for two polarizations may represent a measurement uncertainty, or a real difference between the timing jitter for different polarizations. Further investigations of the timing jitter would be required to resolve this issue.

4.4 Comparison with previously reported devices

In order to comprehensively compare the device efficiency, speed, and active area of this detector with previously reported devices, we define a figure of merit as $\Sigma\eta/\tau$, where Σ is device area, η is device efficiency, and τ is reset time. Device efficiency of this detector was 47% $\pm$ 5%, with reset time of $\sim$5 ns and active area of 9 μm $\times$ 9 μm. The figure of merit of this detector is thus $\sim$7.6 μm^2/ns. As a comparison, the best previously published device efficiency for an SNSPD on sapphire [2] was 57% $\pm$ 6%, with reset time of $\sim$3.4 ns and active area of 3 μm $\times$ 3.3 μm. Its figure of merit is calculated to be $\sim$1.7 μm^2/ns. The large active area of this antenna-integrated SNSPD makes the coupling of light into the detector from fibers, waveguides, or free space much more efficient and convenient.

4.5 Integration of 30-nm wide nanowires with antennae

Mid-infrared (Mid-IR, 3 μm - 5 μm) photodetection is important in applications such as astronomy [67] and environmental monitoring [68]. The red-shift effect puts many nominally visible spectral lines into the IR and mid-IR spectral regions, and many vibrational and rotational resonances in complex molecules can be sensed and detected remotely. Although SNSPDs have wide spectral response, device efficiency

drops at longer wavelengths [3]. This drop in efficiency limits the mid-IR applications of the detector. As it has been experimentally observed that the drop of detection efficiency when decreasing the bias current was less for a narrower nanowire (20-30 nm wide) than for a wider nanowire (100 nm wide), according to the hotspot model, we expect that narrower nanowires are more sensitive to a photon with smaller energy than a wider nanowire. Therefore, it is natural to think of using narrow nanowires, with a width of $\leq$30 nm, to detect and sense mid-IR single photons.

However, several technical challenges associated with mid-IR SNSPDs made of ultra-narrow nanowire must be addressed. First of all, the diffraction-limited spot-size increases with wavelength. Thus, practical applications require a larger active area in order to couple the mid-IR radiation into the detector efficiently. Second, using a narrower nanowire to cover a larger active area with the typical fill-factor of 50%, we inevitably need to increase the length of the nanowire, resulting in a higher kinetic inductance and a slower speed. Note that the inductance per unit length of a narrower nanowire is larger than the inductance per unit length of a 100-nm nanowire. Finally, the absorption of NbN is weaker in the mid-IR spectral region than in the telecom spectral region.

We applied the idea of antenna integration to the ultra-narrow nanowire to address these challenges. To illustrate the principle, in our design and simulation we used the wavelength of 4 μm, a nanowire width of 30 nm, and a meander pitch of 100 nm, as an example. Because NbN and gold are dispersive at the wavelength of interest, we used the Drude model to fit the experimental data from 300 nm to 1700 nm that we measured by ellipsometry for NbN [1], and to fit the experimental data from the handbook [65] for gold. In this way, we can obtain their optical constants at any given wavelength of interest, and specifically at 4 μm, we obtained complex optical indices $9.01 + 9.61i$ for NbN and $3.18 + 28.48i$ for gold. For all the dielectrics, we assumed that they are non-dispersive, and optical constants at the wavelength of 1.55 μm were used [10]. We optimized the cavity length, l, in order to obtain resonance and maximize the absorptance of NbN. As shown in Figure 4-11,

[1]Details of the fitting appear in Appendix C

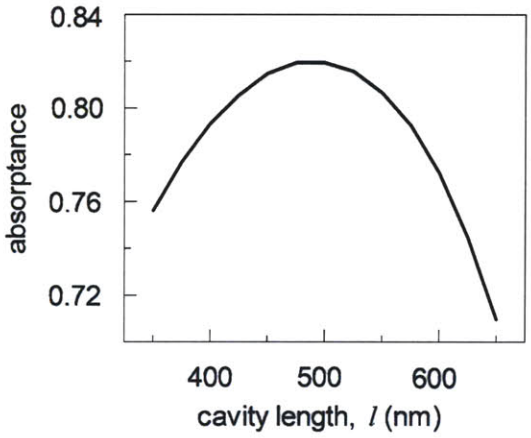

Figure 4-11: Simulation of the cavity effect for a 30-nm wide nanowire integrated with nano-antennae for detecting single-photons at the wavelength of 4 μm (See the device structure in Figure 4-1 (c). The optimum cavity length is ~500 nm and the corresponding absorption of the NbN nanowire is ~82%. The fact that it requires thick HSQ as the spacer layer is the major challenge in fabrication.

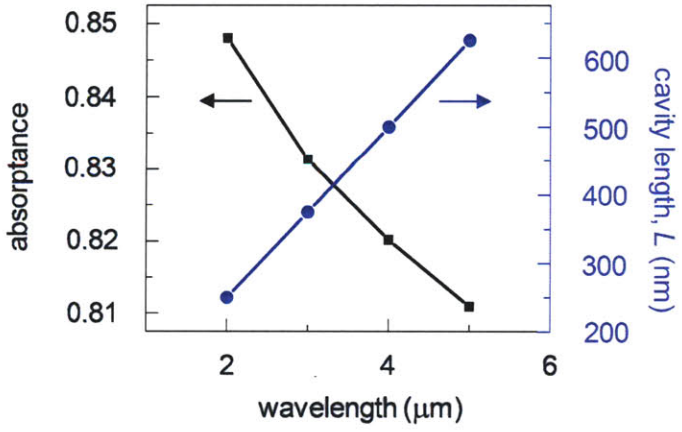

Figure 4-12: Simulated peak absorption and optimum cavity length as a function of wavelength.

the optimized cavity length is at ~500 nm, and remarkably, the peak absorptance is ~82% for TM-polarized incident light. Furthermore, this absorptance is not very sensitive to the actual cavity length. For instance, the absorptance is still ~76% when the cavity length is decreased to 350 nm. As a comparison, without nano-antennae and with only top reflector integration [2], the nanowire is more sensitive to TE polarization, and the optimized absorptance is 51%. The optimized cavity length and the corresponding absorptance for different wavelengths are shown in Figure 4-12. As expected, the optimized cavity length becomes larger for longer wavelengths. The slight drop in optimized absorption at longer wavelength is due to the fact that the frequency of the radiation is further away from the plasma frequency of NbN, and thus the material absorption becomes weaker.

We can increase the active area of the detector by increasing the pitch of the meander and sacrificing some absorption. Considering the wavelength of 4 μm again and increasing the pitch of the meander to 200 nm, for example, the absorptance decreases to 57%. However, increasing the pitch and doubling the detector area would make coupling more efficient. Note that while the pitch is being changed, the length and the width of the detector have not been changed. Therefore, the speed of the detector has not been affected.

To realize the structure that we designed, we increased the acceleration voltage to 100 kV (Elionix ELS-7000 SEBL facility at Harvard University) to directly write on 500-nm thick HSQ. Increasing the acceleration voltage decreases the forward scattering of the electrons in HSQ. Figure 4-13 and Figure 4-14 show a comparison of electron scattering between 30-kV and 100-kV cases, generated by Monte Carlo simulation. The simulation modeled electron scattering in a 500-nm thick, free-standing HSQ film. The electron beam expands more slowly due to less scattering at 100 kV than at 30 kV, and is therefore more suitable for fabricating narrow, high-aspect-ratio resist structures. The HSQ structure realized is shown in Figure 4-15. For such a slim structure with a high aspect ratio, it is necessary to use a critical-point dryer to dry the substrate after develop-ment. Otherwise, the HSQ will fall down due to the capillary force during the evaporation process of the residual liquid after devel-

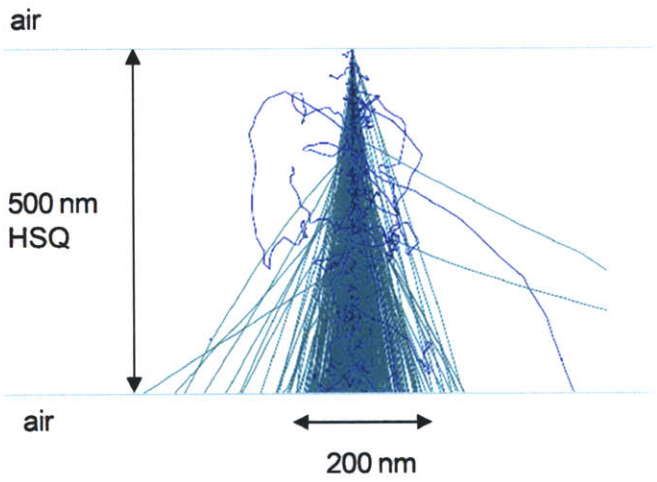

Figure 4-13: Monte Carlo simulation of electron forward scattering (green) and secondary electron scattering (blue) at an acceleration voltage of 30 kV inside 500-nm thick HSQ.

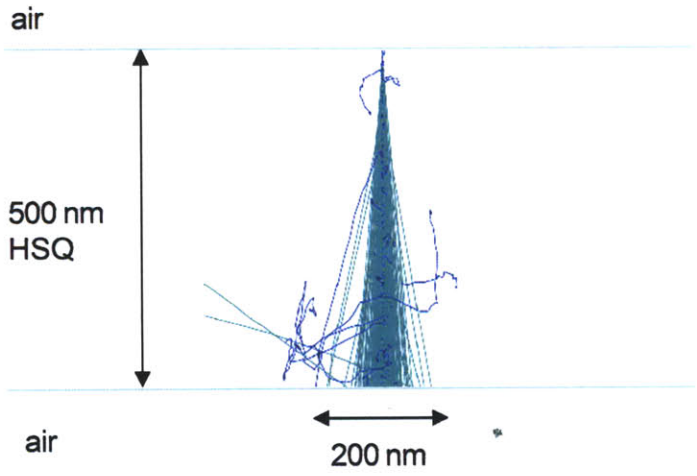

Figure 4-14: Monte Carlo simulation of electron forward scattering (green) and secondary electron scattering (blue) at an acceleration voltage of 100 kV inside 500-nm thick HSQ.

opment. From a fallen-down structure, we know that the thickness of the remaining HSQ was approximately 420 nm. The aspect ratio of the HSQ structure was therefore calculated to be 14:1. The following steps to complete the antenna integration include NbN etching using RIE, evaporation of SiO_2, Ti, and Au, and finally, liftoff.

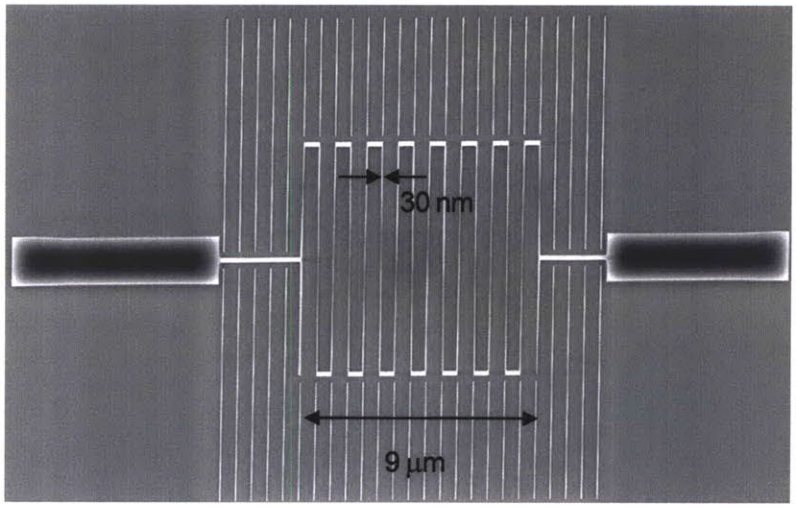

Figure 4-15: Experimentally realized 30-nm wide HSQ structure on an NbN-sapphire substrate using 500-nm thick HSQ and 100-kV acceleration voltage in scanning-electron-beam lithography. The meander with a pitch of 600 nm covers an area of 9 µm by 9 µm.

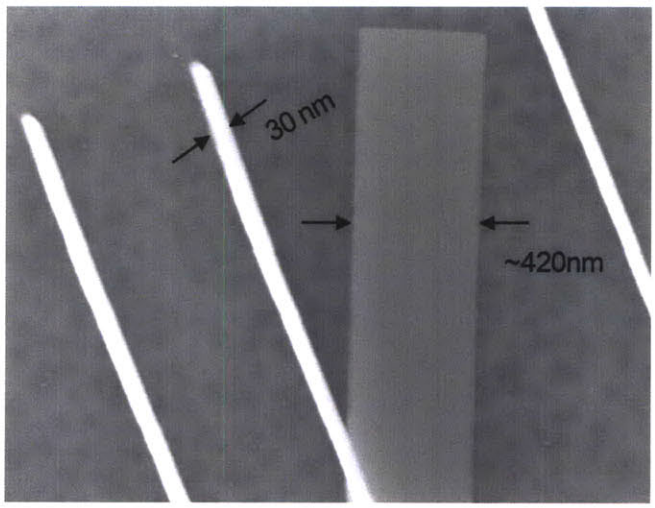

Figure 4-16: Scanning-electron micrograph of a fallen-down HSQ structure. From the fallen-down structure after development, the remaining thickness of the HSQ was measured to be ~420 nm.

4.6 Summary

The major result presented in this chapter is an SNSPD integrated with optical nano-antennae. This type of SNSPD is the only type that dominantly responds to TM

polarization. Furthermore, from the point of view of active area, speed, and device efficiency, this SNSPD has the record performance among single-element SNSPDs. To be more quantitative, the figure of merit is 4.5 times of the figure of merit of the SNSPD with the best device efficiency published in 2006 [2]. The active area, device efficiency, and reset time of this SNSPD are 9 μm by 9 μm, 47%, and 5 ns, respectively. This idea can be extended to ultra-narrow nanowires to sense and detect mid-IR single photons.

Chapter 5

Waveguide-integrated superconducting-nanowire single-photon detector

5.1 Introduction

The meander structure is effective for coupling light to an NbN nanowire; however, it is not the only effective structure. The meander is more suitable for free-space coupling; when the detector is coupled with fiber, it requires optical lenses and/or special mechanical designs and implementations, which are not easy to implement at a cryogenic temperature. Furthermore, the meander structure does not necessarily optimize the absorptance of NbN nanowire per unit length. This chapter introduces waveguide-integrated SNSPDs. This idea originated from an analogy of SNSPDs to classical optoelectronic components. Both classical laser diodes and photodetectors have two basic structures: (1) vertically coupled [69, 70] and (2) edge-coupled [71, 72]. An SNSPD in the meander structure is vertically coupled; a waveguide-integrated SNSPD is edge-coupled.

The design of the waveguide-integrated SNSPDs addresses two concerns: system detection efficiency and speed. The idea is to efficiently couple light into a nanowire

as short as possible [1], but not so short as to latch the device [33]. The simulation shows that it is possible to use a 50-μm long nanowire with waveguide integration to absorb most of the light coupled into the waveguide. The efficiency-speed product is thus extended. Furthermore, this structure makes SNSPDs compatible with various on-chip technologies that have been developed recently [73, 74, 75, 76, 77, 78, 79]. For example, an inverse-taper coupler [74] or a grating coupler [79] can enable efficient coupling of light from a single-mode fiber to the waveguide and eventually to the detector; ring resonators coupled with an integrated waveguide can behave as an optical filter, allowing the coupling of light only in a narrow spectral range to the detector [73]; such ring resonators can also serve as optical modulators and switches [77]. The concept and design of waveguide-integrated SNSPDs pave the way for on-chip applications of single-photon detectors and make integrated quantum optics possible. Most of the design work in this chapter has already been documented in [10].

5.2 Design

The waveguide-integrated SNSPD that we designed is shown schematically in Figure 5-1. The NbN nanowire on a sapphire substrate is no longer a meander structure as in a traditional SNSPD; instead, it is a straight nanowire wound only once in a hairpin configuration.[2] On top of the NbN nanowire, a Si_3N_4 waveguide is integrated with a SiON cladding layer. Furthermore, the beginning part of the waveguide is tapered in order to facilitate the coupling of light from a single-mode fiber [74]. Different from the traditional SNSPD, in which the light is coupled from the top or bottom (i.e., vertically coupled), here the light is coupled from the facet of the inverse-taper coupler (i.e., edge-coupled),[3] then adiabatically coupled to the waveguide with Si_3N_4 as the core, and eventually coupled into the NbN nanowire.

[1] An additional advantage of using a shorter nanowire is that compared with a longer nanowire, a shorter nanowire is with a smaller impedance mismatch with the 50-Ω transmission line.

[2] It can also be a nanowire wound multiple times; however, more NbN in the cross-section would further change the effective index, resulting in a larger impedance mismatch with the waveguide without NbN and therefore, more reflections.

[3] One can also couple light vertically to the waveguide and nanowire by integrating the waveguide with a vertical coupler.

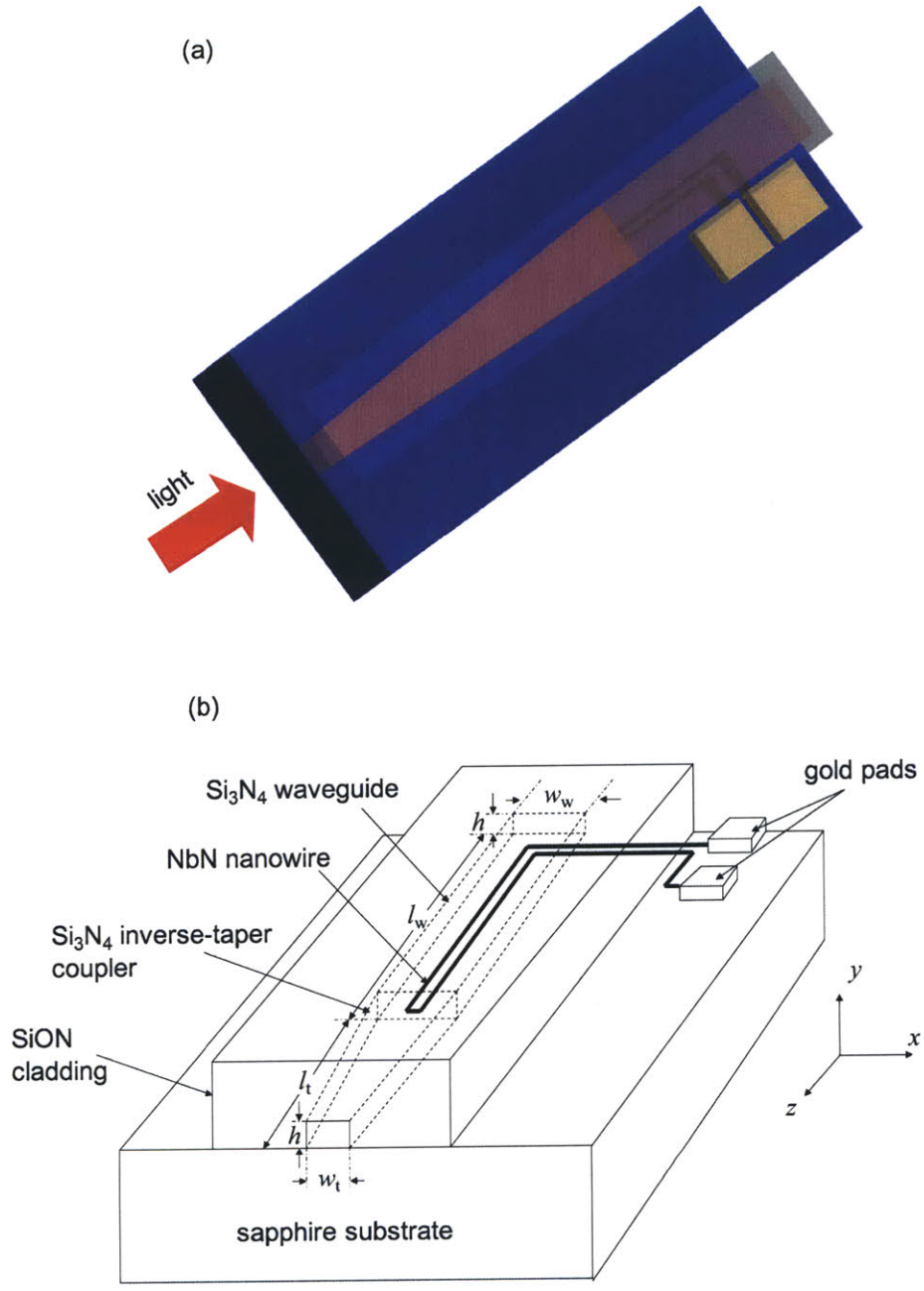

Figure 5-1: Schematics of waveguide-integrated superconducting-nanowire single-photon detector. (a) shows that the incident photons are coupled from the edge. (b) shows the components with labels. The core of the waveguide is Si_3N_4, sandwiched between a sapphire substrate and a SiON cladding layer. The NbN nanowire is under Si_3N_4 and on top of the sapphire substrate. The tapered part of the waveguide is for coupling light to the waveguide from a single-mode fiber or other waveguides.

Here, we use sapphire-Si_3N_4-SiON as the materials for the waveguides as an example to illustrate the concept and the design procedure. The concept and design procedure can also work for other choices of materials for waveguides, nanowires and substrates. For example, one can also use thermally oxidized silicon as the substrate (silicon dioxide is one cladding layer of the waveguide), deposited silicon as the core layer of the waveguide, and HSQ or deposited silicon dioxide as the second cladding layer. The NbN nanowire is on top of silicon dioxide. Other combinations of materials for the waveguide and the nanowire can also work under this concept and design procedure.

We designed the taper to minimize the coupling loss and the waveguide to maximize the absorption per unit length of the NbN nanowire in order to reduce its total length. In other words, the goal of the design is to maximize $\eta_c \times A$ and minimize the length of the nanowire. For illustrative purposes, we use 100-nm-wide NbN nanowires spaced with a 100-nm gap. The principle and procedure of the design can also be applied to other width and spacing, for example, the ultra-narrow nanowires. The thickness of the Si_3N_4 layer, h, for both the waveguide and the coupler is 300 nm. We found by simulation that the optimized $\eta_c \times A$ does not differ significantly for different thicknesses around 300 nm. The width of the coupler tip, w_t, can be designed to increase or reduce its mode size to match the mode from the fiber. The width of the waveguide is denoted as w_w, which can be designed to maximize the absorption of the NbN by controlling the size of the supported mode of the waveguide. The length of the taper, l_t, dependent on w_t and w_w, must be long enough to ensure that the coupling from the inverse taper to the waveguide is adiabatic. The length of the waveguide, l_w, is approximately half of the length of the nanowire, l_n, i.e., $l_n = 2l_w$.

We first consider the coupling of the light from the single-mode fiber with a 9.8 μm mode-field diameter (MFD) [4] to the inverse-taper coupler. Two modes exist in the inverse-taper coupler and the waveguide of interest, TE-like mode and TM-like mode. In TE-like mode, the dominant component of the electric field is E_x; in TM-like mode,

[4]The mode-field diameter is defined as the full width at $1/e^2$ of the intensity profile, or equivalently, full width at $1/e$ of the field profile, under the approximation discussed in Appendix D.

the dominant component of the electric field is E_y. The coupling efficiency, η_c, can be calculated by [80]

$$\eta_c = |M|^2 N/P, \tag{5.1}$$

where

$$N = [\int_{s\to\infty} (\vec{E}^*_{T,t} \times \vec{H}_{T,t}) \cdot z dS]/2, \tag{5.2}$$

$$P = [\int_{s\to\infty} (\vec{E}^*_{T,f} \times \vec{H}_{T,f}) \cdot z dS]/2, \tag{5.3}$$

$$M = [\int_{s\to\infty} (\vec{E}^*_{T,f} \times \vec{H}_{T,t}) \cdot z dS]/2N, \tag{5.4}$$

$\vec{E}_{T,t}$ and $\vec{H}_{T,t}$ are the transverse electric and magnetic fields of the mode of the coupler tip , respectively, $\vec{E}_{T,f}$ and $\vec{H}_{T,f}$ are the transverse electric and magnetic fields of the mode of the fiber, respectively,and dS is the differential cross-sectional-area element. Here, we use a linearly polarized mode with a Gaussian profile to approximate a mode of the fiber [5] and obtain the mode of the coupler tip via the finite-element method using Comsol Multiphysics^{TM}. In our simulation, we chose S as a 20-μm-by-20-μm square to ensure that the field outside this area is negligibly weak. The refractive indices used can be found in Table 5.1. In practice, the refractive indices for Si_3N_4 and SiON can be controlled by controlling the flow ratio and the pressure of the gases in the plasma-enhanced chemical vapor deposition (PECVD) process. The backreflection due to the index mismatch between the fiber and the inverse-taper coupler is estimated to be ~10%, and can be experimentally eliminated by adding a quarter-wavelength antireflection coating on the taper facet. Therefore, the coupling efficiency calculated above has not taken this backreflection into account.

The coupling loss as a function of the coupler-tip width, w_t, is plotted in Figure 5-2. As the width of the coupler tip increases, the mode size decreases. When the mode size of the coupler at its tip becomes similar to the mode size of the single-mode fiber, the coupling loss is minimized. One can see that this minimized loss for both TE- and TM-like polarizations is about 1.2 dB when the w_t is 450 nm for TE-like and

[5] More discussion of this approximation appears in Appendix D.

Table 5.1: Optical constants

Material	Refractive index at 1550 nm
NbN	$5.23 + 5.82i$
$NbNO_x$	2.28
Sapphire	1.75
Si_3N_4	1.98
SiON	1.75

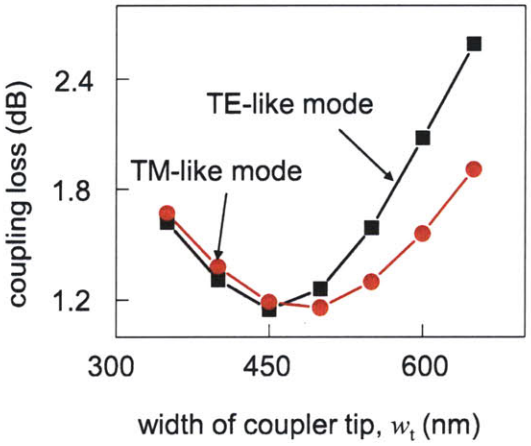

Figure 5-2: Simulated coupling loss between a single-mode fiber and the inverse-taper coupler as a function of the width of the coupler tip, for both TE and TM modes.

500 nm for TM-like. In this region, the coupling loss is quite insensitive to variations in width.

As mentioned above, the function of the inverse-taper coupler is to shrink the optical mode adiabatically, so that the light from the optical fiber with a large mode size can be coupled to the on-chip waveguide with a small mode size without adding addtional scattering loss. Figure 5-3 illustrates this funtionality. Figure 5-3 (a) is a top-view schematic of the SNSPD integrated with the waveguide and inverse-taper coupler. The evolution of the TE-like mode inside the inverse-taper coupler is shown in (b), (c), and (d), which show the distribution of the electric field at the facet, in the middle, and at the end of the inverse-taper coupler, respectively. As the width

of the taper increases, the mode size inside the taper decreases, and the light is more concentrated inside the core layer. The mode size in (b) is smaller than that in (c); the mode in (d), compared with the mode in (c), is smaller in the y direction. To give a more quantitative comparison, Figure 5-4 (a) and (b) show the distribution of E_x at $y = 150$ μm and at $x = 0$, respectively. The capability of the inverse-taper coupler to shrink the mode size can be clearly seen. The evolution of another mode, the TM-like mode, is similar.

We then design the region of the waveguide with the NbN nanowire by varying w_w. For each w_w, we use finite-element analysis to find the complex effective index, n_{eff}, of the waveguide composed of the Si_3N_4 core, the SiON cladding, and the NbN. The larger the imaginary part of n_{eff}, $\mathrm{Im}(n_{eff})$, the stronger the absorption in the NbN. In this way, we can find the optimized w_w, which can yield the largest $\mathrm{Im}(n_{eff})$. The absorptance of the NbN is calculated by

$$A = 1 - \exp[-(2\pi/\lambda_0) \times \mathrm{Im}(n_{eff}) \times 2 \times l_n], \tag{5.5}$$

where λ_0 is the wavelength (1.55 μm).

The imaginary part of the effective index of the waveguide $\mathrm{Im}(n_{eff})$ is plotted in Figure 5-5 as a function of the width of the waveguide, w_w. As w_w increases, more light is confined within the Si_3N_4 layer, and therefore the spatial overlap between the NbN and the mode increases; however, further increase of w_w results in a drop of $\mathrm{Im}(n_{eff})$ because the mode is spread along the Si_3N_4 core, and its overlap with the NbN at the center becomes smaller. Thus, $\mathrm{Im}(n_{eff})$ reaches its maximum 0.00875 when w_w is 1300 nm for TE-like polarization. The absorption for the TE-like mode is much stronger than that for the TM-like mode because the electric field of TM-like field is in the y-direction, and in this direction, the NbN is only 4-nm thick. To adiabatically couple the light from the 450- or 500-nm wide coupler tip to the 1300-nm wide waveguide, we use a 500-μm long inverse taper.

In Figure 5-6, we then plot optimized $\eta_c \times A$ for the TE-like mode as a function of l_n. The $\eta_c \times A$ exponentially increases with l_n, then at $l_n \sim 50$ μm, it starts to

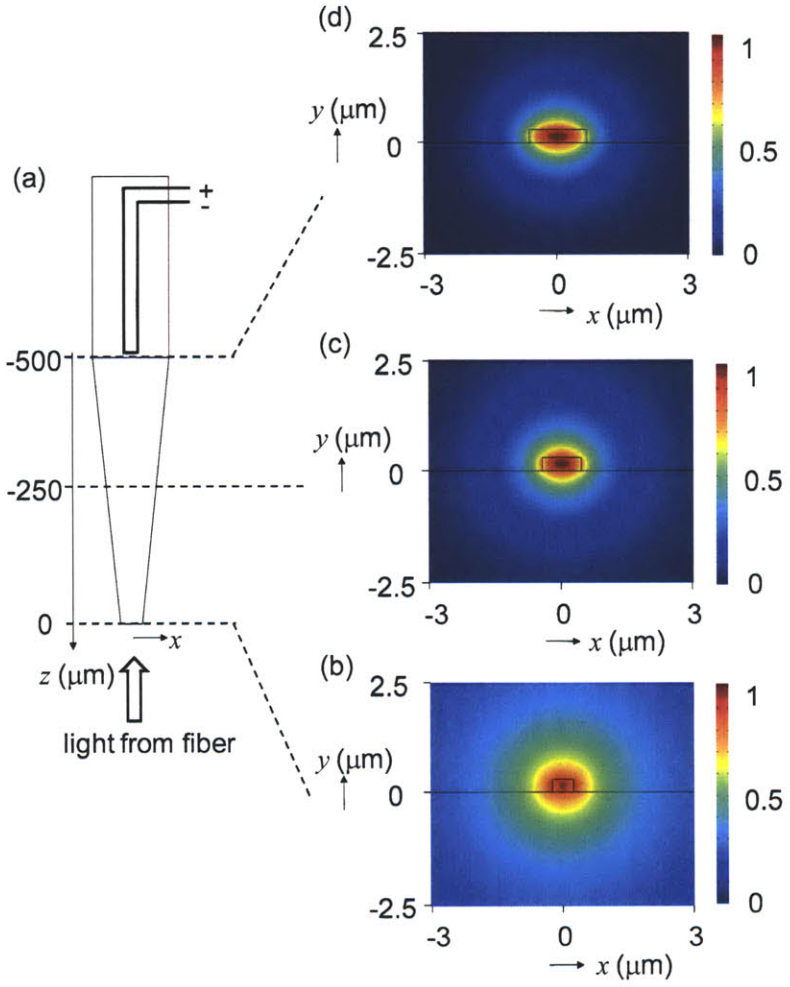

Figure 5-3: Evolution of the TE-like mode inside the inverse-taper coupler. (a) shows a top-view schematic of the inverse-taper coupler as well as the waveguide and the nanowire; (b) shows the distribution of the x-component of the electric field at the facet of the inverse-taper coupler; (c) shows the distribution of the x-component of the electric field in the middle of the inverse-taper coupler; (d) shows the distribution of the x-component of the electric field at the end of the inverse-taper coupler.

saturate, slowly approaching its upper bound 0.76: further increasing the nanowire length does not significantly increase the $\eta_c \times A$. We note here that we have not taken into account the material optical loss of Si_3N_4 because it can be made as small as 5 dB/cm by the PECVD process followed by annealing [81]. The total length of the coupler and the waveguide is about 525 μm, and the estimated additional material

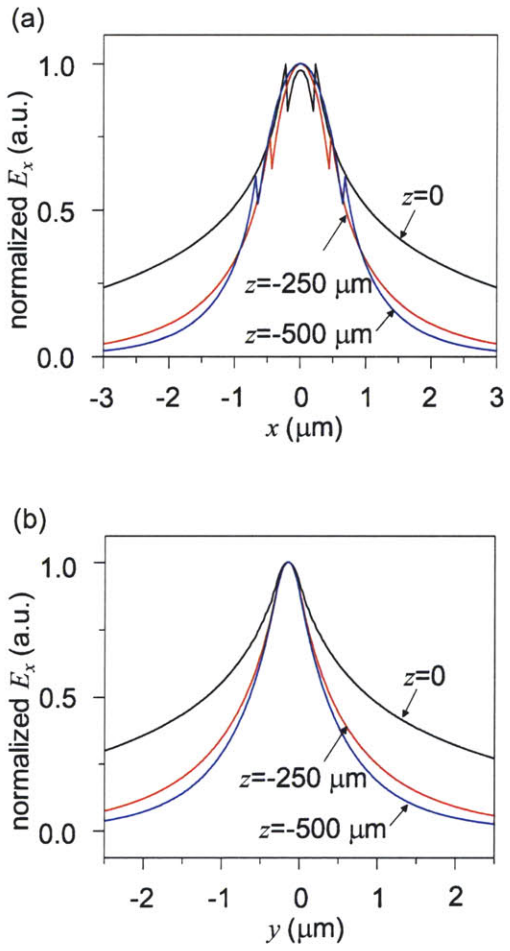

Figure 5-4: Distribution of the x-component of the electric field in TE-like mode inside the inverse-taper coupler at (a) $y = 150$ μm and (b) $x = 0$.

loss is only ~0.2 dB.

5.3 Comparison with cavity-integrated SNSPDs

Let us compare the performance of the waveguide-integrated SNSPD and the traditional cavity-integrated SNSPD [2], for TE- or TM-like polarizations. As mentioned above, the waveguide-integrated SNSPD can achieve a $\eta_c \times A$ of 0.76 with a 50-μm long NbN nanowire, and is directly coupled with a single-mode fiber. For cavity-integrated

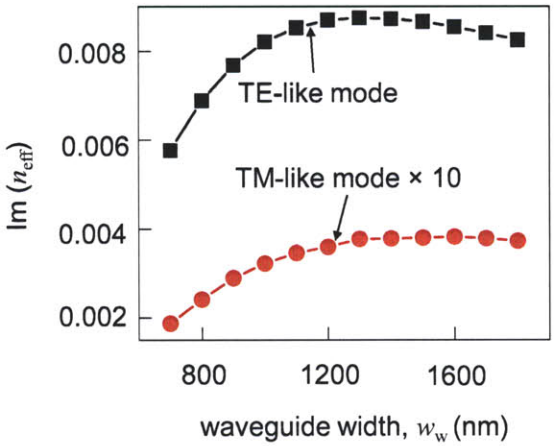

Figure 5-5: Simulated imaginary part of the complex effective index as a function of the width of the waveguide. The NbN nanowire dominantly absorbs photons in the TE-like mode. The initial increase of the $\mathrm{Im}(n_{\mathrm{eff}})$ with the increase of the waveguide width is due to the mode size becoming smaller as the width of the core layer increases. The energy in the mode is more concentrated, resulting in a larger overlap between the mode and NbN nanowire. On the other hand, further increasing the width decreases the absorption because the mode is concentrated in the core layer of the waveguide and the overlap between the mode and NbN nanowire decreases.

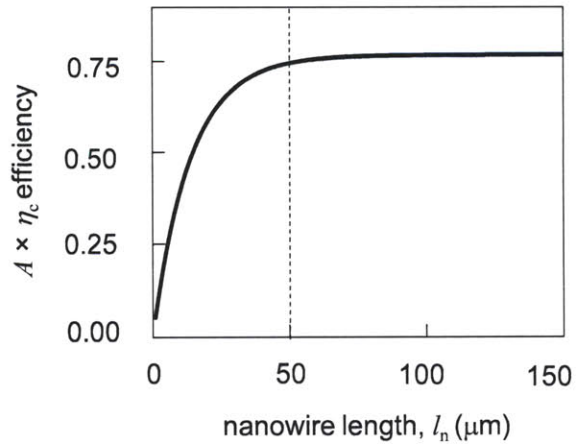

Figure 5-6: Simulated $A \times \eta_{\mathrm{c}}$ efficiency as a function of the length of the nanowire. At $l_{\mathrm{n}} \sim 50$ μm, $A \times \eta_{\mathrm{c}}$ efficiency saturates at 75%.

SNSPDs, on the other hand, the optimized absorptance is 0.68, independent of the total length of the nanowire. In contrast, the coupling efficiency is dependent on the length of the nanowire: (1) for a 3-μm-by-3-μm SNSPD coupled with a single spatial mode with MFD = 9.8 μm, a similar mode-size with a single-mode fiber, the optimized coupling efficiency is ~0.15, and therefore, $\eta_c \times A$ is ~0.10; (2) for a 10-μm-by-10-μm SNSPD coupled with the same spatial mode, the optimized coupling efficiency is ~0.85, and therefore, $\eta_c \times A$ is ~0.58; (3) for a 3-μm-by-3-μm SNSPD coupled with a single spatial mode with MFD = 5 μm, a similar mode-size with a fiber-focuser at its beam waist, the optimized coupling efficiency is ~0.5, and therefore, $\eta_c \times A$ is ~0.34; (4) a 10-μm-by-10-μm SNSPD coupled with the same spatial mode, the coupling efficiency is ~1, and therefore, $\eta_c \times A$ is ~0.68. Thus, one can see that the $\eta_c \times A$ of the waveguide-integrated SNSPD exceeds the $\eta_c \times A$ in the four cases without waveguide coupling. Although the total length of the NbN nanowire in a 3-μm-by-3-μm SNSPD is about 45 μm, similar to the length of the nanowire in a waveguide-integrated SNSPD, its $\eta_c \times A$ is much smaller, even coupled with a fiber focuser. Thus, we conclude that the waveguide-integrated SNSPD should be able to work with simultaneously high speed and high $\eta_c \times A$, and it is directly coupled with a single-mode fiber.

We estimated the reset time of the waveguide-integrated SNSPD to be 3.4 ns. Because the total length of the nanowire in the waveguide-integrated SNSPD is 50 μm, similar to the length of the nanowire in the meander covering a 3-μm-by-3.3-μm area [2], we assumed that their reset time is the same. Details of the estimation appear in Appendix B.

5.4 Development of fabrication process

The process for fabricating waveguide-integrated SNSPDs is composed of two major steps: (1) fabrication of NbN nanowires; (2) integration of the nanowires with waveguides.

The process for fabricating the nanowire illustrated in Figure 5-1 was similar

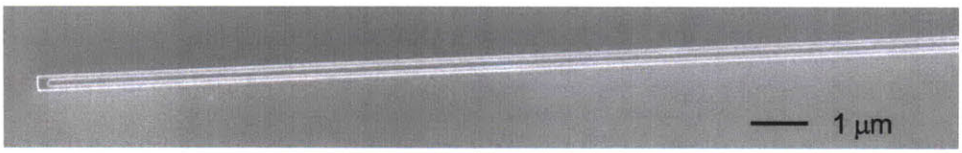

Figure 5-7: Scanning-electron micrograph of the nanowire for waveguide integration. The image shows the HSQ structure on NbN before reactive-ion etching (see the schematic in Figure 5-1).

to the process used to fabricate the nanowire meander in Chapter 2. The major difference is that the electron dose used here in scanning-electron-beam lithography was significantly higher than the dose used to fabricate the nanowire meander. The dose factor used here was ~4, compared with ~1.7 used for the meander.[6] The reason for the difference is the proximity effect. The electrons scattered by the adjacent structures in a meander contribute to the dose, and therefore, the appropriately assigned dose factor needs to be lower. The nanowire structure obtained before RIE is shown in Figure 5-7.

We integrated the nanowire with a waveguide using the Poly(methyl methacrylate) (PMMA) process.[7] We first deposited a layer of 300-nm thick Si_3N_4 on top of the chip using PECVD (platen temperature: 300 °C; showerhead temperature: 250 °C; pressure: 550 mTorr; RF power: 60 W; gas flow: 1960-sccm N_2, 40-sccm SiH_4, and 20-sccm NH_3). We then spun 200-nm thick PMMA (4%) and baked the PMMA at 180 °C for one hour. We exposed the PMMA by scanning-electron-beam lithography to define the core layer of the waveguide, which was aligned with the nanowire. After e-beam writing, we developed PMMA in a 2:1 IPA-MIBK mixture for 60 sec at 21 °C. We evaporated 40-nm nickel (Ni) and did liftoff in NMP at 105 °C for 20 min. We used the remaining Ni as the hard mask and performed RIE etching to transfer the pattern to Si_3N_4 using CF_4 as the reactive gas (98-W RF power). Finally, we stripped Ni off using Ni etchant.

The optical micrograph of the resulting waveguide structure is shown in Figure 5-

[6]Dose factor 1 corresponds to an electron dose of 300 $\mu C/cm^2$. We run a dose matrix to get the precise dose before a real e-beam writing.

[7]If the core layer of the waveguide is designed to be silicon, we can also use an HSQ process, which will be discussed later.

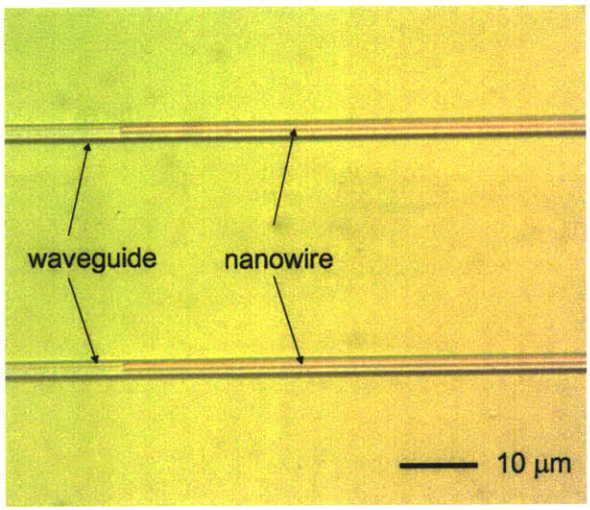

Figure 5-8: Optical micrograph of the waveguides aligned with the nanowires. The nanowires are under the waveguides, but not perfectly aligned with them.

8. Clearly, the nanowires are aligned with the waveguides, but not perfectly aligned: the nanowires are off the central lines of the waveguides. The alignment marks we used in SEBL writing were crosses, each of which was composed of two 0.5-μm-by-5-μm orthogonal bars. The misalignment, defined as the distance between the central line of the nanowire sturcture and the central line of the waveguide, was estimated to be 50 nm. This misalignment would decrease the absorptance of NbN per unit length. Precise alignment in e-beam lithography is a challenge in this process. Spatial-phase locked electron-beam lithography [82] could make a better alignment between the nanowire and the waveguide.

After integrating the waveguide, we diced and cleaved the chip to get smooth waveguide facets. We first made a ~400-μm deep cut on the back of the ~500-μm thick sapphire substrate using a die saw, and then cleaved the chip along the cut. After the chip was successfully cleaved, the end of the waveguide was imaged using an optical microscope (see Figure 5-9), and the facet of the waveguide was imaged using a scanning electron microscope (see Figure 5-10). Cleaving the sapphire substrate was not as easy as cleaving a silicon substrate. This step occasionally generated defects on the waveguides.

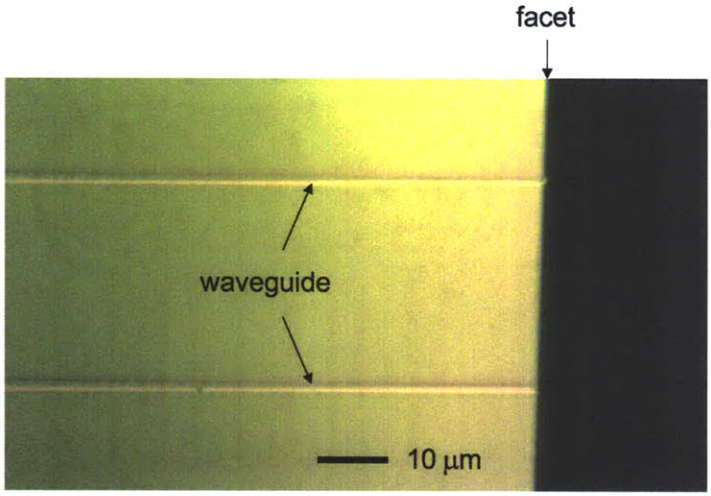

Figure 5-9: Top-view optical micrograph of the waveguides after being cleaved at the facet.

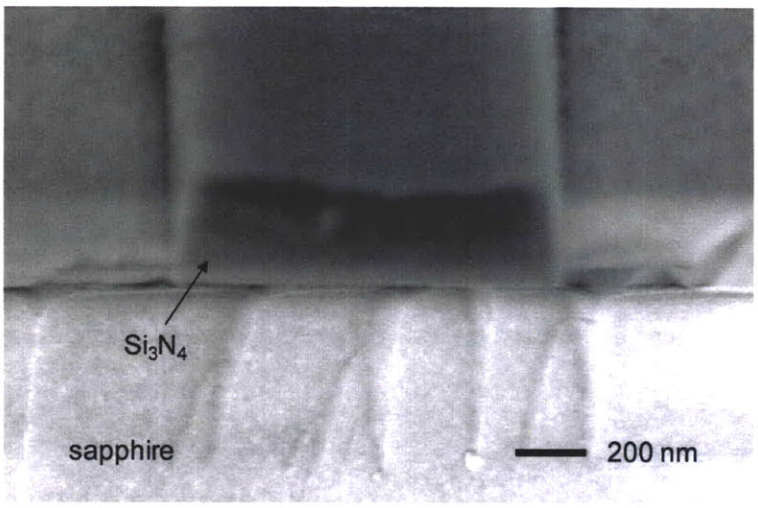

Figure 5-10: Cross-section scanning-electron micrograph of the waveguide after being cleaved at the facet.

To add the cladding layer, one can deposit SiON by PECVD [83], use S1813 as photoresist, perform optical lithography aligned with the core layer of the waveguide to define the top cladding layer, soak the chip in chlorobenzene to create an overhang structure followed by development, evaporate Ni followed by liftoff, use the Ni as the mask to etch SiON by RIE, and finally, strip away the Ni. This process is similar to the process to fabricate the core layer, but the required alignment does not need to be precise.

Alternatively, it is easier to use HSQ instead of SiON as the cladding layer. One can simply spin on HSQ, expose it using e-beam lithography, and develop the HSQ. Although the cladding layer needs to be aligned with the core layer, this alignment only needs to be a rough alignment. The reason to expose and develop HSQ is to avoid the coverage of the contact pads by HSQ.

We confirmed that these two steps, (1) fabrication of the NbN nanowires and (2) integration of the nanowires with the waveguides, were compatible. In other words, the second step did not damage the nanowires fabricated in step (1). We observed photon counting by the nanowires before and after step (2), suggesting that the process was satisfactory. Of course, further quantitative evaluation of the process would be the next step.

If the core layer of the waveguide is designed to be silicon, one can also use an HSQ process [84]. The key of this process is to use HSQ as the e-beam resist to define the core layer of the waveguide, and also use the developed HSQ as the mask to transfer the pattern to the silicon layer by RIE using hydrogen bromide (HBr) as the reactive gas.

5.5 Summary

This chapter has focused on the concept, design, and process development of the waveguide-integrated SNSPDs. Although there are challenges in the fabrication process, for instance, the precise alignment between the waveguide and the nanowire, it is equally challenging to test and package these devices, which will be the next

step. For testing, we need to couple light from a fiber probe to the waveguide in a cryogenic probe station. For packaging, we can directly attach and glue a fiber to the waveguide facet with alignment. This practice has been done in industry and in research.[8] Thus, including the fiber attachment as a part of the fabrication process may be a solution.

The waveguide-integrated SNSPDs proposed and discussed in this chapter are ideal for a system that is already fiber-coupled, for instance, a fiber-based QKD system. Free-space systems can benefit from the convenience of fiber-delivery to the detector without using beam-steering optics or a telescope-mounted cryostat. More importantly, the waveguide-integrated SNSPDs are compatible with various photonics-on-a-chip technologies. For instance, one can conveniently integrate it with one or multiple ring resonators [73, 78] so that the SNSPDs acquire the ability to distinguish the wavelength of the incident photons. This feature could facilitate SNSPDs for applications in integrated wavelength division multiplexing systems. In the future quantum optic circuits on a chip [85, 86, 87], all the components including quantum optic sources and logic gates will be integrated and connected via waveguides, and therefore, the dominant coupling loss from the fiber to the waveguide (i.e., $\sim$1.2 dB calculated in Section 5.2) can be eliminated. The detector will be more efficient.

[8] For instance, the fiber-coupled nonlinear crystal waveguide mentioned in Chapter 3 was prepared in a similar way.

Chapter 6

Summary and future directions

6.1 Summary

This thesis investigated efficient superconducting-nanowire single-photon detectors (SNSPDs) and their applications in quantum optics. The major results include the following:

- A fiber-coupled SNSPD system in a closed-cycle cryocooler has been built on MIT campus, demonstrating 24% system detection efficiency with a dark count rate of ~1000 counts/sec.

- This system has been used in high-quality polarization-entanglement distribution. The visibility in Hong-Ou-Mandel interference after distribution was measured to be 99.2% at the pump power of 25 μW. This visibility is the highest that has ever been reported for waveguide-based entangled-photon sources. We obtained a pair rate of 5.8 pairs/sec at a pump power of 25 μW and two-photon quantum interference visibility of 97.7%.

- An SNSPD integrated with optical nano-antennae has been demonstrated. This detector has an active area of 9 μm by 9 μm, a device efficiency of 47%, and a reset time of 5 ns. This combined performance was previously impossible.

- Waveguide-integrated SNSPDs have been proposed and designed. This device

structure allows photons to be efficiently coupled into a short nanowire. To be more specific, 75% of the incident photons from a single-mode fiber can be coupled into a 50-μm long nanowire. The corresponding reset time is estimated to be 3.4 ns.

6.2 Future directions

It is foreseeable that this SNSPD system with 24% system detection efficiency will have more applications and impact. Generally speaking, it is suitable for any measurement of weak optical signals at visible and infrared wavelengths, in the field of quantum optics, spectroscopy, detecting luminescence and time-resolved photoluminescence, and diagnosis of the problems in VLSI circuits. One on-going experiment using this system is to measure the photoluminescence and time-resolved photoluminescence from single lead sulphate (PbS) quantum dots, which emit weak light near the wavelength of 1.5 μm. From the measured luminescence we can study the dynamics of the carriers, excitons, and bi-excitons in the quantum dots [88]. In the field of quantum optics, we have demonstrated polarization-entanglement distribution, which has been presented in Chapter 3. A natural extension of this experiment would be quantum key distribution. The SNSPD system would also be useful in quantum illumination [89], quantum metrology [90], and detecting the fluorescence of ions in ion traps for quantum computation [91]. Using the SNSPD system as a scientific instrument for various applications is the first direction for the future.

Although the SNSPD system with 24% system detection efficiency has already shown its impact in applications and will have more impact, this efficiency is still not 100%. For some extreme applications, such as linear optical quantum computation [92], almost 100% system detection efficiency is needed. What are the theoretical and practical limits of the system detection efficiency? To answer this question, we need to re-examine η_c, A, and P_r .

First of all, coupling efficiency, η_c, can approach 100% if the active area of the SNSPD is much larger than the size of the optical mode. If we momentarily disregard

the speed of the detector, we can fabricate an SNSPD with a large enough area to tolerate the dynamic misalignment induced by vibration. However, increasing the area decreases the yield of good detectors. Interestingly and also surprisingly, the reported large-area SNSPDs with similar sizes to our detector [7], except for the antenna-integrated SNSPD presented in Chapter 4, all have device efficiency $\leq$30% uniformly [40, 8, 7, 93, 29] at telecom wavelengths. Why? Is it simply because the current technology cannot avoid constrictions, or is there any limitation that is more fundamental?

Secondly, absorptance, A, can approach 100% when additional advanced photonic structures are added to the nanowires. For instance, in Chapter 4, we have discussed SNSPDs integrated with optical nano-antennae to enhance the absorptance of a short nanowire to optimize the speed and system detection efficiency (the device efficiency and in this case, the active area). If we do not care about the speed for a moment, we can decrease the pitch of the meander from 600 nm to 200 nm, and the calculated absorptance of the nanowire is increased to $\sim$96%.[1] The waveguide-integrated SNSPD can essentially absorb almost all the light already coupled into the waveguide. The limiting factor is the material loss of the waveguide, on the order of 5 dB/cm, which is negligibly small in this case. Another approach to make the absorptance >90% is to increase the confinement of the Fabry-Pérot cavity; for example, the optimized absorptance of a 200-nm pitch, 4.5-nm thick NbN can achieve 96% using a NbN meander on a SiO_2-on-Si substrate integrated with a Fabry-Pérot cavity.

Thirdly, this thesis has focused on η_c and A, but it has not touched upon intrinsic quantum efficiency, P_r. Furthermore, a quantitative understanding of P_r is still lacking in the field of SNSPDs. Monte Carlo simulation may be helpful for understanding P_r quantitatively. This thought was inspired by an analogy between two processes: (1) the scattering of hot-electrons inside the NbN nanowire with electrons, phonons, and Cooper pairs and (2) the scattering of incident electrons inside the resist with electrons, lattice, and secondary electrons. The initial energy in process (1) is on the

[1] Of course, it would be more challenging to fabricate a 200-nm pitch antenna structure than to fabricate a 600-nm pitch structure.

order of 1 eV (the incident photon energy) and the initial energy in process (2) is on the order of 10 keV. The essence of Monte Carlo simulation is to repeat random sampling for numerical exprimentation. Specifically for modeling process (2), incident electrons are repeatedly sent to the resist. Each electron has a unique track because of the elastic and inelastic scatterings, and the ensemble of these tracks shows the properties of the electron beam, for example, how the beam expands inside the resist due to scattering. In the analogy, for modeling process (1), we can study the formation of the hotspot from the point of view of the classical collision of particles. Three types of collision exist here: (1) electron-electron scattering, (2) electron-phonon scattering, and (3) electron-Cooper pair scattering. These scatterings eventually drive the system equilibrium. The domain where there are no Cooper pairs inside the nanowire can be regarded as the initial hotspot before the further expansion due to Joule heating. From one incident photon, we can get one domain. If we repeat the process, we can get an ensemble of such domains. This ensemble may yield information about P_r and timing jitter as well.

The work on SNSPDs integrated with optical nano-antennae documented in this thesis is to establish the fabrication process and demonstrate a prototype, the performance of which matches the design and exceeds the performance of previous devices. As far as the fabrication process is concerned, several improvements may further enhance the performance. For example, instead of evaporation, sputtering may be a better way to deposit gold conformably to get rid of the voids. It is also worth trying other materials such as silver and aluminum to make a comparison of the detector performance with the performance using gold. As far as device physics is concerned, it would be interesting to perform a measurement of device efficiency and absorptance, similar to the measurement in [66]. From this measurement, we could obtain the information about P_r for both polarizations. There are experimental indications that the P_r is different for different polarizations, perhaps due to the different electric field distribution inside the nanowire. The measurement of P_r for SNSPDs integrated with optical nano-antennae would test this hypothesis in a different device structure, in which the electric field distribution inside the nanowire is different [66]. This

measurement may shed light on how P_r is dependent on the field distribution, and furthermore, on the polarization of the incident photons. As far as the physics of nano-antennae is concerned, it is possible to give an analytical description. The key is to expand the incident plane wave according to the cavity modes. A similar model has been discussed in [94] without absorbing media at the aperture of each cavity. An analytical description could give a better picture of how (in what functions) the absorption enhancement depends on each geometrical parameter. Such a description may simplify the design process. Very recently, circuit models have been used to describe the physics of optical nano-antennae [95]. It is worth trying to build a circuit model to understand the optical properties of SNSPDs integrated with optical nano-antennae.

For the waveguide-integrated SNSPDs, this thesis focused on the concept, device design, and development of the fabrication process. Although there are challenges in fabrication including aligning the waveguide with the nanowire, it is equally challenging to test these devices. It is quite doable to cleave the waveguide, align the fiber with the waveguide, and attach the fiber to the waveguide; however, it is not clear whether this alignment can be maintained at low temperature. These experiments are the key steps for applying the waveguide-integrated SNSPDs in a system that is already fiber coupled. On the other hand, for quantum optic integrated circuits [85, 86, 87], the goal is to integrate all the components on one chip, and these components are therefore all connected by waveguides, including sources, logic gates, and detectors. In this case, the challenge to couple light to the waveguide is eliminated. The new challenge instead is that all the components have to work at the cryogenic temperature at which the detector works. Regardless of these challenges, it is foreseeable that waveguide-integrated SNSPDs will have more applications that are different than the existing applications of SNSPDs in the meander structure. This waveguide-integrated structure makes SNSPDs compatible with various on-chip photonic technologies that have been developed in recent years for optical interconnects inside a computer, for example, inverse-taper couplers and ring resonators. Applying these technologies to quantum optics on a chip would be interesting.

Although this thesis has focused on single-element SNSPDs and their applications, the concepts and device structures developed here can also be applied to multi-element SNSPDs [37] and SNSPDs composed of parallel nanowires [38]. For instance, four elements with antenna integration can further expand the active area of the detector; SNSPDs composed of parallel nanowires can also be integrated with waveguides. Thus, the concepts and device structures discussed here are quite general. Single-element SNSPDs are the foundations for other device structures.

In summary, superconducting-nanowire single-photon detectors are a promising technology for infrared photon counting and detection. Their excellent performance has already enabled applications and experiments that were previously impossible. More applications will be demonstrated as the performance of SNSPDs is continuously being enhanced. Such enhancement really relies upon the understanding of the device physics, the design of novel device structures, and the enabling technology to make the engineering *tour de force* happen. The ultimate goal is, of course, to the make SNSPDs more convenient to use, with ideal characteristics and more functionalities.

The work documented in this thesis is one step towards this goal.

Appendix A

Standard operation procedure and maintenance of the SNSPD system

A.1 Standard operation procedure

The SNSPD has been packaged in the closed-cycle cryocooler with a fiber as the input channel and an SMA cable as the output channel. A user of the system just needs to follow the following steps in order to use the system.

A.1.1 Before using the system

Follow the following steps to set up the system before using it. See the schematic of a typical experimental setup in Figure 2-7.

1. Take off the connector cap from fiber cable 1.[1]

2. Clean the facet of fiber cable 1 with a fiber connector cleaner.

3. Take off the connector cap from the fiber connected with the polarization controller (denoted as fiber 2).

4. Clean the facet of fiber 2.

5. Clean the fiber adapter with compressed air.

[1]There is a fiber in a metal jacket directly connected with the cryocooler. There is another fiber cable (denoted as fiber cable 1) connected with this fiber in the metal jacket. Do not disconnect fiber cable 1 from the fiber in the metal jacket unless necessary.

6. Connect fiber 1 and fiber 2 with the fiber adapter.

7. Take off the 50-Ω SMA terminator from the cable connected with the cryocooler (denoted as cable 1).

8. Take off the 50-Ω SMA terminator from the cable connected with the bias T (denoted as cable 2).

9. Connect the cable 1 and the cable 2 with an SMA connector by using an SMA torque wrench.

10. Connect the cable 3 connected with the output of the amplifiers with the oscilloscope.

11. Turn on the power of the universal counter, the precision attenuator, the power supply for the RF amplifiers.

12. Set the current to be 13 μA and adjust the oscilloscope to see the pulses of dark counts.

13. Disconnect the cable from the oscilloscope and connect it with the counter.

14. Set the bias current to be 0.

15. Decrease the threshold of the universal counter from maximum so that there are just no counts.

16. Set the bias current to be 95% of the critical current.

17. Set the attenuation of the precision attenuator to be 90 dB.

18. Turn on the power of the laser and set the power of the laser to be 100 μW.

19. Adjust the polarization controller to maximize the counting rate.

20. If the detector switches itself to the latched state at any time, turn off the bias current and turn it on again.

21. Disconnect the fiber from the laser and connect it with the output fiber from the user's setup.

The system is ready to use.

A.1.2 After using the system

Follow the following steps after using the system.

1. Turn off the power of power supply of the amplifiers, the precision attenuator, and the universal counter.

2. Disconnect the fiber cable 1 from the polarization controller. Cap both.

3. Disconnect the SMA cable 1 from the bias T. Terminate it with a 50-Ω SMA terminator.

4. Organize the fiber cable and the SMA cable. Tape them fast to the rack of the cryocooler so that they will not move due to gravity or vibration.

A.2 Maintenance

It is recommended that the adopter of the system follow the following steps to maintain the system when maintenance is needed. However, maintaining the system relies upon the status of the cryocooler and the experience of the adopter. So, this procedure is not a standard operation procedure.

A.2.1 Optical alignment

The following steps are recommended for optical alignment when necessary:

1. Follow the steps in **Before using the system**.

2. Make sure the control knobs of the three nanopositioners are at off positions. Turn on the power supply of the controller.

3. Coarse alignment

(a) Set the voltage of the Z positioner to be 30 V and set the frequency to be 1000 Hz.

(b) Move the Z positioner down approximately 2 mm (push the button up). Observe the decrease of the counts on the display of the counter.

(c) Increase the power of the laser so that the reading of the counter is maintained to be between 15 kHz to 20 kHz.

(d) Set the voltage of the X and Y positioners to be 30 V and set the frequency to be 1000 Hz.

(e) Adjust the X and Y positioners to maximize the counting rate.

(f) If the detector switches, decrease the optical power sent to the SNSPD by adding 10 dB more attenuation. Turn off and on the bias current.

(g) Move up the Z positioner slowly (push the button down). The counting rate should keep increasing and the detector keeps switching. Repeat (f).

(h) If the counts start to decrease as the Z positioner is moving up, it means that the position is too high. Slowly move it back.

4. Fine alignment

(a) Set the voltage of the X, Y, Z positioners to be 20 V and the frequency to be 100 Hz.

(b) Alternatively adjust X, Y, Z positioners until no further increase of the counts is observed.

A.2.2 Procedure to measure dark count rate and system detection efficiency

The following steps are recommended for measuring the dark count rate and the system detection efficiency when necessary:

1. Follow step 1 to step 15 in **Before using the system** to set up the system.
2. Sweep the bias current and record the corresponding dark count rate.
3. Do steps 17, 18, and 19 in **Before using the system**.
4. Sweep the bias current and record the corresponding counting rate.
5. At low bias, decrease the attenuation so that the count rate is maintained to be ~20 kHz.
6. Subtract the dark count rate from the counting rate in step 4 for each bias.
7. Calculate the system detection efficiency using Equation 2.1 in Chapter 2.

A.2.3 Procedure to shut down the system

The following steps are recommended for shutting down the system when necessary:

1. Turn off the power of the compressor unit.
2. Shut down the cooling water supply of the compressor unit.

A.2.4 Procedure to start the system

The following steps are recommended for restarting the system when necessary:

1. Make sure that the temperature of the system is room temperature.

2. Open the vacuum valve between the pump and the system.

3. Turn on the pump and wait until the pressure is $< 10^{-4}$ torr.

4. Open the valve for the cooling water for the compressor unit.

5. Turn on the compressor unit. A periodic noise should appear and temperature starts to drop.

6. The pressure also drops during cooling down. Close the vacuum valve between the pump and the cryocooler when the pressure is $< 10^{-6}$ torr.

7. Shut down the pump.

A.2.5 Procedure to refill the compressor unit with ultra-pure helium gas

The pressure of the refrigerant in the compressor unit can drop as time passes by, and it is necessary to refill the unit with ultra-pure helium gas when the pressure is too low to cool the cryocooler. It is recommended to perform this operation with an experienced technician.

1. Connect the helium gas cylinder (99.995% helium gas) [96] with the compressor unit.

2. Open the valve of the gas cylinder slowly.

3. Watch the increase of the pressure on the gauge on the compressor unit until the pressure reaches recommended value, 1.91 ± 0.098 MPa at 20 °C, in the manual of the cryocooler [96].

4. Close the valve of the gas cylinder slowly.

5. Disconnect the helium gas cylinder with the compressor unit.

Appendix B

Calculation of reset time

Reset time, τ, is defined in Chapter 1 as the time, after a detection event, needed for the device efficiency to recover to 90% of the device efficiency if there were no detection. It can be measured directly [5] or calculated from the kinetic inductance of the detector, L_k. Strictly speaking, L_k is a function of the current [97], i_b, flowing in the nanowire; but here, we assume that L_k is a constant.

The calculation of reset time is composed of two steps. First, from the measured relation between device efficiency (or system detection efficiency[1]) η and current i_b, we can obtain the bias current $I_{90\%}$ that is corresponding to 90% of the efficiency at the bias current I_b[2] by

$$I_{90\%} = \eta^{-1}[90\%\eta(I_b)], \tag{B.1}$$

where $\eta^{-1}[\cdot]$ is the inverse function of $\eta[\cdot]$. Second, from L_k, we can obtain the reset time τ that is needed for the current to recover from 0 to $I_{90\%}$ by

$$1 - \exp[1 - \tau/(L_k/R)] = I_{90\%}/I_b, \tag{B.2}$$

[1]Here, the coupling efficiency as a constant does not change anything in the calculation. So, η can represent either system detection efficiency or device efficiency in this Appendix.

[2]In this Appendix, we use i_b to refer to the actual current in the nanowire, and use I_b to refer to the bias current that we set to operate the detector.

where $R = 50\ \Omega$. Or equivalently,

$$\tau = (L_k/R)\ln[1/(1 - I_{90\%}/I_b)]. \tag{B.3}$$

In Chapter 2, we used $L_k = 340$ nH [5]. The bias current was set to be $I_b = 0.99I_c$. $I_{90\%} = 0.97I_c$ is obtained from $\eta - i_b$ relation that we measured. We calculated the reset time to be 26.5 ns.

In Chapter 4, we measured the kinetic inductance to be $L_k = 100$ nH. The bias current was set to be $I_b = 0.975I_c$. $I_{90\%} = 0.9I_c$ is obtained from $\eta - i_b$ relation that we measured. We calculated the reset time to be 5.1 ns.

In Chapters 4 and 5, we estimated the reset time of an SNSPD composed of a 50-μm long nanowire to be 3.4 ns. This estimation is based on Reference [5]. In Reference [5], the reset time of an SNSPD composed of a 120-μm long nanowire was measured to be 8.5 ns, and its L_k was measured to be 110 nH. In addition, the L_k of a 50-μm long nanowire was measured to be 44.5 nH. We thus estimated the reset time of an SNSPD composed of a 50-μm long nanowire by 44.5 nH $\times$ 8.5 ns/110 nH, which is 3.4 ns. The assumption of this estimation is that $\eta - i_b$ relations are identical for the SNSPD composed of the 50-μm long nanowire and the SNSPD composed of the 120-μm long nanowire.

As a final note, the kinetic inductance per square was calculated to be ~ 90 nH/□ based on the data in Reference [5] whereas it was calculated to be ~ 60 nH/□ based on the data of SNSPDs integrated with optical nano-antennae. This smaller kinetic inductance per square, in addition to the shorter length of the nanowire, obviously contributed to the enhanced speed of the SNSPDs integrated with optical nano-antennae presented in Chapter 4. In addition to the difference in film thickness, the integration of optical nano-antennae could have an effect on the kinetic inductance. The integration of optical nano-antennae could also add additional capacitance. These effects are not totally clear for now. A measurement and comparison of the kinetic inductance using the network analyzer before and after adding the optical nano-antennae to the nanowires should be able to clarify these effects.

Appendix C

Fit of the optical constants of NbN using the Drude model

This appendix presents the details of fitting the measured complex optical refractive indices, $\tilde{n} = n + ik$, of NbN in a spectral range using the Drude model, which was further used to obtain the optical constants of NbN, used in Chapter 4 at mid-IR wavelengths, that were difficult to measure directly.

We measured the complex refractive indices of NbN thin film on sapphire substrate by ellipsometry in the spectral range between 270 nm (4.593 eV) and 1750 nm (0.709 eV),[1] and the raw data obtained and used for fitting are listed in Table C.1.

The dielectric constant of a metal under the Drude model can be expressed as

$$\epsilon(\omega) = \epsilon_r[1 - \frac{{\omega_p}^2}{\omega(\omega + i\Gamma)}], \tag{C.1}$$

where ω is the angular frequency of the light,[2] ϵ_r is the core dielectric constant, ω_p is the screened plasma freqency of the metal,[3] and Γ is the damping term. The complex refractive index and the dielectric constant are linked through $\tilde{n}^2 = \epsilon$. The fitting is to find the ϵ_r, ω_p, and Γ for NbN.

[1] A useful conversion in optics is $\lambda(\text{nm}) = \frac{1.24}{E(\text{eV})}$.

[2] The energy of the photon, E, is propotional to ω, i.e., $E = \hbar\omega$, where $\hbar$ is the reduced Planck constant.

[3] If the dielectric constant of the metal under the Drude model is written as $\epsilon(\omega) = \epsilon_r - \frac{{\omega_p}^{*2}}{\omega(\omega+i\Gamma)}$, ${\omega_p}^*$ is called the unscreened plasma freqency of the metal.

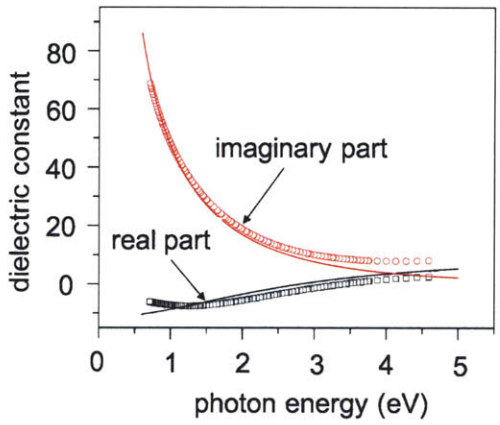

Figure C-1: Fit of the measured optical constants of NbN using the Drude model. The circles and squares are measured data, and the lines are fittings.

We fitted the data by adjusting the ϵ_r, ω_p, and Γ in Eq. C.1 until the ϵ_r-ω curve fitted the data well, judged by visual observation, as shown in Figure C-1. ϵ_r, $\hbar\omega_p$, and $\hbar\Gamma$ were found to be 9.7, 3.8 eV, and 2.57 eV, respectively, for NbN. The fitting judged by visual observation is subjective to some extent; a more objective way is to perform nonlinear least-square fitting.

Using the Drude model, we therefore calculated the dielectric constant of NbN at 4 μm to be $-11.3 + 173i$, or equivalently, the complex refractive index to be $9.01 + 9.61i$, which was used in Chapter 4.

The origin of possible errors includes the error in the measurement by ellipsometry, the fitting by the Drude model, and the fact that the data point of interest is outside the range of the data set obtained by measurement.

In addition to using the Drude model to fit the data, one can also use, for instance, two polynomial functions to separately fit the real and imaginary parts of the complex optical refractive indices. For example, fittings using two fifth-order polynomial functions yielded $n = 7.77 + 7.67i$ at the wavelength of 4 μm.

Table C.1: Refractive indices of NbN thin film measured by elliposmetry.

Energy (eV)	Wavelength (nm)	n	k
4.593	270.000	2.3504	1.7328
4.429	280.000	2.3129	1.7344
4.276	290.000	2.2756	1.7481
4.133	300.000	2.2399	1.7723
4.000	310.000	2.2070	1.8054
3.875	320.000	2.1775	1.8462
3.758	330.000	2.1519	1.8932
3.750	330.667	2.1504	1.8966
3.700	335.135	2.1405	1.9195
3.650	339.726	2.1312	1.9440
3.647	340.000	2.1306	1.9455
3.600	344.444	2.1226	1.9701
3.550	349.296	2.1148	1.9979
3.543	350.000	2.1138	2.0019
3.500	354.286	2.1079	2.0272
3.450	359.420	2.1019	2.0581
3.444	360.000	2.1013	2.0616
3.400	364.706	2.0969	2.0905
3.351	370.000	2.0931	2.1236
3.350	370.149	2.0931	2.1246
3.300	375.758	2.0903	2.1601
3.263	380.000	2.0891	2.1874
3.250	381.538	2.0889	2.1973
3.200	387.500	2.0887	2.2359
3.179	390.000	2.0891	2.2522
3.150	393.651	2.0900	2.2760
3.100	400.000	2.0927	2.3176

Table C.1 (Cont'd)

Energy (eV)	Wavelength (nm)	n	k
3.050	406.557	2.0969	2.3607
3.000	413.333	2.1027	2.4052
2.950	420.339	2.1102	2.4510
2.918	425.000	2.1160	2.4815
2.900	427.586	2.1194	2.4983
2.850	435.088	2.1304	2.5469
2.800	442.857	2.1433	2.5968
2.756	450.000	2.1563	2.6422
2.750	450.909	2.1580	2.6480
2.700	459.259	2.1748	2.7004
2.650	467.925	2.1936	2.7542
2.611	475.000	2.2099	2.7974
2.600	476.923	2.2145	2.8091
2.550	486.275	2.2376	2.8653
2.500	496.000	2.2629	2.9226
2.480	500.000	2.2737	2.9459
2.450	506.122	2.2905	2.9811
2.400	516.667	2.3205	3.0408
2.362	525.000	2.3450	3.0870
2.350	527.660	2.3530	3.1016
2.300	539.130	2.3879	3.1636
2.255	550.000	2.4220	3.2209
2.250	551.111	2.4255	3.2266
2.200	563.636	2.4657	3.2908
2.157	575.000	2.5030	3.3476
2.150	576.744	2.5087	3.3561
2.100	590.476	2.5546	3.4226
2.067	600.000	2.5868	3.4675

Table C.1 (Cont'd)

Energy (eV)	Wavelength (nm)	n	k
2.050	604.878	2.6033	3.4901
2.000	620.000	2.6551	3.5588
1.984	625.000	2.6724	3.5810
1.950	635.897	2.7101	3.6286
1.908	650.000	2.7591	3.6885
1.900	652.632	2.7682	3.6995
1.850	670.270	2.8298	3.7717
1.837	675.000	2.8463	3.7906
1.800	688.889	2.8947	3.8450
1.771	700.000	2.9334	3.8874
1.750	708.571	2.9633	3.9195
1.710	725.000	3.0202	3.9796
1.700	729.412	3.0355	3.9954
1.653	750.000	3.1064	4.0674
1.650	751.515	3.1116	4.0726
1.600	775.000	3.1916	4.1512
1.550	800.000	3.2758	4.2313
1.503	825.000	3.3588	4.3081
1.500	826.667	3.3643	4.3131
1.459	850.000	3.4406	4.3818
1.450	855.172	3.4573	4.3967
1.417	875.000	3.5210	4.4527
1.400	885.714	3.5550	4.4822
1.378	900.000	3.6000	4.5210
1.350	918.519	3.6576	4.5700
1.341	925.000	3.6776	4.5869
1.305	950.000	3.7538	4.6506
1.300	953.846	3.7654	4.6602

Table C.1 (Cont'd)

Energy (eV)	Wavelength (nm)	n	k
1.272	975.000	3.8286	4.7123
1.250	992.000	3.8787	4.7532
1.240	1000.000	3.9020	4.7722
1.210	1025.000	3.9740	4.8304
1.200	1033.330	3.9977	4.8495
1.181	1050.000	4.0447	4.8871
1.153	1075.000	4.1141	4.9423
1.150	1078.260	4.1230	4.9494
1.127	1100.000	4.1821	4.9962
1.102	1125.000	4.2490	5.0489
1.100	1127.270	4.2550	5.0537
1.078	1150.000	4.3146	5.1005
1.075	1153.490	4.3236	5.1076
1.055	1175.000	4.3790	5.1511
1.050	1180.950	4.3942	5.1630
1.033	1200.000	4.4423	5.2006
1.025	1209.760	4.4667	5.2197
1.012	1225.000	4.5045	5.2493
1.000	1240.000	4.5414	5.2781
0.992	1250.000	4.5657	5.2972
0.975	1271.790	4.6182	5.3383
0.973	1275.000	4.6258	5.3443
0.954	1300.000	4.6850	5.3906
0.950	1305.260	4.6973	5.4003
0.936	1325.000	4.7432	5.4363
0.925	1340.540	4.7789	5.4644
0.919	1350.000	4.8005	5.4814
0.902	1375.000	4.8569	5.5258

Table C.1 (Cont'd)

Energy (eV)	Wavelength (nm)	n	k
0.900	1377.780	4.8631	5.5307
0.886	1400.000	4.9125	5.5697
0.875	1417.140	4.9501	5.5995
0.870	1425.000	4.9672	5.6131
0.855	1450.000	5.0212	5.6560
0.850	1458.820	5.0401	5.6710
0.841	1475.000	5.0744	5.6984
0.827	1500.000	5.1269	5.7404
0.825	1503.030	5.1332	5.7455
0.813	1525.000	5.1787	5.7820
0.800	1550.000	5.2298	5.8231
0.787	1575.000	5.2803	5.8639
0.775	1600.000	5.3301	5.9043
0.763	1625.000	5.3793	5.9444
0.752	1650.000	5.4280	5.9842
0.750	1653.330	5.4344	5.9894
0.740	1675.000	5.4760	6.0236
0.729	1700.000	5.5236	6.0627
0.725	1710.340	5.5431	6.0788
0.719	1725.000	5.5705	6.1016
0.709	1750.000	5.6170	6.1401

Appendix D

Linearly polarized mode with a Gaussian profile to approximate the mode in a single-mode optical fiber

In Chapter 5, the mode in a single-mode optical fiber is treated as a linearly polarized mode with a Gaussian profile. This appendix explains this treatment and justifies the approximations.

A standard single-mode optical fiber is composed of a core layer with an optical index n_1 and a cladding layer with an optical index n_2. The diameter of the core layer, a, is between 8 μm and 10 μm, and the diameter of the cladding layer is ~125 μm. Because the field decays in the cladding layer and becomes negligibly small at the outer boundary of the cladding layer, the single-mode fiber can be modeled as a two-layer cylindrical dielectric waveguide. Furthermore, this waveguide satisfies the following weakly guiding condition: $0 < n_1 - n_2 \ll n_2$. The cladding layer is made of silicon dioxide ($n_2 \approx 1.46$), and the core layer is made of doped silicon dioxide. Typically, n_1 is only 1% - 5% larger than n_2 [98].

Because of the cylindrical symmetry, a standard single-mode fiber has two orthog-

onal modes. These two modes are degenerate in their dispersion relations, and have the same field distribution except for orthogonal polarizations. We thus focus on one of them.

Strictly speaking, the mode of such a two-layer cylindrical dielectric waveguide has six non-zero field components: E_i and H_i $(i = x, y, z)$. However, under the weak-guiding condition, the mode can be approximated by a linearly polarized mode with $E_y = 0$, $H_x = 0$, and other four nonzero components. This linearly-polarized-mode approximation is the first approximation used in this treatment.

Furthermore, the nonzero transverse components, E_x and H_y, satisfy the following relations: $E_x \propto J_0(hr)$ in the core layer, $E_x \propto K_0(qr)$ in the cladding layer, and $H_y = \frac{1}{\eta_f} E_x$ in both cladding and core layers, where the $J_0(\cdot)$ is the zeroth order Bessel function of the first kind, $K_0(\cdot)$ is the zeroth order modified Bessel function of the second kind, r is the radial coordinate in a cylindrical coordinate system, h and q are the transverse propagation constant in the core layer and the exponential decay constant in the cladding layer, respectively, and η_f is the wave impedance in the fiber [99, 98]. This field distribution can be approximated by a Gaussian distribution, i.e, $E_x \propto \exp(-\frac{r^2}{\omega_0^2})$, $H_y \propto \exp(-\frac{r^2}{\omega_0^2})$ in both core and cladding layers, where $2\omega_0$ is the mode-field diameter. This Gaussian-profile approximation is the second approximation used in this treatment.

To justify these two approximations, Figure D-1 presents a comparison between the simulated transverse electric field distribution, E_x, and the Gaussian distribution with a mode-field diameter of 9.8 μm used in Chapter 5. The parameters used in the simulation are $a = 9.5$ μm, $n_1 = 1.467$, and $n_1 = 1.46$. The similarity between these two distributions in Figure D-1 justifies the validity of using a linearly polarized mode with a Gaussian profile to approximate the mode in a single-mode optical fiber.

In summary, under this treatment, the transverse field components of the single-mode fiber used in Equation 5.1 are as follows: $E_x = E_0 \exp(-\frac{r^2}{\omega_0^2})$ and $H_y = \frac{E_0}{\eta_f} \exp(-\frac{r^2}{\omega_0^2})$ for the TE mode; and $E_y = E_0 \exp(-\frac{r^2}{\omega_0^2})$ and $H_x = \frac{E_0}{\eta_f} \exp(-\frac{r^2}{\omega_0^2})$ for the TM mode, where E_0 is a constant.

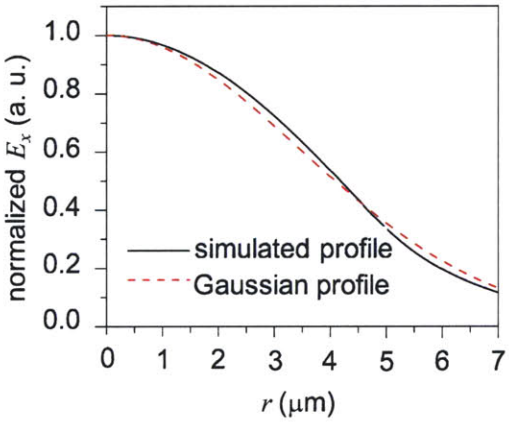

Figure D-1: Comparison between the simulated field distribution and the approximated distribution of E_x in a single-mode optical fiber. The similarity between these two distributions justifies the validity of using a linearly polarized mode with a Gaussian profile to approximate the mode in a single-mode optical fiber.

Bibliography

[1] G. N. Gol'tsman, O. Okunev, G. Chulkova, A. Lipatov, A. Semenov, K. Smirnov, A. Dzardanov B. Voronov, C. Williams, and R. Sobolewski. Picosecond superconducting single-photon optical detector. *Appl. Phys. Lett.*, 79(6):705–707, 2001.

[2] K. M. Rosfjord, J. K. W. Yang, E. A. Dauler, A. J. Kerman, V. Anant, B. Voronov, G. N. Gol'tsman, and K. K. Berggren. Nanowire single-photon detector with an integrated optical cavity and anti-reflection coating. *Opt. Express*, 14(2):527–534, 2006.

[3] L. Maingault, M. Tarkhov, I. Florya, A. Semenov, R. Espiau de Lamaeestre, P. Cavalier, G. Gol'tsman, J. P. Poizat, and J. C. Villegier. Spectral dependency of superconducting single photon detectors. *J. Appl. Phys.*, 107(11):116103, 2010.

[4] G. Gol'tsman, O. Minaeva, A. Korneev, M. Tarkhov, I. Rubtsova, A. Divochiy, I. Milostnaya, G. Chulkova, N. Kaurova, B. Voronov, D. Pan, J. Kitaygorsky, A. Cross, A. Pearlman, I. Komissarov, W. Slysz, M. Wegrzecki, P. Grabiec, and R. Sobolewski. Middle-infrared to visible-light ultrafast superconducting single-photon detectors. *IEEE Trans. Appl. Supercond.*, 17(2, Part 1):246–251, 2007.

[5] A. J. Kerman, E. A. Dauler, W. E. Keicher, J. K. W. Yang, K. K. Berggren, G. Gol'tsman, and B. Voronov. Kinetic-inductance-limited reset time of superconducting nanowire photon counters. *Appl. Phys. Lett.*, 88(11), 2006.

[6] E. A. Dauler, B. S. Robinson, A. J. Kerman, J. K. W. Yang, K. M. Rosfjord, V. Anant, B. Voronov, G. Gol'tsman, and K. K. Berggren. Multi-element superconducting nanowire single-photon detector. *IEEE Trans. Appl. Supercond.*, 17(2):279–284, 2007.

[7] X. Hu, T. Zhong, J. E. White, E. A. Dauler, F. Najafi, C. H. Herder, F. N. C. Wong, and K. K. Berggren. Fiber-coupled nanowire photon counter at 1550 nm with 24% system detection efficiency. *Opt. Lett.*, 34(23):3607–3609, 2009.

[8] S. Miki, M. Takeda, M. Fujiwara, M. Sasaki, and Z. Wang. Compactly packaged superconducting nanowire single-photon detector with an optical cavity for multichannel system. *Opt. Express*, 17(26):23557–23564, 2009.

[9] A. J. Kerman, E. A. Dauler, J. K. W. Yang, K. M. Rosfjord, V. Anant, K. K. Berggren, G. N. Gol'tsman, and B. M. Voronov. Constriction-limited detection

efficiency of superconducting nanowire single-photon detectors. *Appl. Phys. Lett.*, 90(10), 2007.

[10] X. Hu, C. W. Holzwarth, D. Masciarelli, E. A. Dauler, and K. K. Berggren. Efficiently coupling light to superconducting nanowire single-photon detectors. *IEEE Trans. Appl. Supercond.*, 19(3, Part 1):336–340, 2009.

[11] T. Zhong, X. Hu, F. N. C. Wong, K. K. Berggren, T. D. Roberts, and P. Battle. High-quality fiber-optic polarization entanglement distribution at 1.3 mu m telecom wavelength. *Opt. Lett.*, 35(9):1392–1394, 2010.

[12] S. Hecht, S. Shlaer, and M. H. Pirenne. Energy, quanta, and vision. *The Journal of General Physiology*, 25(6), 1942.

[13] T. Honjo, S. W. Nam, H. Takesue, Q. Zhang, H. Kamada, Y. Nishida, O. Tadanaga, M. Asobe, B. Baek, R. Hadfield, S. Miki, M. Fujiwara, M. Sasaki, Z. Wang, K. Inoue, and Y. Yamamoto. Long-distance entanglement-based quantum key distribution over optical fiber. *Opt. Express*, 16(23):19118–19126, 2008.

[14] Q. Zhang, H. Takesue, S. W. Nam, C. Langrock, X. Xie, B. Baek, M. M. Fejer, and Y. Yamamoto. Distribution of time-energy entanglement over 100 km fiber using superconducting single-photon detectors. *Opt. Express*, 16(8):5776–5781, 2008.

[15] H. Takesue, S. W. Nam, Q. Zhang, R. H. Hadfield, T. Honjo, K. Tamaki, and Y. Yamamoto. Quantum key distribution over a 40-dB channel loss using superconducting single-photon detectors. *Nature Photonics*, 1(6):343–348, 2007.

[16] D. M. Boroson, R. S. Bondurant, and J. J. Scozzafava. Overview of high rate deep space laser communications options. In G. S. Mecherle, C. Y. Young, and J. S. Stryjewski, editor, *Free-space laser communication technologies XVI*, volume 5338 of *Proceedings of the Society of Photo-Optical Instrumentation Engineers (SPIE)*, pages 37–49, 2004.

[17] J. Zhang, N. Boiadjieva, G. Chulkova, H. Deslandes, G. N. Gol'tsman, A. Korneev, P. Kouminov, A. Leibowitz, W. Lo, R. Malinsky, O. Okunev, A. Pearlman, W. Slysz, K. Smirnov, C. Tsao, A. Verevkin, B. Voronov, K. Wilsher, and R. Sobolewski. Noninvasive CMOS circuit testing with NbN superconducting single-photon detectors. *Electron. Lett.*, 39(14):1086–1088, 2003.

[18] N. Mohan, O. Minaeva, G. N. Gol'tsman, M. B. Nasr, B. E. A. Saleh, A. V. Sergienko, and M. C. Teich. Photon-counting optical coherence-domain reflectometry using superconducting single-photon detectors. *Opt. Express*, 16(22):18118–18130, 2008.

[19] A. A. Gorman and M. A. J. Rodgers. Current perspectives of singlet oxygen detection in biological environments. *Journal of Photochemistry and Photobiology*, 14(3):159–176, 1992.

[20] P. G. Pai, S. S. Chao, Y. Takagi, and G. Lucovsky. Infrared spectroscopic study of siox films produced by plasma enhanced chemical vapor-deposition. *J. Vac. Sci. Tech. A - Vacuum Surfaces and Films*, 4(3, Part 1):689–694, 1986.

[21] B. W. Caughey, A. Dong, K. S. Bhat, D. Ernst, S. F. Hayes, and W. S. Caughey. Secondary structure-analysis of the scrapie-associated protein prp 27-30 in water by infrared-spectroscopy. *Biochemistry*, 30(31):7672–7680, 1991.

[22] E. A. Dauler, M. J. Stevens, B. Baek, R. J. Molnar, S. A. Hamilton, R. P. Mirin, S. W. Nam, and K. K. Berggren. Measuring intensity correlations with a two-element superconducting nanowire single-photon detector. *Phys. Rev. A*, 78(5):053826, 2008.

[23] M. J. Stevens, B. Baek, E. A. Dauler, A. J. Kerman, R. J. Molnar, S. A. Hamilton, K. K. Berggren, R. P. Mirin, and S. W. Nam. High-order temporal coherences of chaotic and laser light. *Opt. Express*, 18(2):1430–1437, 2010.

[24] J. Kitaygorsky, J. Zhang, A. Verevkin, A. Sergeev, A. Korneev, V. Matvienko, P. Kouminov, K. Smirnov, B. Voronov, G. Gol'tsman, and R. Sobolewski. Origin of dark counts in nanostructured NbN single-photon detectors. *IEEE Trans. Appl. Supercond.*, 15(2, Part 1):545–548, 2005.

[25] X. Hu. *Coupling light to superconductive photon counters.* M. S. thesis, Massachusetts Institute of Technology, 2008.

[26] A. Verevkin, J. Zhang, R. Sobolewski, A. Lipatov, O. Okunev, G. Chulkova, A. Korneev, K. Smirnov, G. N. Gol'tsman, and A. Semenov. Detection efficiency of large-active-area NbN single-photon superconducting detectors in the ultraviolet to near-infrared range. *Appl. Phys. Lett.*, 80(25):4687–4689, 2002.

[27] A. J. Annunziata, D. F. Santavicca, J. D. Chudow, L. Frunzio, M. J. Rooks, A. Frydman, and D. E. Prober. Niobium Superconducting Nanowire Single-Photon Detectors. *IEEE Trans. Appl. Supercond.*, 19(3, Part 1):327–331, 2009.

[28] S. Miki, M. Takeda, M. Fujiwara, M. Sasaki, A. Otomo, and Z. Wang. Superconducting NbTiN nanowire single photon detectors with low kinetic inductance. *Appl. Phys. Express*, 2(7), 2009.

[29] M. G. Tanner, C. M. Natarajan, V. K. Pottapenjara, J. A. O'Connor, R. J. Warburton, R. H. Hadfield, B. Baek, S. W. Nam, S. N. Dorenbos, E. Bermudez Urena, T. Zijlstra, T. M. Klapwijk, and V. Zwiller. Enhanced telecom wavelength single-photon detection with NbTiN superconducting nanowires on oxidized silicon. *Appl. Phys. Lett.*, 96(22), 2010.

[30] D. Bitauld, F. Marsili, A. Fiore, A. Gaggero, F. Mattioli, R. Leoni, M. Benkahoul, and F. Levy. NbN nanowire superconducting single photon detectors fabricated on MgO substrates. *J. Modern Optics*, 56(2-3):395–400, 2009.

[31] S. N. Dorenbos, E. M. Reiger, U. Perinetti, V. Zwiller, T. Zijlstra, and T. M. Klapwijk. Low noise superconducting single photon detectors on silicon. *Appl. Phys. Lett.*, 93(13), 2008.

[32] F. Marsili, A. Gaggero, Lianhe H. Li, A. Surrente, R. Leoni, F. Levy, and A. Fiore. High quality superconducting NbN thin films on GaAs. *Superconductor Science & Technology*, 22(9), 2009.

[33] J. K. W. Yang, A. J. Kerman, E. A. Dauler, V. Anant, K. M. Rosfjord, and K. K. Berggren. Modeling the electrical and thermal response of superconducting nanowire single-photon detectors. *IEEE Trans. Appl. Supercond.*, 17(2, Part 1):581–585, 2007.

[34] A. J. Kerman, J. K. W. Yang, R. J. Molnar, E. A. Dauler, and K. K. Berggren. Electrothermal feedback in superconducting nanowire single-photon detectors. *Phys. Rev. B*, 79(10):100509, 2009.

[35] R. H. Hadfield. Single-photon detectors for optical quantum information applications. *Nature Photonics*, 3(12):696–705, 2009.

[36] G. S. Buller and R. J. Collins. Single-photon generation and detection. *Measurement Science & Technology*, 21(1), 2010.

[37] E. A. Dauler. *Multi-element superconducting nanowire single photon detectors.* Ph.D. thesis, Massachusetts Institute of Technology, 2009.

[38] M. Tarkhov, J. Claudon, J. Ph. Poizat, A. Korneev, A. Divochiy, O. Minaeva, V. Seleznev, N. Kaurova, B. Voronov, A. V. Semenov, and G. Gol'tsman. Ultrafast reset time of superconducting single photon detectors. *Appl. Phys. Lett.*, 92(24), 2008.

[39] T. Zhong, F. N. C. Wong, T. D. Roberts, and P. Battle. High performance photon-pair source based on a fiber-coupled periodically poled KTiOPO4 waveguide. *Opt. Express*, 17(14):12019–12030, 2009.

[40] A. Korneev, Y. Vachtomin, O. Minaeva, A. Divochiy, K. Smirnov, O. Okunev, G. Gol'tsman, C. Zinoni, N. Chauvin, L. Balet, F. Marsili, D. Bitauld, B. Alloing, L. Li, A. Fiore, L. Lunghi, A. Gerardino, M. Halder, C. Jorel, and H. Zbinden. Single-photon detection system for quantum optics applications. *IEEE J. Select. Top. Quant. Electron.* , 13(4):944–951, 2007.

[41] E. A. Dauler, A. J. Kerman, B. S. Robinson, J. K. W. Yang, B. Voronov, G. Gol'tsman, S. A. Hamilton, and K. K. Berggren. Photon-number-resolution with sub-30-ps timing using multi-element superconducting nanowire single photon detectors. *J. Modern Optics*, 56(2-3):364–373, 2009.

[42] J. K. W. Yang, E. A. Dauler, A. Ferri, A. Pearlman, A. Verevkin, G. Gol'tsman, B. Voronov, R. Sobolewski, W. E. Keicher, and K. K. Berggren. Fabrication development for nanowire GHz-counting-rate single-photon detectors. *IEEE Trans. Appl. Supercond.*, 15(2, Part 1):626–630, 2005.

[43] A. Zeilinger. Experiment and the foundations of quantum physics. *Rev. Mod. Phys.*, 71(2):S288–S297, 1999.

[44] A. Poppe, A. Fedrizzi, R. Ursin, H. Bohm, T. Lorunser, O. Maurhardt, M. Peev, M. Suda, C. Kurtsiefer, H. Weinfurter, T. Jennewein, and A. Zeilinger. Practical quantum key distribution with polarization entangled photons. *Opt. Express*, 12(16):3865–3871, 2004.

[45] D. Bouwmeester, J. W. Pan, K. Mattle, M. Eibl, H. Weinfurter, and A. Zeilinger. Experimental quantum teleportation. *Nature*, 390(6660):575–579, 1997.

[46] Z. S. Yuan, Y. A. Chen, B. Zhao, S. Chen, J. Schmiedmayer, and J. W. Pan. Experimental demonstration of a BDCZ quantum repeater node. *Nature*, 454(7208):1098–1101, 2008.

[47] T. Jennewein, C. Simon, G. Weihs, H. Weinfurter, and A. Zeilinger. Quantum cryptography with entangled photons. *Phys. Rev. Lett.*, 84(20):4729–4732, 2000.

[48] M. Aspelmeyer, H. R. Bohm, T. Gyatso, T. Jennewein, R. Kaltenbaek, M. Lindenthal, G. Molina-Terriza, A. Poppe, K. Resch, M. Taraba, R. Ursin, P. Walther, and A. Zeilinger. Long-distance free-space distribution of quantum entanglement. *Science*, 301(5633):621–623, 2003.

[49] X. Y. Li, P. L. Voss, J. Chen, J. E. Sharping, and P. Kumar. Storage and long-distance distribution of telecommunications-band polarization entanglement generated in an optical fiber. *Opt. Lett.*, 30(10):1201–1203, 2005.

[50] H. C. Lim, A. Yoshizawa, H. Tsuchida, and K. Kikuchi. Broadband source of telecom-band polarization-entangled photon-pairs for wavelength-multiplexed entanglement distribution. *Opt. Express*, 16(20):16052–16057, 2008.

[51] C. E. Kuklewicz, M. Fiorentino, G. Messin, F. N. C. Wong, and J. H. Shapiro. High-flux source of polarization-entangled photons from a periodically poled $ktiopo_4$ parametric down-converter. *Phys. Rev. A*, 69(1):013807, 2004.

[52] C. K. Hong, Z. Y. Ou, and L. Mandel. Measurement of subpicosecond time intervals between two photons by interference. *Phys. Rev. Lett.*, 59(18):2044–2046, 1987.

[53] E. Cubukcu, E. A. Kort, K. B. Crozier, and F. Capasso. Plasmonic laser antenna. *Appl. Phys. Lett.*, 89(9), 2006.

[54] L. Tang, S. E. Kocabas, S. Latif, A. K. Okyay, D.-S. Ly-Gagnon, K. C. Saraswat, and D. A. B. Miller. Nanometre-scale germanium photodetector enhanced by a near-infrared dipole antenna. *Nature Photonics*, 2(4):226–229, 2008.

[55] A. V. Akimov, A. Mukherjee, C. L. Yu, D. E. Chang, A. S. Zibrov, P. R. Hemmer, H. Park, and M. D. Lukin. Generation of single optical plasmons in metallic nanowires coupled to quantum dots. *Nature*, 450(7168):402–406, 2007.

[56] R. W. Heeres, S. N. Dorenbos, B. Koene, G. S. Solomon, L. P. Kouwenhoven, and V. Zwiller. On-Chip Single Plasmon Detection. *Nano Lett.*, 10(2):661–664, 2010.

[57] W. Srituravanich, N. Fang, C. Sun, Q. Luo, and X. Zhang. Plasmonic nanolithography. *Nano Lett.*, 4(6):1085–1088, 2004.

[58] X. Hu, E. A. Dauler, A. J. Kerman, J. K. W. Yang, J. E. White, C. H. Herder, and K. K. Berggren. Using surface plasmons to enhance the speed and efficiency of superconducting nanowire single-photon detectors. *2009 Confernce on Lasers and Electro-Optics and Quantum Electronics and Laser Science Conference*, 2009.

[59] X. Hu, F. Marsili, F. Najafi, and K. K. Berggren. Mid-infrared single-photon detection using superconducting nanowires integrated with nano-antennae. *2010 Quantum Electronics and Laser Science Conference*, 2010.

[60] X. Hu, E. A. Dauler, R. J. Molnar, and K. K. Berggren. Superconducting-nanowire single-photon detectors integrated with optical nano-antennae. *Opt. Express*, submitted.

[61] J. A. Porto, F. J. García-Vidal, and J. B. Pendry. Transmission resonances on metallic gratings with very narrow slits. *Phys. Rev. Lett.*, 83(14):2845–2848, 1999.

[62] F. J. García-Vidal and L. Martín-Moreno. Transmission and focusing of light in one-dimensional periodically nanostructured metals. *Phys. Rev. B*, 66(15):155412, 2002.

[63] J. Bravo-Abad, L. Martín-Moreno, and F. J. García-Vidal. Transmission properties of a single metallic slit: From the subwavelength regime to the geometrical-optics limit. *Phys. Rev. E*, 69(2):026601, 2004.

[64] B. A. Munk. *Frequency selective surface: theory and design.* New York : Wiley, 2000.

[65] E. D. Palik. *Handbook of Optical Constants of Solids.* New York : Academic Press, Inc, 1998.

[66] V. Anant, A. J. Kerman, E. A. Dauler, J. K. W. Yang, K. M. Rosfjord, and K. K. Berggren. Optical properties of superconducting nanowire single-photon detectors. *Opt. Express*, 16(14):10750–10761, 2008.

[67] C. J. Lada and B. A. Wilking. The nature of the embedded population in the rho-ophiuchi dark cloud - mid-infrared observations. *Astrophysical Journal*, 287(2):610–621, 1984.

[68] U. Willer, M. Saraji, A. Khorsandi, P. Geiser, and W. Schade. Near- and mid-infrared laser monitoring of industrial processes, environment and security applications. *Optics and Lasers in Engineering*, 44(7):699–710, 2006.

[69] R. Jager, M. Grabherr, C. Jung, R. Michalzik, G. Reiner, B. Weigl, and K. J. Ebeling. 57% wallplug efficiency oxide-confined 850nm wavelength GaAs VCSELs. *Electron. Lett.*, 33(4):330–331, 1997.

[70] M. Jutzi, M. Berroth, G. Wohl, M. Oehme, and E. Kasper. Ge-on-Si vertical incidence photodiodes with 39-GHz bandwidth. *IEEE Photon. Tech. Lett.*, 17(7):1510–1512, 2005.

[71] Y. D. Huang, T. Okuda, K. Shiba, and T. Torikai. High-yield external optical feedback resistant partially corrugated waveguide laser diodes. *IEEE J. Select. Top. Quant. Electron.* , 5(3):435–441, 1999.

[72] D. Ahn, C.-Y. Hong, J. Liu, W. Giziewicz, M. Beals, L. C. Kimerling, J. Michel, J. Chen, and F. X. Kärtner. High performance, waveguide integrated Ge photodetectors. *Opt. Express*, 15(7):3916–3921, 2007.

[73] B. E. Little, J. S. Foresi, G. Steinmeyer, E. R. Thoen, S. T. Chu, H. A. Haus, E. P. Ippen, L. C. Kimerling, and W. Greene. Ultra-compact Si-SiO2 microring resonator optical channel dropping filters. *IEEE Photon. Tech. Lett.*, 10(4):549–551, 1998.

[74] V. R. Almeida, R. R. Panepucci, and M. Lipson. Nanotaper for compact mode conversion. *Opt. Lett.*, 28(15):1302–1304, 2003.

[75] Q. F. Xu, V. R. Almeida, R. R. Panepucci, and M. Lipson. Experimental demonstration of guiding and confining light in nanometer-size low-refractive-index material. *Opt. Lett.*, 29(14):1626–1628, 2004.

[76] V. R. Almeida, C. A. Barrios, R. R. Panepucci, and M. Lipson. All-optical control of light on a silicon chip. *Nature*, 431(7012):1081–1084, 2004.

[77] Q. F. Xu, B. Schmidt, S. Pradhan, and M. Lipson. Micrometre-scale silicon electro-optic modulator. *Nature*, 435(7040):325–327, 2005.

[78] T. Barwicz, M. R. Watts, M. A. Popovic, P. T. Rakich, L. Socci, F. X. Kärtner, E. P. Ippen, and H. I. Smith. Polarization-transparent microphotonic devices in the strong confinement limit. *Nature Photonics*, 1(1):57–60, 2007.

[79] D. Vermeulen, S. Selvaraja, P. Verheyen, G. Lepage, W. Bogaerts, P. Absil, D. Van Thourhout, and G. Roelkens. High-efficiency fiber-to-chip grating couplers realized using an advanced CMOS-compatible Silicon-On-Insulator platform. *Opt. Express*, 18(17):18278–18283, 2010.

[80] A. W. Snyder and J. D. Love. *Optical waveguide theory.* Chapman and Hall Ltd, 1983.

[81] A. L. Zhang, K. T. Chan, M. S. Demokan, V. W. C. Chan, P. C. H. Chan, and A. H. P. Chan. Annealing effects on the loss and birefringence of silicon oxynitride rectangular optical waveguides. *Appl. Phys. Lett.*, 87(10), 2005.

[82] J. T. Hastings. *Nanometer-precision electron-beam lithography with applications in integrated optics.* Ph.D. thesis, Massachusetts Institute of Technology, 2003.

[83] Q. Fang, J. F. Song, S. H. Tao, M. B. Yu, G. Q. Lo, and D. L. Kwong. Low loss (~6.45db/cm) sub-micronpolycrystalline silicon waveguide integratedwith efficient sion waveguide coupler. *Opt. Express*, 16(9):6425–6432, 2008.

[84] C. W. Holzwarth. *Material selection and nanofabrication techniques for electronic photonic integrated circuits.* Ph.D. thesis, Massachusetts Institute of Technology, 2009.

[85] J. C. F. Matthews, A. Politi, A. Stefanov, and J. L. O'Brien. Manipulation of multiphoton entanglement in waveguide quantum circuits. *Nat. Photonics*, 3(6):346–350, 2009.

[86] J. L. O'Brien, A. Furusawa, and J. Vuckovic. Photonic quantum technologies. *Nature Photonics*, 3(12):687–695, 2009.

[87] C. M. Natarajan, A. Peruzzo, S. Miki, M. Sasaki, Z. Wang, B. Baek, S. Nam, R. H. Hadfield, and J. L. O'Brien. Operating quantum waveguide circuits with superconducting single-photon detectors. *Appl. Phys. Lett.*, 96(21), 2010.

[88] G. Nair, S. M. Geyer, L.-Y. Chang, and M. G. Bawendi. Carrier multiplication yields in PbS and PbSe nanocrystals measured by transient photoluminescence. *Phys. Rev. B*, 78(12), 2008.

[89] S. Lloyd. Enhanced sensitivity of photodetection via quantum illumination. *Science*, 321(5895):1463–1465, 2008.

[90] V. Giovannetti, S. Lloyd, and L. Maccone. Quantum metrology. *Phys. Rev. Lett.*, 96(1):010401, 2006.

[91] S. Gulde, M. Riebe, G. P. T. Lancaster, C. Becher, J. Eschner, H. Haffner, F. Schmidt-Kaler, I. L. Chuang, and R. Blatt. Implementation of the Deutsch-Jozsa algorithm on an ion-trap quantum computer. *Nature*, 421(6918):48–50, 2003.

[92] E. Knill, R. Laflamme, and G. J. Milburn. A scheme for efficient quantum computation with linear optics. *Nature*, 409(6816):46–52, 2001.

[93] S. Miki, T. Yamashita, M. Fujiwara, M. Sasaki, and Z. Wang. Multichannel SNSPD system with high detection efficiency at telecommunication wavelength. *Opt. Lett.*, 35(13):2133–2135, 2010.

[94] J. A. Kong. *Electromagnetic Wave Theory.* EMW Publishing, 2008.

[95] Y. Choi, D. Choi, and L. P. Lee. Metal-insulator-metal optical nanoantenna with equivalent-circuit analysis. *Adv. Mat.*, 22(15):1754, 2010.

[96] *2 stage 4 K cryocooler system UV210SGWUC operation manual.* Daikin Industries Ltd., 2001.

[97] J. K. W. Yang. *Superconducting nanowire single-photon detectors and sub-10-nm lithography.* Ph.D. thesis, Massachusetts Institute of Technology, 2009.

[98] K. Q. Zhang and D. J. Li. *Electromagnetic theory for microwaves and optoelectronics.* Springer, Berlin, Heidelberg, 2008.

[99] L. B. Jeunhomme. *Single-mode fiber optics: principles and applications.* Marcel Dekker, Inc., 1990.